NANOPARTICLE CARGO DELIVERY TO METASTATIC BREAST CANCER VIA TUMOR ASSOCIATED TARGETING SCHEMES

By

GIL COVARRUBIAS

Submitted in partial fulfillment of the requirements

For the degree of Doctor of Philosophy

Thesis Committee Advisor: Efstathios Karathanasis, PhD

Department of Biomedical Engineering

CASE WESTERN RESERVE UNIVERSITY

January 2021

CASE WESTERN RESERVE UNIVERSITY

SCHOOL OF GRADUATE STUDIES

We hereby approve the thesis dissertation of

Gil Covarrubias

candidate for the degree of Doctor of Philosophy*.

Committee Chair

Jeffrey R. Capadona, Ph.D.

Thesis Advisor/Committee Member

Efstathios Karathanasis, Ph.D.

Committee Member

Jennifer Yu, M.D., Ph.D.

Committee Member

Pallavi Tiwari, Ph.D.

Committee Member

Anna C. Samia, Ph.D.

Date of Defense:

August 3rd, 2020

*We also certify that written approval has been obtained for any proprietary material contained therein.

Dedication

To my Mom, my Dad and sister, Natalia, who have always encouraged me from the very first day I decided to embark on this journey. It has been really difficult not physically having you all by my side throughout this time but I know you have and will always be with me pushing forward and lifting me up. I would also like to thank the rest of my family, who have always been excited to see me and cheered on my progression. Unfortunately, my grandfather is no longer with us but I would like to say to him, "Lo hice, mas bien lo hicimos!" (I did it, rather we did it!).

To Danielle Conneely, the most amazing and selfless individual I have ever met, I will never be able to truly thank you for all the sacrifices you have made for us. Just a little over 5 years ago we graduated college and went on a journey that took us to Cleveland, OH where we didn't know a single soul let alone how long we would be there. However, none of this seemed to matter as long as we had each other. Thank you and I love you so much.

Table of Contents

Contents

List of Figures

Acknowledgements

This work would have not been accomplished without the help and guidance of others to whom I am thankful.

I would like to thank my advisor, Dr. Efstathios Karathanasis, for initially taking me as a research technician for a year and then allowing me to join his lab as a PhD student. I am truly grateful for his words of wisdom, encouragement and criticisms. He has helped me become the scientist and engineer I am today by helping me from basic experimental designs to thoughtful big picture thinking. These past five years have been trying but worth wild nonetheless. I am really thankful and I look forward to carrying the legacy.

Thank you goes out to my committee members, Dr. Jeffery Capadona, Dr. Jennifer Yu, Dr. Pallavi Tiwari, and Dr. Anna Samia for their expert advice and guidance throughout my graduate studies. I would also like to thank Dr. Prabhani Atukorale, Dr. Susann Brady-Kalnay, Dr. Chris Flask, Dr. Pubudu Peiris and Dr. Vindya Perera for being great mentors throughout my graduate degree, as this work and effort would have not been accomplished without them.

I am further thankful for the members of the Karathanasis Lab both past and present: Peter Bielecki, Morgan Lorkowski, Taylor Moon, Wyatt Becicka, Oguz Turan, Felicia He, Randall Toy and Elizabeth Doolittle. A special thanks goes out to my army of undergrads; some are now medical/graduate students themselves. This degree is as much mine as it is yours, I truly couldn't have done it without all of you: Georgia Loutranakis, Haley Sims, Abdelrahman Rhamy, Anthony Cha, Claudia Jazowski, Felicia He and Morgan Lorkowski. I would also like to thank the CCIR staff Bernadette Erokwu and Michael Kavran for their services, guidance and patience with me. It has been wonderful

working with everyone mentioned here as each of you have definitely had an impact on me both personally and academically.

I don't think I would have ever been able to make it this far if it wasn't for the Postbaccalaureate Research Education Program (PREP) were I was given the opportunity to do a one-year research program that ended culminating into the PhD. The AGEP program has further helped with my success and I am truly blessed to be a part of both of these communities of wonderful people including: Dr. Paul MacDonald, Malana Bey, Dr. Diana Ramirez, Matt Smith and Dr. Anita Howard. A special thanks goes to Dr. Agata Exner for even putting my name out there such that I would end up being recruited by PREP.

I would especially like to thank my friends from high school, college and graduate school that have made this entire experience a bit more bearable helping me get an escape from the day-to-day. Beeners in beanies (high school friends): Ismael Olivares, Ale Muniz, Brian Lovich, Carolina Yanez, Rene Yanez, Diego Carlos and Dominique Eggers. College friends: Austin Saline, Tru Hoang, Nelson Boland, Ronak Nair, Marta Mota, Pantelis Gliakamoutas and Paulina Michon. Graduate school friends: Peter Bielecki, Rajat Schivacharan, Selva Jeganathan, Kristen Gelenitis, Natalie Cole, Christopher Hernandez, Erin and Chase Rossting, Savannah Mills, Bree Christine, Alice Yang, Brain Widman, DaShawn Hickman, Kelsey Bower, Nadia Rose, Nate Braman, Nick VanDillen, Rahul Hedge, Leah Plasek, Brent Eastman, Eric Dennis and Abhi Kakkar. I truly thank all of you for keeping me sane and for all of the great times we have had thus far.

Danielle Conneely, the most amazing and selfless individual I have ever met, I will never be able to truly thank you for all the sacrifices you have made for us. Just a little over

5 years ago we graduated college and went on a journey that took us to Cleveland, OH where we didn't know a single soul let alone how long we would be there. However, none of this seemed to matter as long as we had each other. Thank you and I love you so much.

Finally, I would like to thank my Mom, my Dad and sister, Natalia, who have always encouraged me from the very first day I decided to embark on this journey. It has been really difficult not physically having you all by my side throughout this time but I know you have and will always be with me pushing forward and lifting me up. I would also like to thank the rest of my family, who have always been excited to see me and cheered on my progression. Unfortunately, my grandfather is no longer with us but I would like to say to him, "Lo hice, mas bien lo hicimos!" (I did it, rather we did it!).

List of Abbreviations

(c)RGD-NP	$\alpha_v\beta_3$ integrin-targeted nanoparticle
4T1	Balb/C derived TNBC murine tumor model
ANOVA	Analysis of variance
APC	Antigen presenting cells
BC	Breast cancer
BLI	Bioluminescence imaging
c-KIT	Tyrosine-protein kinase KIT
CAR-T cell	Chimeric antigen T cell receptor
CCK-8	Formazan-based cell counting assay
CCR2	Chemokine receptor type 2
cdGMP	cyclic-di-guanylate monophosphate
CDN	Cyclic di-nucleotide
CNS-1	Cellosaurus cell line rat glioma model
CPI	checkpoint inhibitors
CREKA-NP	Fibronectin-targeted nanoparticle
CT	Computed tomography
CTC	Circulation tumor cells
CTLA-4	Cytotoxic T-lymphocyte-associated protein 4
D2.A1/OR	D2-Hyperplastic alveolar nodules (HAN) series mTNBC cell line
DAPI	4’,6-diamidino-2-phenylindole
DiR	1,1'-Dioctadecyl-3,3,3',3'-Tetramethylindotricarbocyanine Iodide
DMSO	Dimethyl sulfoxide

DOPC	1,2-dioleoyl-sn-glycero-3-phosphocholine
DOX	Doxorubicin
DPPC	1,2-dipalmitoyl-sn-glycero-3-phosphocholine
E-cad	Epithelial cadherin
EGFR	Epidermal growth factor receptor
EGFR-NP	EGFR-targeted nanoparticle
EMT	Epithelial-mesenchymal transition
EPR	Enhanced permeability and retention effect
FBS	Fetal bovine serum
FMT	Fluorescence molecular tomography
GBM	Glioblastoma multiforme
GFP	Green fluorescent protein
IACUC	Institutional Animal Care and Use Committee
ICAM-1	Intercellular adhesion molecule-1
IDO	Indoleamine 2,3-dioxygenase
IFN-α/β	Type 1 Interferons α and β
IL-10	Interluekin-10
IO	Iron oxide
IP	Intraperitoneal
IVIS	Spectrum in vivo imaging system
MALDI-MS	Matrix-assisted laser desorption/ionization mass spectroscopy
MDSC	myeloid derived suppressor cells

mPEG2000-DSPE	1,2-distearoyl-sn-glycero-3-phosphoethanolamine-N-[methoxy-(polyethylene glycol)-2000
MRI	Magnetic resonance imaging
MSN	Mesoporous silica nanoparticle
mTNBC	Metastatic triple negative breast cancer
MWCO	Molecular weight cutoff
NHS	N-hydroxysuccinimide
NIR	Near-infrared spectroscopy
NK	Natural killer cells
NMR	Nuclear magnetic resonance
NP	Nanoparticle
NT-NP	Nontargeted nanoparticle
OSEM	Ordered subset expectation maximization
OX40	Cluster of differentiation 314
PBS	Phosphate-buffered solution
PD-1	Programmed death 1
PET	Positron emission tomography
PSN-NP	P-selectin-targeted nanoparticle
PTP-μ	Receptor tyrosine phosphatase mu
ROI	Region of Interest
SD	Standard deviation
SEM	Standard error of means
SPIONs	Superparamagnetic iron oxide nanoparticles

STING	Stimulator of interferon genes
Sulfo-SMCC	Sulfosuccinimidyl 4-(N-maleimidomethyl)cyclohexane-1-carboxylate
TGF-β	Transfomring growth factor-β
TLC	Thin layer chromatography
TME	Tumor microenvironment
TNBC	Triple negative breast cancer
TSTU	Tetrafluoroborate
U-87 MG	U87 derived human primary glioblastoma cell line
USPIONS	Ultrasmall SPIONs
µCi	Microcurie

Nanoparticle Cargo Delivery to Metastatic Breast Cancer via Tumor Associated Targeting Schemes

Abstract

By

GIL COVARRUBIAS

The high morbidity associated with triple negative breast cancers (TNBCs) is directly related to its high risk of recurrence. TNBC recurrence is often invasive - leading to its metastasis (mTNBC) in visceral organs including the lungs, liver, and brain. With these phenotypic characteristics nearly all newly diagnosed patients with mTNBC will have a poor prognosis. The difficulty with metastatic disease is two-fold: 1) micrometastasis (> 1cm) cannot be reliably detected by conventional diagnostic techniques and 2) therapeutic windows are reduced as the metastatic lesions are not easily accessible to systemically administered agents. Thus, the difficulty in diagnosis and treatment lies to a great degree in adequately targeting imaging and therapeutic agents to metastasis. However, it is well documented that metastatic niches upregulate receptors that are not commonly found in healthy tissues such as nonendogenous matrix proteins (i.e. PTP-mu, fibronectin/fibrinogen), adhesion molecules (i.e. selectins, cadherins and integrins) and cell specific markers (i.e. EGFR and integrins). Nanotechnology offers a unique solution such by incorporating targeting ligands that can direct nanoparticles to these tumor-associated upregulated biomarkers. By decorating the surface of nanoparticles with targeting moieties, we can adequately administer nanoparticles loaded with either contrast agents, chemotherapeutics or immunotherapeutics. In this dissertation, we show that targeted

nanoparticles can significantly improve diagnosis and treatment of metastatic breast cancer.

Overview

Metastatic disease is often visualized as undeveloped disseminated micrometastasis throughout solid tumor progression or as a factor of disease recurrence years after reported stable remission. Metastasis often evades standard clinical detection due to seemingly invisible colonies that further curtail therapeutic approaches including first-line chemotherapy. Here we aim to develop mechanisms that would aid in detailing a targeted approach for both detection of and drug delivery to metastatic tumor microenvironments. Metastatic disease is frequently characterized as both a heterogeneous and dynamic disease state often displaying variable spatial and temporal cues in the form of biomarker upregulation. The goal of this dissertation is to use nanoparticle constructs to target systemically available tumor-associated biomarkers to further enhance the detection rate of and drug delivery to (i.e. chemotherapeutic agents and immunostimulatory molecules) metastatic niches. This dissertation is organized in the following five chapters:

Chapter 1: Introduction and Thesis Organization

This chapter provides a background in metastatic breast cancer and challenges associated with detection and treatment. Here we also focus on the mechanisms required for improved detection and therapeutic outcome using nanoparticles as a platform technology. Lastly, we identify the immunosuppressive characteristics of the disease and the means to reinvigorate a senescent immune system to promote an anti-tumor response.

Chapter 2: Imaging of Cancer Metastasis via Multi-ligand Nanoparticles

Metastasis displays a highly heterogeneous cellular population with cancer cells continuously evolving. With this behavior, biomarker expression is often variable due to disease progression at variant locations. Here we explore the use of a multi-ligand

nanoparticle through its surface decoration with four different types of ligands. This multi-ligand targeting scheme enabled nearly a 3-fold increase in lung metastases nanoparticle deposition when compared to its single-ligand variants. PET imaging showed that a multi-ligand nanoparticle labeled with [^{18}F]fluoride was able to precisely target metastatic disease at its very early stage of development in three different animal models of metastatic breast cancer.

Chapter 3: Chemotherapeutic Delivery via Systemically Administered Tumor Targeted Nanoparticles

This chapter uses the principles acquired in the previous chapter to develop a therapeutic protocol. Here we used a dual-ligand nanoparticle loaded with the chemotherapeutic drug doxorubicin to target EGFR and αvβ3 integrin overexpressed on metastatic cancer cells. We observed that the treatment with the dual-ligand nanoparticle yielded significant improvement and event-free survival in a mouse model of breast cancer metastasis.

Chapter 4: Immune Agonist Delivery to Metastatic Triple Negative Breast Cancer via Site Specific Nanoparticle Targeting

This chapter focuses on the delivery of immunostimulatory molecules to triple negative breast cancer (TNBC). While chemotherapeutic delivery is typically employed as a first-line treatment, chemoresistance often leads to tumor recurrence. Here we use a nanoparticle carrier and tumor targeting approaches to deliver immune potentiating agonists to aid in overcoming the profound immunosuppressive nature associated with tumor regions. Using such a therapy elicits immune-recognition and T cell-mediated killing

of tumor cells, proving a powerful approach for treating metastatic disease and preventing recurrence.

Chapter 5: Summary and Future Directions

This chapter offers a summary of the work provided here and an interpretation of the results acquired. Furthermore, the impact of the work is described in relation to metastatic cancer detection and treatment. Future directions and alternative work including developing similar targeting strategies for glioblastoma multiforme (GBM) are also detailed here.

Chapter 1: Introduction and Thesis Organization

Vascular targeting of nanoparticles for molecular imaging of diseased endothelium.
Atukorale PU, Covarrubias G, Bauer L, Karathanasis E.

Precise targeting of cancer metastasis using multi-ligand nanoparticles incorporating four different ligands
Peiris, Pubudu M., Felicia He, Gil Covarrubias, Shruti Raghunathan, Oguz Turan, Morgan Lorkowski, Bhargavee Gnanasambandam, C. Wu, W. P. Schiemann, and Efstathios Karathanasis.

1.1 Metastatic Breast Cancer

The majority of breast cancer (BC) associated-deaths are due to the high risk of recurrence years after individuals are reported to be in stable remission[1]. Recurrence is often invasive leading to its metastasis in visceral organs including the lungs, liver, brain and bone[2,3]. While first-line therapies often display promising results in BC patients, most succumb to recurrent disease due to small colonies of disseminated tumor cells enabling the establishment and outgrowth of metastatic niches[2,3]. Due to the first-treatment regimen, the recurrent disease phenotype is characteristically pro-survival and chemoresistant, making secondary treatments ineffective against metastatic breast cancers. Besides their resistant phenotype, disseminated breast cancer cells often escape clinical detection by remaining dormant before remerging as incurable secondary tumors[4,5]. Dormant disseminated tumor cells cease dividing and are potential 'time bomb' that survive in quiescent/senescent states prior to initiating their 'explosive' metastatic outgrowth[6–8]. Since dormant disseminated tumor cells are slow-dividing cells, antimitotic agents, the current standard-of-care has proven to be ineffective.

The implementation of non-traditional therapeutics is thus required due to the poor prognosis of metastatic breast cancers. As a front runner, cancer immunotherapy holds an inherent ability to treat aggressive and metastatic forms of breast cancer effectively. Immunotherapy, including chimeric antigen receptor T cell therapy and checkpoint inhibitors, activate and mobilize an adaptive response often carried out by effector T-cells promoting tumor regression and clearance.[9,10] However, due to the potency and relentless activation of effector T-cells, instances of T-cell exhaustion and off-target toxicity have reduced the overall effectiveness of such therapies.[9] Furthermore, the complexity of the

tumor microenvironment constantly evolves and variant phenotypic characteristics enables a stealth-like behavior via an immunosuppressive profile. The immunosuppressive "cold" tumor microenvironment expels pro-tumor cues leading to immunological ignorance such that effector cells including natural killer (NK) cells and most importantly cytotoxic T-cells ($CD8^+$ T-cells) are either no longer trafficked to or are shuttled out of tumor sites, thereby shielding developing tumors from systemic immunosurveillance[11,12]. Thus, there is a need to re-educate the suppressed immune system within the tumor microenvironment to adequately support an effective immune response.

1.2 Targeting the Heterogenous and Dynamic Tumor Microenvironment via Perivascular Targeting of Nanoparticles

Tumor microenvironments are both heterogenous and dynamic, often developing variable spatial and temporal phenotypic cues throughout disease progression. Nanotechnology has actively moved into the development of targeted particles for the enhancement of drug delivery and contrast-enhanced clinical imaging.[13–20] However, many of these technologies often only exploit the upregulation of a single targeting moiety provoking the unintended stratification of malignancies as homogenous and static. Rather, multivalent targeted nanoparticles schemes show promise in effectively delivering chemotherapeutic agents and contrast agents.

1.2.1 – Passive vs Active Tumor Targeting

The deposition of nanoparticles into tumor bearing regions can be achieved via two different mechanisms: either passive or active targeting (**Fig 1.1**). Enhanced Permeability and Retention Effect (EPR)-driven passive targeting is based on the premise that a

developed and sizeable tumor mass has grown too rapidly leading to angiogenesis and leaky and ill-formed blood vessels (i.e. gap-junctions do not properly seal blood vessels leaving 200-500 nm gaps).[13,21] The compromised vasculature enables long circulating nanoparticles to naturally drain within tumor margins. However, this phenomenon is not necessarily observed in early metastatic niches as these lesions are not well established, yielding poor passive delivery.[4,22–24]

On the other hand, active targeting schemes are specifically designed to target upregulated biomarkers that are overexpressed on or adjacent to cancer cells, the tumor extracellular matrix and tumor-associated vasculature for enhanced therapeutic deposition (**Fig 1.2**)[16,21,24–27]. Based on the targeting mechanism, active targeting can be further separated into two different categories – deep-tissue targeting or perivascular targeting. Targeting upregulated biomarkers on cancer cells (deep-tissue targeting) requires nanoparticles to successfully extravasate across the endothelium, navigate through the extracellular space and successfully interact with cell-surface receptors on the targeted cancer cells.[28] Furthermore, the interstitial pressure observed in tumor masses invokes another difficult-to-overcome hurdle. Thus, the underlying properties required for deep-tissue targeting makes this delivery system often inconsistent and unfavorable. Perivascular targeting, however, is intrinsically exploitable.[28] Micrometastatic colonies are typically docked or adjacent to the vascular network. The accompanying endothelium subsequently becomes a viable target for systemically administered nanoparticles for two main reasons: 1) the endothelium often shows danger signals in the form of upregulated biomarkers and 2) systemically administered nanoparticles have direct access to the vasculature and perivascular space enabling them to scavenge their target more proficiently

when compared to deep-tissue targeting (**Fig 1.2**). Thus, perivascular targeting allows us to specifically localize and target metastasis.[16,21,24–26,28]

1.2.2 – Targeting Ligands for Active Targeting

As previously mentioned, it is important to not stratify a tumor microenvironment as homogenous and static. A nanoparticle's versatility and multivalent characteristics allows for the surface decoration of multiple targeting ligands that specifically target upregulated receptors overexpressed in tumor microenvironments. While there is a plethora of cancer biomarkers, here we will focus on some of the more traditional or mainstream targeting schemes.

- Extracellular matrix protein targeting[21,29–31]: Nonendogenous matrix proteins are often upregulated or recruited for the growth, development and extravasation of tumors. Due to blood clotting in cancerous lesions, fibrin-based proteins typically arise from systemic intervention as a result of the injured endothelium. Here fibrin protein networks are developed after leaking into the tumor interstitium aiding in the development of the extracellular matrix. By surface modifying a nanoparticle with a CREKA, peptide we can target fibrinogen/fibronectin complexes.
- Adhesion molecule targeting[14,15,24,32,33]: Adhesion molecules typically expressed in wound healing are often highjacked by circulating tumor cells for their docking and attachment to distal regions (i.e. E- and P-selectins, and $\alpha v\beta 3$ integrins). Furthermore, these adhesion molecules are expressed on a variety of cells including endothelial, cancer, and immune cells. The accessibility of the

target in the diseased tissue enables a significant accumulation of moiety targeted nanoparticles.

- Cell-specific receptor targeting[17,34]: There are several cell markers highly expressed on cancer cells such as epidermal growth factor receptor (EGFR), c-KIT, and epithelial cadherins (E-cad). Targeting these biomarkers allows for the direct localization of nanoparticle carrier to tumor cells.

To capture the heterogenic and dynamic characteristic of metastatic disease, a multi-ligand nanoparticle construct is desired to deliver maximal therapeutic cargo or contrast-enhanced agents for the treatment and detection, respectively, of metastatic disease.

1.3 Nanoparticles as Imaging Agents and Drug Delivery Carriers

The design of nanoparticle constructs as imaging agents and drug delivery carriers is highly engineerable and tunable. Nanoparticle technology is highly versatile primarily due to the potential material composition. Nanoparticles can range from inorganic (i.e. gold, iron, silica) to lipid, polymeric and nucleic acid-based compounds. The chemistry behind such constructs enables for variances in size, shape, and surface composition for a variety of applications[28,35–37]. In terms of nanoparticles for imaging agents, iron-based nanoparticles (i.e. SPIONs, USPIONs, and iron oxides) are intrinsically designed as MRI T2-weighted contrasted enhancing agents[14,28,38]. Gold nanoparticles are often developed for x-ray-based techniques such as CT due to their contrast enhancement and their ability to be surface modified to envelop tissue targeting moieties[16,28,39]. In this research we used mesoporous silica nanoparticles to encapsulate [^{18}F]fluoride, a positron emission

tomography (PET) agent, to enable imaging of lung micrometastasis with sizes in the range of 1 mm.

In terms of drug delivery carriers, lipid, silica, polymeric and nucleic acid-based nanoparticles offer: 1) stable loading of hydrophobic or hydrophilic therapeutic agents, 2) significantly high drug loading and 3) easily manipulated surface chemistry to incorporate tumor-specific targeting ligands[13,24,37,40]. Through the screening of several different types of particles, for the vast majority of this work, we use a liposome due to its great adaptability. The utilization of liposomes meet three important criteria: 1) its simplicity and reproducibility allow us to rapidly screen several targeting moieties without having to significantly change the synthetic procedures, 2) its hydrophobic membrane and hydrophilic core allow for a diverse set of therapeutic molecules to either be loaded or encapsulated within its structure and 3) its surface coating is easily manipulated based off of the lipids used allowing for either single or multivalent surface decoration of targeting ligands[19,20,24,40].

For the delivery of imaging and therapeutic agents to a tumor microenvironment, it is vital to capture each and every metastatic node[14,18,32,41–43]. Thus, the utilization of multivalent nanoparticle constructs is significantly important to accomplish these two tasks. Exploiting and targeting upregulated tumor-associated biomarkers, and not considering the environment monolithic, will allow for the maximal delivery of both chemotherapeutic and contrast agents. In the case of immunotherapy delivery, as described in the next section, targeting each metastatic lesion might not be as important. Upon reactivating an immune senescent tumor microenvironment, a systemic response is initiated which can localize and target tumor regions that were not necessarily exposed to

the nanoparticle treatment itself. In the next section, we will describe the challenges behind the immunosuppressive nature of tumors, delivery challenges and the respective solutions for such a problem.[9,10,13,44]

1.4 Re-educating the Immunosuppressed Tumor Microenvironment via the Delivery of Immune-potentiating Agents

While effective as an initial treatment, the systemic delivery of chemotherapeutic agents cannot prevent the risk of recurrence. If recurrence does occur, tumor cancer cells can adapt to such systemic therapies and develop resistance even though these cytotoxic drugs initially show high potency[1,45,46]. Recently, exciting advances are pointing out that immunotherapy can address the limitations of today's anticancer therapies. Immunotherapies such as checkpoint inhibitors (i.e. CTLA-4, OX40 and PD-1), chimeric antigen T cell receptors (CAR-T cells) and recombinant cytokines have shown clinically significant therapeutic outcomes where chemotherapy has failed[9,10,47]. These treatment strategies rely on the mobilization of adaptive immunity to promote tumor clearance.

On the other hand, *in situ* cancer vaccines focus on the activation of the innate immune system which further shows promise[13,47,48]. Harnessing an innate immune pro-inflammatory response within a tumor microenvironment (TME) is key to an effective therapeutic outcome. Innate cells, specifically antigen presenting cells (APCs, i.e. dendritic cells and macrophages), must continuously scavenge tumor-associated antigens by either engulfing tumor cells or retrieving shed debris. The innate arm of immunity will then subsequently travel to the nearest lymph node -the hub for innate and adaptive immunity communication - where APCs will directly prime and activate effector T-cells for a robust

anti-tumor clearance response. However, as a tumor progresses, its defense mechanisms rise through pro-tumor cytokine release (i.e. IL-10 and to some degree TGF-β) and upregulated inhibitory ligands (i.e. CTLA-4, OX40 and PD-1) [13,47,48]. These pro-tumor cues lead to immunological ignorance in the form of innate cell dysfunction, the tumor hijacking of immune cells, and the shuttling out of effector cells including natural killer (NK) cells and most importantly cytotoxic T-cells ($CD8^+$ T-cells) - all of which are factors that promote tumor growth and extravasation to distal regions[13,47,48]. This overwhelmingly immunosuppressive TME often results in a poor prognosis. Furthermore, it is not surprising that immunotherapies such as CAR-T cells and immune checkpoint inhibitors have clinically shown to have a suboptimal efficacy of about 20% as systemic T-cells either fail to be trafficked or lack the capability of infiltrating an immunosuppressive TME[9].

To relinquish the tumor stronghold on innate immunity within malignant lesions, we employ the use of a Stimulator of Interferon Genes (STING) agonist, cyclic-di-guanylate monophosphate (cdGMP)[48–52]. The activation of the STING pathway is self-amplifying and self-propagating as its downstream cascade leads to the production of type 1 interferons, such as IFN-α/β which further aid to enhance the innate response by reviving a suppressed TME. From an indirect measure, not particularly looking at IFN-α/β secretion, system functionality can be observed through an increase in tumor clearing cells including NK and $CD8^+$ T-cells[48–52]. Immunostimulatory molecules are often delivered locally as their therapeutic index reaches its highest potency in these conditions. However, such a therapy requires the exact topological location of the tumor and the feasibility of reaching it, which is challenging in a metastatic setting. If delivered systemically, the immunotherapy could elicit significant repercussions as off targeting may occur, which

could potentiate a profound systemic immune response. To adequately deliver cdGMP to the tumor microenvironment, we passively encapsulated it into a lipid-based nanoparticle and administered it intravenously using our nanoparticle targeting schemes[14–20,37,53,53]. While we are eliciting an innate response using this treatment scheme, the adaptive immune system must also be taken into consideration. The combinatorial delivery of checkpoint inhibitors is a necessity to achieve a high cure rate. The use of anti-PD-L1/-1 and anti-CTLA-4 in combination with an *in situ* nanoparticle vaccine will allow the newly reactive cancer immunity cycle to reduce any further blockades by either functional effector T-cells or cancer cells[9].

1.5 Thesis Organization: Specific Objectives Overview and Hypotheses

Micrometastatic disease (<1cm) often evades detection and therapeutic treatments due to its seemingly invisible size. However, it is well established that the vascular network associated with such a disease often displays and upregulates danger signals in the form of biomarkers. As these biomarkers are readily targetable via the bloodstream, we employ the use of nanoparticles whose surface is decorated with tumor-targeting ligands. Tumor-associated receptors include nonendogenous matrix proteins, adhesion molecules and cell-specific receptors that are readily targetable. In this dissertation, we focus on developing multivalent nanoparticles that specifically target metastatic niches for significant delivery of contrast-enhanced, chemotherapeutic and immunotherapeutic agents.

1.5.1 – Objective 1: To Develop Nanoparticle Targeting Schemes for Imaging Metastatic Breast Cancer

Rationale: It is well documented that metastatic tumor microenvironments can be differentiated from healthy tissues as indicated by the stark differences in biomarker upregulation. We have previously developed nanoparticles that have targeted metastatic niches using single-ligand nanoparticles. However, due to the dynamic and heterogeneous characteristics of metastatic disease some metastatic nodes were missed upon using tumor-targeting technique. **In Chapter 2, we hypothesize that developing a multi-ligand nanoparticle will allow for its complete deposition across temporally and spatially variant metastatic niches capturing the dynamic and heterogenic tumor microenvironment.** Within this chapter, we initially observe *ex vivo* nanoparticle localization with an assortment of targeting techniques using a fluorescently labeled liposomal nanoparticle. Applying a multi-ligand targeting approach from technique learned in the *ex vivo* studies, we use a mesoporous silica nanoparticle loaded with PET probe to engage in *in vivo* imaging of a variety of tumor microenvironments including aggressive and dormant metastasis.

1.5.2 – Objective 2: To Apply Nanoparticle Targeting Schemes for Chemotherapeutic Delivery to Metastatic Breast Cancer

Rationale: Utilizing the targeting strategies observed in chapter 2, we will be able to employ these techniques to deliver therapeutic cargo to metastatic niches. **In chapter 3, we hypothesize, by using a similar multi-ligand targeting approach, that we will be able to deliver a maximal chemotherapeutic payload to an aggressive metastatic triple negative breast cancer in an effort to yield an improved prognosis and survival.** A

similar approach is required as chemotherapeutic agents must be delivered to every single metastatic cell in order to reach full recovery.

1.5.3 – Objective 3: To Apply Nanoparticle Targeting Schemes for Immunostimulatory Delivery to Metastatic Breast Cancer

Rationale: The delivery of immunostimulatory molecules requires a slightly different approach as it is no longer necessary to target each and every single cell. Here, our approach is to identify a targeting ligand that will yield a significant accumulation of immuno-nanoparticles. **In chapter 4, we hypothesize that the identification of a targeting scheme for the delivery of an immuno-nanoparticle will yield a profound recruitment and expansion of both innate and adaptive immune cells within tumor margins and in circulation.** In this case, the reactivation of the immune system will target distal metastatic niches such that the multivalent targeting approach might not be required.

1.6 Figures

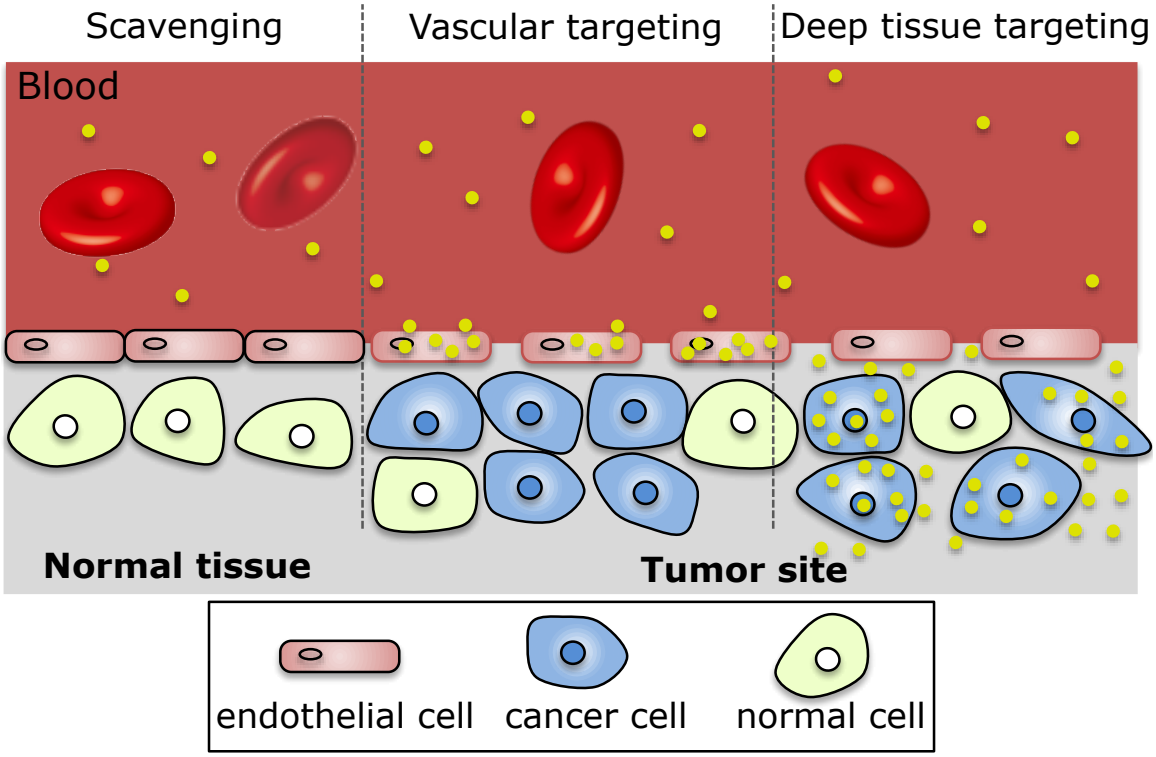

Figure 1.1 Vascular Targeting vs Deep Tissue Targeting

Schematic depicting vascular targeting and deep tissue targeting under systemic nanoparticle administration.

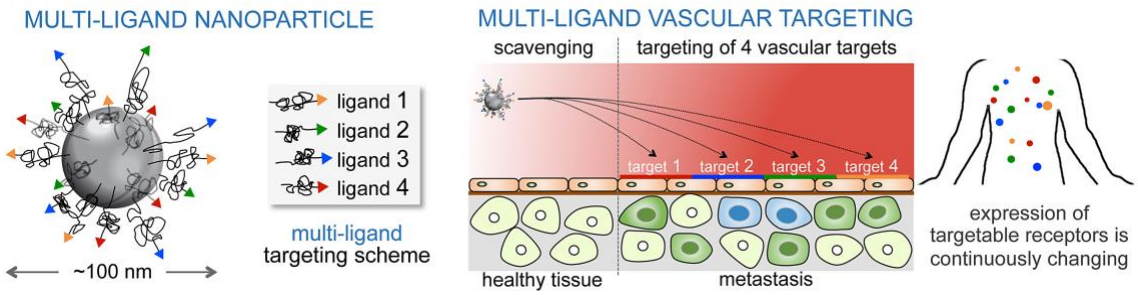

Figure 1.2 Illustration of Systemically Administered Nanoparticles Targeting the Perivascular Niche

Chapter 2: Imaging of Cancer Metastasis via Multi-ligand Nanoparticles

Precise targeting of cancer metastasis using multi-ligand nanoparticles incorporating four different ligands

Peiris, Pubudu M., Felicia He, Gil Covarrubias, Shruti Raghunathan, Oguz Turan, Morgan Lorkowski, Bhargavee Gnanasambandam, C. Wu, W. P. Schiemann, and Efstathios Karathanasis.

2.1 Abstract

Metastasis displays a highly heterogeneous cellular population with cancer cells continuously evolving. As a result, a single-ligand nanoparticle cannot account for the continuously changing expression of targetable biomarkers over time and space. To effectively direct nanoparticles to metastasis, we developed a multi-ligand nanoparticle by using four different types of ligands on the same nanoparticle that target biomarkers on the endothelium associated with metastatic disease. These vascular targets included $\alpha_v\beta_3$ integrin, P-selectin, EGFR and fibronectin. Using terminal and in vivo imaging studies, the targeting performance of the multi-ligand nanoparticles was compared to the single-ligand nanoparticle variants. All four single-ligand nanoparticle variants achieved significant targeting of lung metastasis in the 4T1 mouse model of breast cancer metastasis with about 2.5% of the injected dose being deposited into metastasis. A dual- ligand nanoparticle resulted in a nearly 2-fold higher deposition into lung metastases than its single-ligand counterparts. The multi-ligand nanoparticle significantly outperformed its targeting nanoparticle counterparts achieving a deposition of ~7% of its injected nanoparticles into lung metastases. Using the high sensitivity of radionuclide imaging, PET imaging showed that a multi-ligand nanoparticle labeled with [^{18}F]fluoride was able to precisely target metastatic disease at its very early stage of development in three different animal models of metastatic breast cancer.

2.2 Introduction

Various targeting ligands schemes have been employed to direct nanoparticles to tumors. However, traditional strategies using a single-ligand system often consider cancer as a mono- lithic disease and fail to account for tumor heterogeneity. This is particularly evident in the case of metastatic disease. Metastatic cancer cells continuously evolve and change the expression of targetable cell-surface biomarkers over time and space[1–5], which results in different metastatic lesions being targeted by different ligands. To capture the dynamic nature of metastasis, we designed multi-ligand nanoparticles that employed four different ligands on the same nanoparticle to effectively target variations in receptor presentation on the endothelium of metastatic lesions (**Fig 2.1**). Our targeting concept is based on three key components that synergistically facilitate effective nanoparticle targeting of the heterogeneity of metastatic disease and its dissemination: (1) Vascular targeting of nanoparticles (rather than traditional deep-tissue targeting); (2) a selection of vascular targets that are over- expressed in metastatic microenvironments; and (3) a four-ligand targeting system that considers the dynamic microenvironment of metastasis by accounting for potential spatiotemporal alterations in the expression patterns of four targetable biomarkers, including $\alpha_v\beta_3$ integrin, P-selectin, EGFR, and fibronectin.

Targeting of upregulated receptors on cancer cells in the tumor interstitium (deep-tissue targeting) requires the nanoparticle has to successfully extravasate across the endothelium, navigate through the extracellular space and finally have meaningful interactions with the cell-surface receptors on the target cells. Unfortunately, the microenvironment of early metastasis does not favor deep-tissue targeting of nanoparticles.[22,23,25,58]The early spread of metastatic cancer cells to distant organs results

in small clusters of cancer cells that lack leaky endothelium.[59] On the other hand, the endothelium is the closest point-of-contact for circulating nanoparticles. By having direct access to the vascular bed, circulating nanoparticles can continuously scavenge for vascular cancer biomarkers. Most importantly, the size and the multivalent avidity, due to formation of multiple receptor-ligand bonds, makes nanoparticles ideal for targeting vascular-associated pathologies. In previous studies, we showed that vascular targeting is more effective than deep-tissue targeting in mouse models of breast cancer metastasis.[14–16,53]

Further, the endothelium associated with metastasis offers a diverse set of targetable biomarkers, which differ from that of healthy vascular beds. Metastatic cancer cells develop their own distinct microenvironment and upregulate specific biomarkers in the lumen of colonized blood vessels in distant organs.[15,22,23,25,58] In this work, we selected mouse models of triple-negative breast cancer (TNBC), which are highly metastatic and exhibit a high recurrence rate and mortality.[60]To target metastatic TNBC, we selected four different peptides that target 1) receptors on metastatic TNBC cells (*i.e.*, EGFR, $\alpha_v\beta_3$ integrin); 2) the adhesion molecules of the leukocyte adhesion cascade that circulating tumor cells (CTCs) use to attach to the endothelium of distant metastasis (*i.e.*, E- and P-selectin, $\alpha_v\beta_3$ integrin); and 3) overexpressed glycoproteins of the extracellular matrix in the near-perivascular regions of metastasis (*i.e.*, fibronectin). These vascular biomarkers often exhibit spatiotemporal variability representing different microenvironments.[15]

To thoroughly evaluate targeting variants of nanoparticles, we used various mouse models of breast cancer metastasis that represent a broad spectrum of the disease. In particular, we focused on the imaging and diagnostic application of targeted nanoparticles.

While current clinical modalities can detect large metastases (>1 cm) with accuracy,[43,61,62] today's imaging rarely detects disseminated disease (*i.e.*, micrometastasis), which prohibits early and effective interventions.[63] By the time metastatic disease becomes clinically evident, long-term patient outcome is not favorable. In previous work, we have also demonstrated effective drug delivery to hard-to-reach tumors using vascular targeting and single-ligand schemes.[38,53,64] To illustrate the broad application of multi-ligand targeting schemes, we selected two types of nanoparticles, which are all-purpose, versatile nanoparticles for numerous types of therapeutic and imaging agents. Specifically, we used 100-nm liposomes and silica nanoparticles.[65–68] Importantly, these nanoparticles can conveniently accommodate multi-ligand strategies. Presentation of different types of ligands can be easily controlled on the surface of the nanoparticles in terms of ligand density and ratio among different ligands types. Using fluorescence and radionuclide imaging, we show that multi-ligand nanoparticles are capable of precise and effective targeting and recognition of metastatic disease at its early stages of development.

2.3 Methods and Materials

2.3.1 Nanoparticle Fabrication

We prepared 100-nm liposomes using established methods.[15,26,37,42,65,66] The DPPC and DSPE-PEG(2000)-ligand were used as the lipid matrix for the liposomes. The lipids were dissolved in ethanol and hydrated with PBS at 60 °C followed by sequential extrusion in a Lipex Biomembranes Extruder (Northern Lipids, Vancouver, Canada), to size the liposomes to 100 nm. After extrusion, the nanoparticles were dialyzed against PBS for 1 day using a 100 kDa MWCO dialysis tubing (Spectrum Laboratories, CA). A lipid composition of DPPC, cholesterol and DSPE-PEG(2000)-ligand in the molar ratio of 60-X:40:X was used. Depending on the nanoparticle variant, X was 2, 4.2 or 5.6 mol% for the single-, dual- or quadruple-ligand nanoparticle, respectively. The dual- and quadruple-ligand particles used an equal ratio of the two or four ligand conjugates. For the fluorescence imaging studies, each liposome variant was labeled with an Alexa 647 fluorophore. The fluorophore was conjugated directly onto the lipid DSPE. DSPE-Alexa-647 was used as part of the lipid matrix at 2.5 mol%.

2.3.2 Functionalization of Nanoparticles with Targeting Ligands

Functionalization was performed using previously established methods.[15,17,69] The $\alpha_v\beta_3$ integrin-targeting peptide c(RGDfC), [14,15,32] P-selectin-targeting peptide CDAEWVDVS, [15,24,33] fibronectin-targeting peptide CREKA,[29] and the EGFR-targeting peptide CYHWYGYTPQNVI,[17,34] were used. Each peptide was conjugated on the distal end of DSPE-PEG-NH_2 using standard conjugation chemistry. The completion of the reaction was confirmed using thin layer chromatography (TLC). TLC was carried out on silica gel coated fiber sheets using a mixture of $CHCl_3$/MeOH as the mobile phase.

2.3.3 Animal Models

All animal studies were conducted under a protocol approved by the Institutional Animal Care and Use Committee (IACUC) at Case Western Reserve University. The well-being of the animals took priority over precise measurements in decisions regarding euthanasia or other interventions. All animals received standard care, including *ad libitum* access to food and water, a 12/12 light/dark cycle, appropriate temperature and humidity. Teklab Global #2018 was fed to mice that were imaged with fluorescent imaging. This is because the standard rodent diet has chlorophyll, which adds artifacts to fluorescent images.

We developed three different models of breast cancer metastasis based on the 4T1, D2.A1, and D2.OR cancer cells. All cell lines were engineered to stable express firefly luciferase and green fluorescent protein (GFP). In the case of the 4T1 model, we inoculated 0.5×10^6 4T1-luc-GFP cells orthotopically in a no. 9 mammary fat pad of female BALB/c mice that was surgically exposed while mice were anesthetized. We have previously established that disseminated metastases are developed within 14 days of 4T1 inoculation.[14–16,53] At that point, the primary tumor was resected. The other three models of metastasis were based on direct injection of cancer cells into blood circulation in nude or wild-type female mice. Tail vein injection of cancer cells resulted in colonization in the lung. Mice were injected *via* the tail vein with 5×10^5 metastatic D2.A1 or D2.OR cells. The animals were monitored on a daily basis to ensure that they did not suffer from any adverse effects resulting from tumor inoculation.

2.3.4 Bioluminescence Imaging

Using the IVIS Spectrum system, bioluminescence imaging (BLI) was performed 10 min after intraperitoneal administration of 200 μl of D-luciferin (10 mg/ml). BLI was performed every 3-7 days until the terminal point of the study. At the terminal point, organs were extracted for *ex vivo* organ imaging or histological analysis.

2.3.5 Fluorescent Imaging Ex Vivo

Lungs were imaged *ex vivo* using the IVIS Spectrum system. Briefly, mice were injected with a dose containing ~5.3×10^{11} nanoparticles of each formulation. Each nanoparticle formulation was labeled with Alexa 647. Using phantoms of each nanoparticle variant, the IVIS Spectrum system was calibrated to take quantitative deposition measurements of regions with lung metastasis. After 3 h from nanoparticle injection, the animals were anesthetized with an IP injection of ketamine/xylazine and transcardially perfused with PBS. After the organs were explanted, the lungs were precisely sliced in 500 μm sections using a mouse brain slicer. We confirmed that this low tissue thickness nearly eliminated losses of fluorescence signal. Organs from animals injected with saline were also imaged to determine background fluorescence at all excitation wavelengths. This enabled quantitative *ex vivo* imaging of the nanoparticle concentration in the lungs.

2.3.6 Histological Evaluation

Immunohistochemistry was performed to evaluate the expression of $\alpha_v\beta_3$ integrin and EGFR in D2.A1 metastasis in the lungs. Serial tissue sections were stained with the nuclear stain DAPI and the specific antibody for $\alpha_v\beta_3$ integrin or EGFR.

2.3.7 Radiolabeling of Nanoparticle

Silica nanoparticles were prepared by using a base-catalyzed sol–gel process. Functionalization of the nanoparticles with the four targeting ligands was performed using

the four peptides described above *via* standard conjugation chemistry. Briefly, 2 mg of silane-PEG-maleimide was dissolved in 2 mL of deionized water and separated into 4 equal volumes. A 1.5X molar excess of each desired peptide was dissolved in each container and allowed to react with the silane-PEG-maleimide for 2 hours. Completion of the reaction was confirmed using thin layer chromatography (TLC). Finally, the peptide-PEG-silane conjugates and 1 mg of silane-PEG-NH_2 were added to the silica particles and allowed to react for 24 hours.

No carrier-added (n.c.a) [^{18}F] fluoride was produced by a cyclotron via the nuclear reaction ^{18}O (p,n) ^{18}F. At the end of bombardment, the activity of aqueous [^{18}F]fluoride (50-100 mCi) was transferred to the GE Tracerlab FXn synthesizer by high helium pressure. After delivery, the radioactive solution was passed through a Sep-Pak light QMA cartridge and was eluted by K_2CO_3 solution (6 mg in 0.6 ml water) followed by K_{222} solution (12 mg in 1 ml acetonitrile). The solvent was evaporated under a steam of helium at 85 ^{o}C for 5 min and the residue was vacuumed at 55 ^{o}C for another 3 min to get the anhydrous K_{222}/ [^{18}F] complex. A solution of the triflate salt of tert-butyl 4-N,N,N-triethylammoniumbenzoate (1, 5mg in 0.5 mL of anhydrous acetonitrile) was added to the above dried complex, and the mixture was heated at 100^{o}C for 10 min. Afterwards, tetratylammonium hydroxide solution (TBAH, 20µl in 0.5 mL acetonitrile) was added and heated at 100 °C for 10 min. The solvent was then removed and N,N,N',N'-tetramethyl-O-(N-succinimidyl)uronium tetrafluoroborate (TSTU, 10mg in 1 ml MeCN) was added and heated at 100 °C for 10 min. After cooling down, 8 mL of 5% acetic acid was added and the resulting mixture was loaded onto a Sep-Pak plus C18 cartridge, which was then washed with 10 ml water and 10 ml 10% MeCN. The crude [^{18}F]SFB was eluted with 1

mL of acetonitrile which was further purified by semi-preparative HPLC (Phenomenex C-18, 10 mm × 250 mm, acetonitrile : water (0.01%TFA) = 1:1, flow rate of 3 ml/min, t_R=11.5 min). The radioactive fraction containing the desired products was collected, diluted with water, loaded onto a Sep-Pak C-18 cartridge and eluted with 1 ml acetonitrile. After evaporation, the residue was reconstituted in 0.1 mL DMSO, mixed with 0.1 mg of MSN nanoparticles and 20 μL DIPEA. The mixture was reacted at 40 °C for 10 min, the radiolabeling yield were 80~91% (n=6) as determined by thin layer chromatography (TLC).

2.7 PET Imaging

MicroPET/CT imaging was performed using a Siemens Inveon microPET/CT scanner. For better anatomic localization, CT co-registration was applied. Before microPET imaging, CT scout views were taken to ensure the whole body of the mouse was placed in the co-scan field of view (FOV) where the highest image resolution and sensitivity are achieved. Under anesthesia, radiotracer (200 μCi, 0.2 ml) was administered *via* tail vein injection, and immediately followed by a PET acquisition up to 120 min. After the microPET acquisition was done, the mouse was moved into the CT field and a two-bed CT scan was performed. A two-dimensional ordered subset expectation maximization (OSEM) algorithm was used for image reconstruction using CT as attenuation correction. For quantitative analysis, the resultant PET images were registered to the CT images, which enabled us to accurately define the ROI and quantify the radioactivity concentrations.

2.3.8 Statistical analysis

Means were determined for each variable in this study and the resulting values from each experiment were subjected to one-way analysis of variance with *post hoc* Bonferroni

test (SPSS 15, Chicago, IL). A P value of less than 0.05 was used to confirm significant differences. Normality of each data set was confirmed using the Anderson-Darling test.

2.4 Results and Discussion

2.4.1 Histological evaluation of vascular biomarkers

In this work, we explored a multi-ligand targeting strategy to target a nanoparticle to four different vascular markers related to metastasis. The selected targets involve surface receptors on the remodeled endothelium as well as foci resident on the endothelium of metastasis. Metastatic TNBC displays a highly heterogeneous cellular population, including rapidly dividing cancer cells, cancer stem cells and dormant disseminated cancer cells.[12,70] To consider the dynamic and complex nature of metastatic TNBC, we sought to target upregulated biomarkers expressed by metastatic TNBC cells (*e.g.*, EGFR, $\alpha_v\beta_3$ integrin), the remodeled endothelium associated with metastasis (*e.g.*, P-selectin, $\alpha_v\beta_3$ integrin), and the extracellular matrix in near-perivascular regions of metastasis (*e.g.*, fibronectin). In addition to the adhesion-specific biomarkers on the remodeled endothelium of metastasis, [23,71–80] TNBC cells carry a continuously evolving phenotype including varying overexpression of cell surface receptors. Specifically, EGFR contributes to tumor formation, invasiveness and metastasis and is overexpressed in ~70% of TNBC patients.[81–89] .

To assess the expression of vascular biomarkers on the endothelium associated with metastasis, we performed histological analysis in two mouse models of metastatic TNBC. **Fig 2.2** shows representative images in the 4T1 and D2.A1 mouse models. The main findings are summarized here: 1) After identifying clusters of cancer cells dispersed in the lungs, cancer cells were found on vascular beds. 2) These vascular beds were exactly the locations with highly targetable $\alpha_v\beta_3$ integrin, P-selectin, fibronectin and EGFR. Abundance and selective perivascular expression of all four biomarkers could be seen in

regions with cancer cells. 3) These biomarkers were not observed on the endothelium of healthy lung tissues, which indicates that they are highly selective vascular targets associated with metastasis. The histological analysis shown in **Fig 2.2** illustrates the presence of these four biomarkers on the vascular beds of locations with metastatic TNBC in different animal models, indicating their availability for vascular targeting of nanoparticles.

2.4.2 Nanoparticle targeting variants for fluorescence imaging

In the first set of studies, we used a liposomal nanoparticle with a composition and size identical to previously published work[15]. We prepared 100-nm liposomes using established methods.[15,26,37,42,65,66] To be detectable in the fluorescence imaging studies, the nanoparticle variants were labeled with the Alexa 647 fluorophore that contained an NHS functional group. The fluorophore was conjugated directly onto the lipid DSPE. To ensure for complete conjugation of the entire amount of DSPE with the Alexa fluorophore, a 2-fold molar excess of fluorophore was used over DSPE. Completion of the reaction was confirmed by thin layer chromatography (TLC). The final levels of the fluorescent label on the nanoparticles were directly measured using the Spectrum In Vivo Imaging System (IVIS, Perkin Elmer). Further, there was no change in the fluorescence signal of the nanoparticle formulations during a 24 h dialysis, indicating stable fluorescence labeling.

The average diameter of the nanoparticles and their targeting variants was verified by dynamic light scattering and determined to be ~103 nm (with a polydispersity index of 0.027). The nanoparticle variants included an $\alpha_v\beta_3$ integrin-targeting nanoparticle (RGD-NP), a P-selectin-targeting nanoparticle (PSN-NP), an EGFR-targeting nanoparticle (EGFR-NP), a fibronectin-targeting nanoparticle (CREKA-NP), an EGFR and $\alpha_v\beta_3$

integrin-targeting nanoparticle (dual-NP), and a quadruple-targeting nanoparticle (multi-NP). As ligands, we selected peptides that bind specifically and with high affinity to $\alpha_v\beta_3$ integrin (RGD), P-selectin (PSN), fibronectin (CREKA), and EGF receptor (EGFR). More specifically, the $\alpha_v\beta_3$ integrin-targeting peptide c(RGDfC), [14,15,32] P-selectin-targeting peptide CDAEWVDVS, [15,24,33] fibronectin-targeting peptide CREKA,[29] and EGFR-targeting peptide CYHWYGYTPQNVI,[17,34] were used. Before preparing liposomes, the DSPE-PEG-ligand was synthesized separately for each peptide. Briefly, peptides was conjugated on the distal end of DSPE-PEG-NH_2 using standard conjugation chemistry as reported previously.[15] In previous studies, we have confirmed the structure of similarly synthesized conjugates using MALDI-MS and NMR.[40,69] The thiol of the cysteine residue on the peptide was conjugated to the amine of DSPE-PEG-NH_2 *via* the heterobifunctional crosslinker sulfo-SMCC, which is reactive towards amine and sulfhydryl groups. To guarantee complete conjugation of the DSPE-PEG-NH_2 with the peptide, we used a two-fold molar excess of the peptide over DSPE-PEG-NH_2. The progression of the reaction was monitored using thin layer chromatography (TLC), which confirmed complete conjugation of the entire amount of DSPE-PEG-NH_2 with the peptide. TLC was carried out on silica gel coated fiber sheets using a mixture of chloroform/methanol as the mobile phase. DSPE-PEG-NH_2 traveled a short distance (Rf=0.2), whereas the free peptides migrated to closer to the solvent front (Rf =0.75-0.9 depending on the peptide). In addition, iodine vapor staining, spots were also ninhydrin positive. The products appeared in a new spot (Rf=0.5-0.6). At the end of the reaction, there was only the spots of DSPE-PEG-peptide and the remaining excess of peptide. The absence of a spot at Rf=0.2 indicated the

complete depletion of DSPE-PEG-NH_2. The excess peptide was completely removed using a 1-day dialysis against PBS.

These conjugates were then conveniently and accurately added to the recipe for each nanoparticle variant. Using Bio-Rad Protein Assay and Coomassie Blue G-250 dyes, the number of peptides on the nanoparticle variants was determined. The single-ligand nanoparticles contained ~2,000 peptides per particle, whereas the dual-ligand variant had a total ~4,200 peptides per particle. The quadruple-ligand NP contained a total number of ~5,800 peptides per particle with the four peptides having an equal share.

We should note that the DSPE-PEG-ligands were dissolved and well-mixed with the rest of the lipids in ethanol before hydration and formation of liposomes. The Bio-Rad Protein Assay confirmed the amounts of DSPE-PEG-peptide, indicating negligible losses during extrusion. While we didn't measure the surface distribution of the different types of ligands relative to each other dual and multi-ligand nanoparticles, we assumed that there was uniform distribution of the peptides because the different types of peptides did not exhibit greatly different sizes and charges. Overall, in the case of the dual- and quadruple-ligand nanoparticles, we sought to ensure the ligand density for each type of peptide by using an equal ratio for the two or four ligand conjugates. Zeta potential measurements revealed a near neutral charge for these liposomes (about 2-4 mV), indicating that all the amines were conjugated with peptides.

2.4.3 Evaluation of Targeting Efficacy of Different Nanoparticle Variants In Vivo

For these studies, we used the 4T1 model, which is one of the standard models to study the development of metastatic TNBC in immunocompetent mice. After inoculation

in a mammary fat pad, 4T1 tumors rapidly develop spontaneous metastases at organ sites reminiscent of those observed in human patients.[14–16,64] The primary tumor was then surgically removed, so that metastatic disease could be studied in an animal setting comparable to the adjuvant clinical scenarios where the primary tumor is removed, and metastatic foci remain intact. Further, the 4T1 cells stably expressed fluorescent and bioluminescent reporter genes, which were needed to longitudinally track the dissemination and growth of developing metastasis in mice. **Fig 2.3**A shows representative bioluminescence (BLI) images of a mouse bearing a 4T1 tumor indicating the timeline of metastatic progression. Once BLI imaging indicated that metastasis was present in the lungs (day 16), a nanoparticle formulation labeled with Alexa 647 was systemically injected into the animal. To quantitatively image the fluorescence signals from nanoparticles deposited in metastases, we used the IVIS Spectrum system to image the lungs *ex vivo.* Our previous studies have showed that maximum deposition of targeted nanoparticles onto the endothelium of metastasis occurs within 3 h post-injection.[15,16] After 3 h from injection of the nanoparticles, lungs were perfused, excised and precisely sliced in 500-μm sections using a mouse organ slicer. Phantom studies confirmed that the 500-μm tissue thickness resulted in negligible attenuation of fluorescence signal, enabling accurate quantification of the concentration of each nanoparticle variant in metastatic sites in the lungs. **Fig 2.3**A shows representative images of the deposition of CREKA-NP and multi-NP in the lungs.

We quantitatively evaluated the different targeting variants of the nanoparticles in the 4T1 mouse model at a time point representing the early spread of metastatic disease (day 16 after tumor inoculation). Using calibrations from phantoms of the Alexa 647-

labeled nanoparticles, quantitative measurements of the nanoparticle were taken from lung slices. Lungs from animals injected with saline were also imaged to determine background fluorescence at the selected excitation wavelengths. Furthermore, the accuracy of the quantitative measurements of the fluorescence imaging method was confirmed by directly measuring the concentration of deposited nanoparticles in the tissues in a separate study (n=4). Specifically, besides the surface Alexa 647 label, a red fluorophore was encapsulated into the nanoparticle. Using the same methodology, 3 h after injection, the lungs were perfused, excised, sliced in 500-μm sections and imaged with the IVIS Spectrum system. The lung sections were then homogenized and the secondary label was extracted following established methods.[64,90,91]

Specifically, we compared the quadruple-ligand nanoparticle targeting all four biomarkers to its single-ligand nanoparticle variants targeting only one of the four biomarkers and a dual-ligand nanoparticle targeting EGFR and $\alpha_v\beta_3$ integrin. All formulation were injected at the same dose containing ~5.3×10^{11} nanoparticles. The summary of the measurements is shown in **Fig 2.4**A (n=4-6 mice in each group). It should be noted that injection of the nanoparticles to healthy animals resulted in negligible signals (nearly baseline levels) from the lungs. Consistent with our previous studies,[15] the intratumoral deposition of the non-targeted nanoparticles (NT-NP) resulted in low levels (1.26% of dose), indicating low EPR-driven deposition into early metastasis. On the other hand, all four single-ligand nanoparticle variants achieved higher levels of deposition in lung metastasis, which was about 2.5% of the injected dose of nanoparticles. Notably, the deposition among the four single-ligand variants was statistically insignificant. Among the four potential ligand combinations to generate dual-ligand nanoparticles, we selected

EGFR and $\alpha_v\beta_3$ integrin, which represent two diverse biomarkers, including receptors on metastatic TNBC cells (*i.e.*, EGFR, $\alpha_v\beta_3$ integrin) and receptors on the remodeled endothelium metastasis (*i.e.*, $\alpha_v\beta_3$ integrin). The dual-ligand nanoparticle resulted in a nearly 2-fold higher deposition into lung metastases than its single-ligand counterparts. Finally, the multi-NP particle significantly outperformed all the formulations achieving a deposition of ~7% of the injected nanoparticles into lung metastases. It is important to mention that we sought to maintain a reliable assay system by selecting animals with very similar metastatic burden as shown in **Fig 2.4**B.

While the averaged values of entire groups provided useful information, examination of the lung deposition for each animal separately provided further insights (**Fig 2.4**C). When we looked closely at the single-ligand formulations, the targeting efficacy was very inconsistent. For instance, EGFR-NP achieved a deposition of 0.97% of injected dose into lung metastases of one animal and 4.34% in another animal, which represents a nearly 450% difference between those two animals. Similar observations can be made for the other single-ligand formulations. In the case of the dual-ligand nanoparticle, the targeting efficacy was higher than the single-targeting variants with significant consistency among all animals. Most notably, the multi-ligand nanoparticle targeting all four biomarkers consistently achieved the highest deposition in lung metastases for all the animals ranging from 6.1-8.4% of the injected dose.

Comparing the non-targeted to the CREKA-targeted nanoparticle variant, the organ distribution was similar in mice bearing 4T1 metastasis (**Fig 2.4**D). For both formulations, the majority of the particles ended up being cleared by the organs of the reticuloendothelial

system (liver and spleen), while the nanoparticle levels in the heart and kidneys were very low. As expected, the presence of peptide on the CREKA-NP accelerated the particle's recognition and clearance as indicated by the higher levels in the liver compared to the non-targeted variant.

Rather than targeting cancer cells in the tumor interstitium, we sought to target biomarkers on the endothelium associated with metastatic disease. Generally, traditional targeting schemes seek to direct nanoparticles onto upregulated receptors on the cancer cells in the tumor interstitium. Unfortunately, the microenvironment of early metastasis lacks the leaky endothelium often found in solid tumors and therefore passive intratumoral deposition of nanoparticle is not favored.[15,16] As a consequence, 'deep-tissue' targeting of surface receptors on cancer cells is limited in early and transient metastasis. On the other hand, the remodeled endothelium associated with metastasis serves as the early and obvious targetable site of the disease. While our targeting studies in **Fig 2.4** show that the single-ligand nanoparticle variants exhibited significant deposition into metastatic sites, the targeting efficacy was not consistently high in all the animals. To further increase targeting efficacy, we demonstrated in a previous study[15] that a dual-ligand nanoparticle can target two receptors overexpressed in metastasis facilitating effective targeting of metastatic disease that was otherwise missed by single-ligand strategies. In fact, the dual-ligand strategy was able to account for spatiotemporal alterations in the expression patterns of the targetable receptors in metastatic sites. Here, we further expanded from two to four different targeting ligands on the same nanoparticle. Compared to all the single-ligand and the dual-ligand nanoparticle variants, the four-ligand nanoparticle achieved consistently higher targeting of metastatic disease.

2.4.4 PET Imaging

Finally, we sought to evaluate the ability of the multi-ligand nanoparticles to target and detect metastasis at its very early stages of development. While fluorescence labelling provided sufficient contrast sensitivity to be able to image the nanoparticles *ex vivo*, targeting of the very early spread of the disease requires even higher sensitivity. Thus, we employed radiolabeling and radionuclide-based imaging due to its extraordinary sensitivity (down to the picomolar level).[92] More specifically, positron emission tomography (PET) exhibits many advantages, including high sensitivity and deep tissue penetration.[92,93] To evaluate the performance of the multi-ligand targeting strategy, we used mice bearing different models of breast cancer metastasis, representing a broad range of the disease. In this study, we included mice with D2.A1, D2.OR and 4T1 metastasis in the lungs as well as healthy mice (n=6). In addition to the 4T1 model, the D2-Hyperplastic Alveolar Nodules (HAN) series consists of metastatic D2.A1 cells and their isogenic and dormant D2.OR counterparts. The D2.0R cells differ dramatically in their ability to initiate metastatic outgrowth in the lungs of syngeneic Balb/C mice.[94,95] Dormant breast cancer cells are "potential time bombs" that remain in quiescent/senescent states for long periods of time prior to initiating their "explosive" metastatic outgrowth. Representative BLI images show the vast difference of the progression of the disease in the D2.A1 and D2.OR models (**Fig 2.5**).

The multi-ligand nanoparticle was radiolabeled with [^{18}F]fluoride, which was produced by an on-site cyclotron. In addition to the four ligands (~500 ligands of each ligand type per particle), we left 100 PEG-amines on each particle available for conjugation with the [^{18}F] label (**Fig 2.6**A). In the first step of the radiochemistry (**Fig 2.6**B), N-

succinimidyl 4-[^{18}F]fluorobenzoate ([^{18}F]SFB) was synthesized, which was purified by semi-preparative HPLC (Phenomenex C-18, 10 mm × 250 mm, acetonitrile : water (0.01%TFA) = 1:1, flow rate of 3 ml/min, t_R=11.5 min). Having an NHS ester, [^{18}F]SFB reacts effectively with the available amines on the nanoparticles. The radiolabeling yield was 80-91% (n=6 batches), as determined by thin layer chromatography (TLC).

To resemble the early-stage development of metastatic disease, we used mice bearing lung metastasis of 4T1 (Day 10), D2.A1 (Day 7) and D2.OR (Day 35) cancer cells. **Fig 2.8** shows that the BLI photon count from the regions with metastasis was very low (~10^5 p/sec/cm^2/sr). The radiolabeled multi-ligand nanoparticle (200 µCi, 0.2 ml) was administered *via* tail vein injection, and immediately followed by a PET acquisition for 120 min. MicroPET/CT imaging was performed using a Siemens Inveon microPET/CT scanner. For anatomic localization, CT co-registration was applied. After the microPET acquisition was done, the mouse was moved into the CT field and a two-bed CT scan was performed. **Fig 2.7** (**top raw**) shows representative coronal images of the mice 1 h after administration of the multi-ligand nanoparticles. PET imaging showed that vascular targeting of the nanoparticle resulted in "hot spots" in the lungs of all the mice with metastasis. As expected, the liver also displayed significant signal, since nanoparticles are cleared by Kuppfer cells in the liver (**Fig 2.9)**. It should be emphasized that the thoracic region of healthy animals exhibited no signal, indicating the absence of non-specific accumulation of the multi-ligand nanoparticles in healthy lungs. Further, there was no signal from the heart 60 min after injection of the agent as shown in the pharmacokinetic profile of the agent in **Fig 2.10**. Most importantly, the findings of *in vivo* imaging were verified by *ex vivo* organ imaging. The lungs of the mice were perfused and excised after

the last PET imaging session. Planar fluorescence imaging confirms the presence and topology of early metastasis (**Fig 2.7, bottom raw**). In addition, *ex vivo* PET imaging of lungs confirmed that the signal is from cancerous tissues in the lungs (**Fig 2.11**).

It is important to note that it is essential for a nanoparticle to be able to target 'clinically silent' micrometastatic disease. Numerous retrospective studies with long-term follow-up showed increased mortality in breast cancer patients with micrometastasis.[96–100] Thus, it is essential to evaluate the risk of an individual patient of harboring clinically silent micrometastatic disease. An accurate diagnostic testing would be deployed for use in early-stage disease to optimally assess the risk of patients and impact treatment decisions for optimal local control. In more advanced disease scenarios, such imaging would be used for guiding treatment decisions around locoregional versus systemic treatment. In conclusion, early and accurate detection of metastasis can become one of the most consistent prognostic factors in therapy decision-making.

As a case study for the multi-ligand nanoparticle, triple-negative breast cancer (TNBC) was selected, which is an extremely metastatic subtype of breast cancer with frequent relapse and shorter metastasis-free-survival. [101,102] In this context, our animal modeling included an extremely metastatic subtype of breast cancer (*i.e.*, metastatic TNBC) as well as dormant disseminated disease (*i.e.*, latent breast cancer). Our studies showed that an ^{18}F-labeled nanoparticle coupled with a four-ligand vascular targeting facilitated precise detection of early disease, transient and dormant metastatic disease. Using the extraordinary sensitivity of radionuclide imaging and a very low dose of the nanoparticles, PET imaging achieved remarkable diagnostic accuracy with high sensitivity

(*i.e.*, correctly identified all the animals with micrometastasis) and high specificity (*i.e.*, correctly identified healthy animals as not having the disease).

2.5 Conclusion

In conclusion, we explored a new paradigm on how to design multi-ligand nanoparticles to consider the complex, dynamic and heterogeneous microenvironment of metastatic disease. Compared to the non-targeted nanoparticle, all four variants of single-ligand nanoparticles achieved superior deposition into early metastasis. The dual-ligand nanoparticle achieved a nearly 2-fold higher deposition into metastasis than any of the single-ligand variants. Most notably, the four-ligand nanoparticle exhibited further and significant improvements, resulting in a nearly 3-fold higher deposition than the single-ligand nanoparticles (~7% of the injected dose). Finally, we demonstrated the diagnostic accuracy of the multi-ligand nanoparticle to detect 'clinically silent' micrometastatic disease using PET imaging, which exhibits high sensitivity. Overall, precise targeting of a nanoparticle imaging agent early-stage metastasis can be a companion diagnostic and provide prognostic and diagnostic value in therapy decision-making.

2.6 Figures

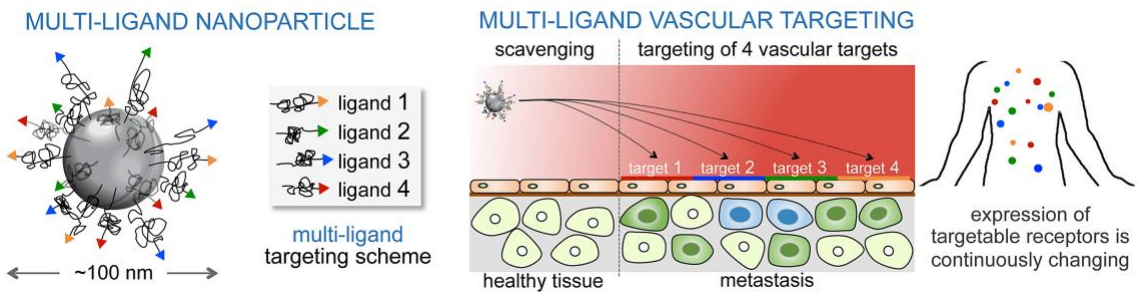

Figure 2.1 Illustration of the multi-ligand concept shows a nanoparticle capable of targeting the dynamic microenvironment of metastatic disease.

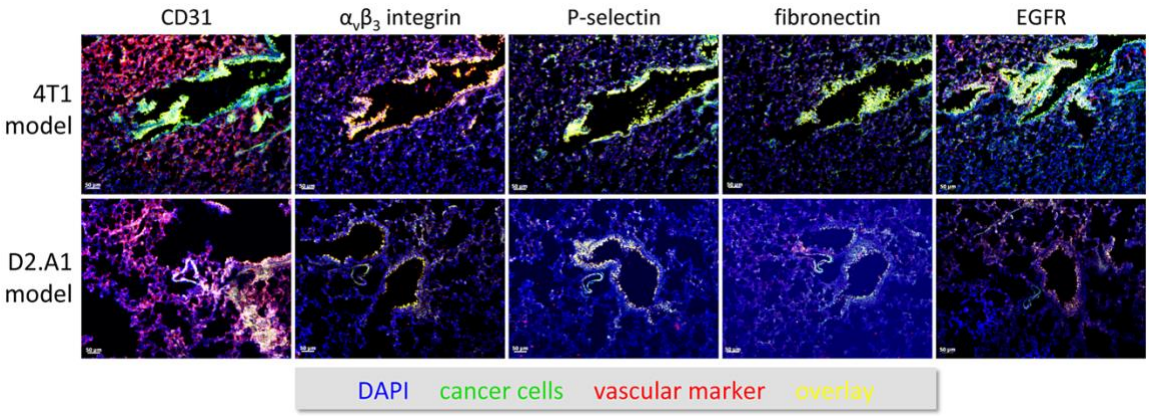

Figure 2.2 Histological evaluation of the microdistribution of vascular biomarkers in two mouse models of metastatic TNBC.

Representative fluorescence images of serial histological sections of lungs show the spread of metastatic cancer cells in mice bearing 4T1 metastasis (top) and D2. A1 metastasis (bottom). Location of metastatic cancer cells is shown with respect to endothelial cells and expression of $\alpha_V\beta_3$ integrin, P-selectin, fibronectin and EGFR (10× magnification; scale bar = 50 μm; blue: nuclear stain; green: cancer cells; red: CD31 endothelial marker or $\alpha_V\beta_3$ integrin or P-selectin or fibronectin or EGFR).

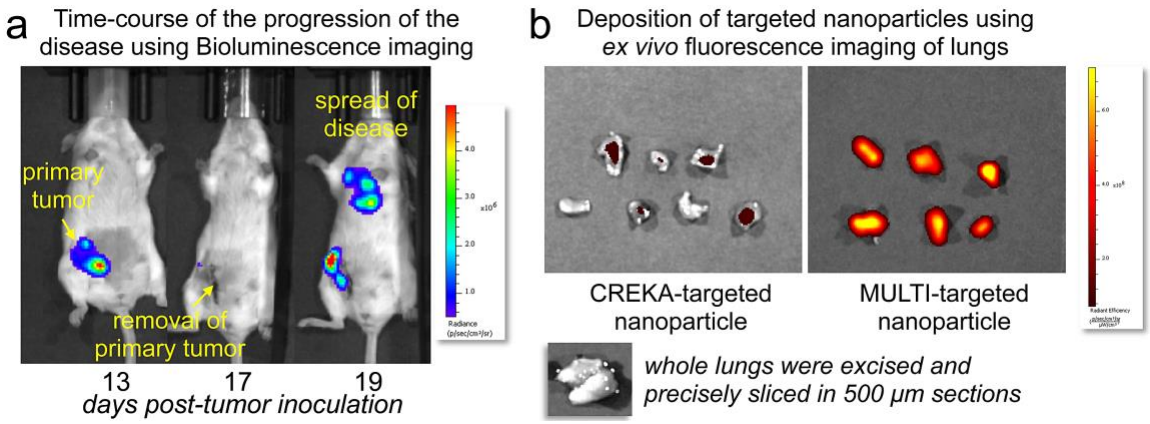

Figure 2.3 Representative in vivo bioluminescence (BLI) images and ex vivo fluorescence images of mice with 4T1 metastasis.

(a) BLI images of the same animal show the progression of 4T1 metastasis in the lungs of mice. (b) The nanoparticle targeting variants were labeled with Alexa 647. The particles were intravenously injected into animals with 4T1 metastasis. After 3 h from injection, lungs were perfused, excised, sectioned into thin slices of equal thickness and imaged ex vivo using an IVIS Spectrum system.

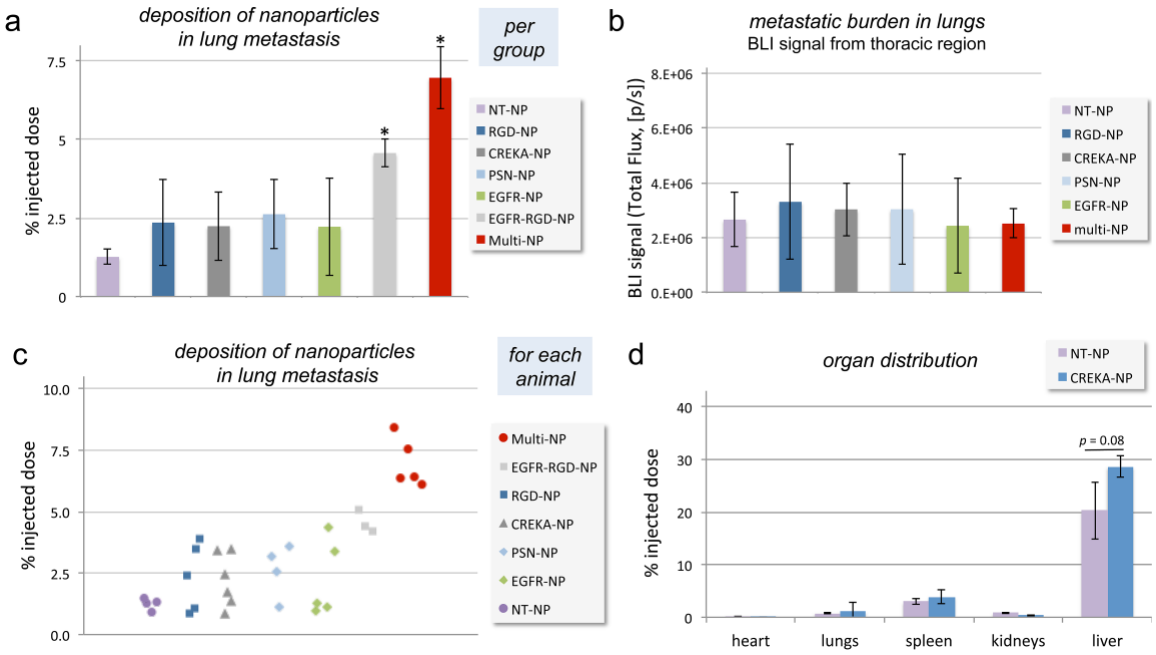

Figure 2.4 Quantitative evaluation of the ability of the nanoparticle targeting variants to target metastasis in the 4T1 mouse model.

(a) Each formulation was systemically administered via a tail vein injection at the same dose (NT-NP indicates the non-targeted nanoparticle). The fluorescence signal of the fluorescence images of the lung sections was quantified for each formulation at 3 h after injection (n = 5 mice). On the basis of phantom measurements of each formulation using the IVIS imaging system, the fluorescence signal was converted to nanoparticle concentration (mean ± SD; * indicates $p < 0.05$ by Student's t test; n = 4–6 mice per group). (b) The bioluminescence signal from the thoracic region of each animal was quantified and summarized for each group, representing the metastatic burden of the different groups used in the targeting studies. Data are presented as mean ± SD. (c) The nanoparticle deposition of the nanoparticle targeting variants in lung metastasis is presented separately for each animal. (d) Organ distribution of NT-NP and CREKA-NP was evaluated in the 4T1 mouse model (n = 5).

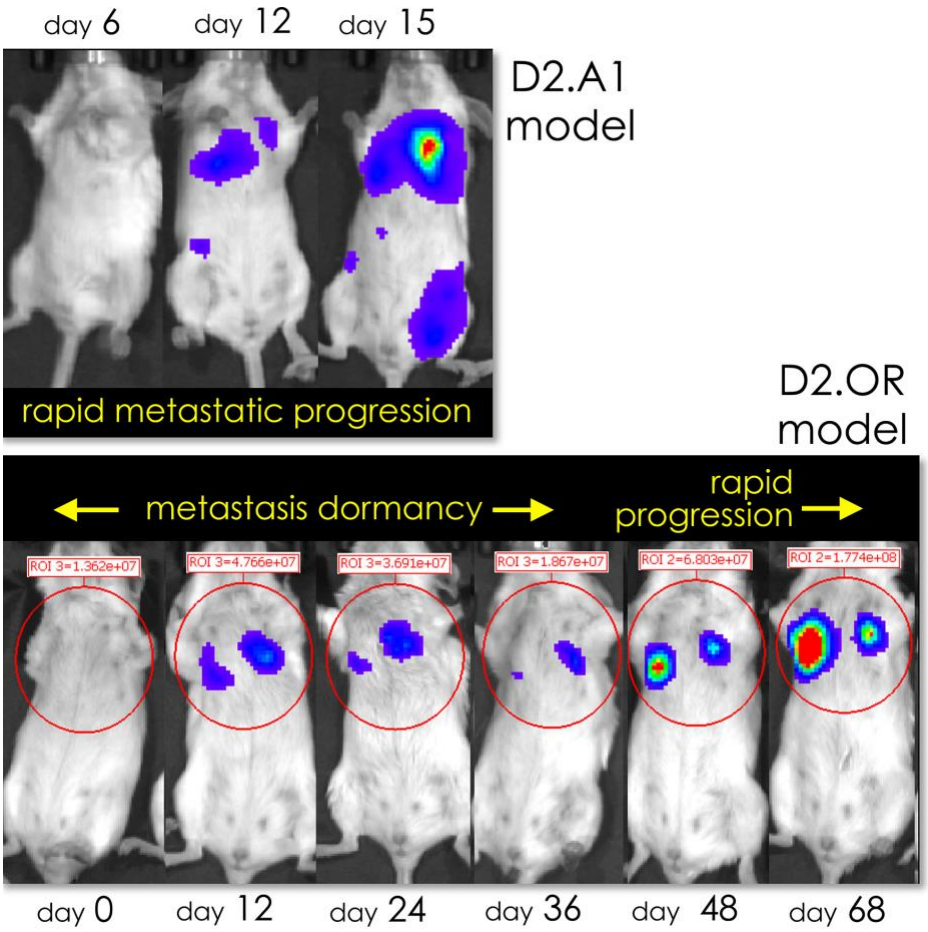

Figure 2.5 Representative BLI images shows the timeline of the progression of aggressive metastasis (top; D2.A1 model) and latent metastasis (bottom; D2.OR model) in the lungs of mice after tail vein injection of cancer cells.

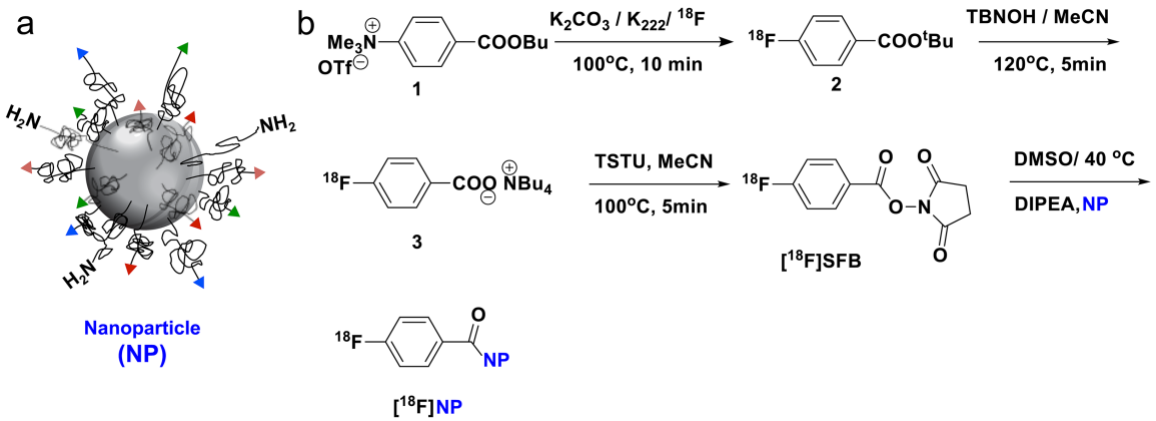

Figure 2.6 Radiolabeling of the multi-ligand nanoparticle with [^{18}F]fluoride.

(a) Illustration of the nanoparticles shows that incorporation of the functionalization with the 4 targeting peptides and the availability of a small number of amine groups on the nanoparticle's surface. (b) Reaction scheme of the radiochemistry shows the synthesis of [^{18}F]SFB and its conjugation onto the nanoparticles.

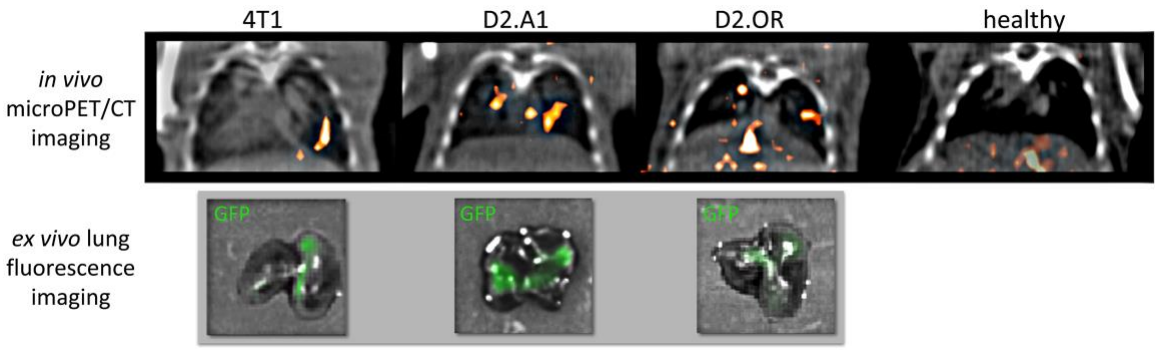

Figure 2.7 Imaging of micrometastasis using an 18F-labeled multi-ligand nanoparticle and PET.

Healthy mice and mice with 4T1 or D2A1 or D2.OR metastasis in the lungs were intravenously injected with a dose of 200 μCi (0.2 mL) of the radiolabeled multi-ligand nanoparticle, and immediately followed by a PET acquisition up to 120 min. PET/CT imaging was performed using a Siemens Inveon microPET/CT scanner. Coronal images show the thoracic region of the mice 60 min after injection of the nanoparticles (top raw). At the end of the PET imaging session, the lungs of the animals were perfused, excised and imaged ex vivo using a CRi Maestro fluorescence imaging system, indicating the locations with metastasis in the lungs (bottom raw).

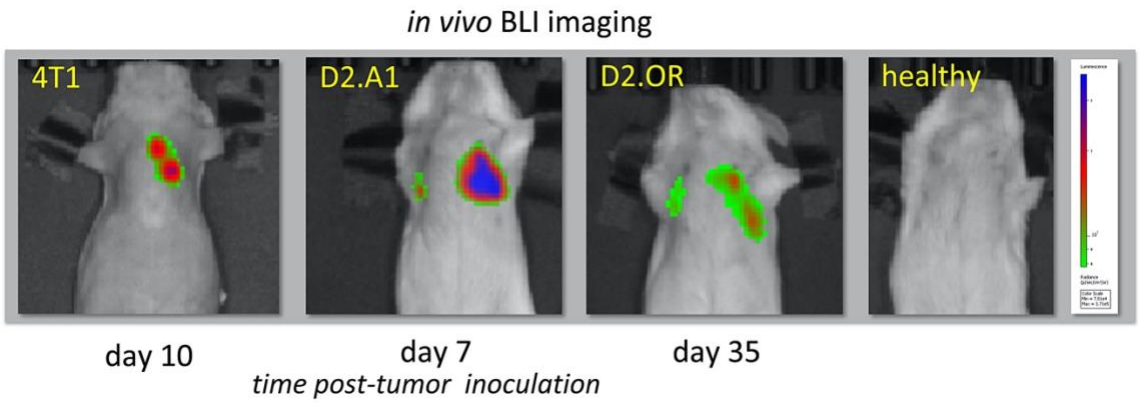

Figure 2.8 Bioluminescence (BLI) images show the metastatic burden in the lungs of various animals based on different types of breast cancer.

Fig. 2.7 shows the PET images of these animals after injection with the ^{18}F-labeled multi-ligand nanoparticles.

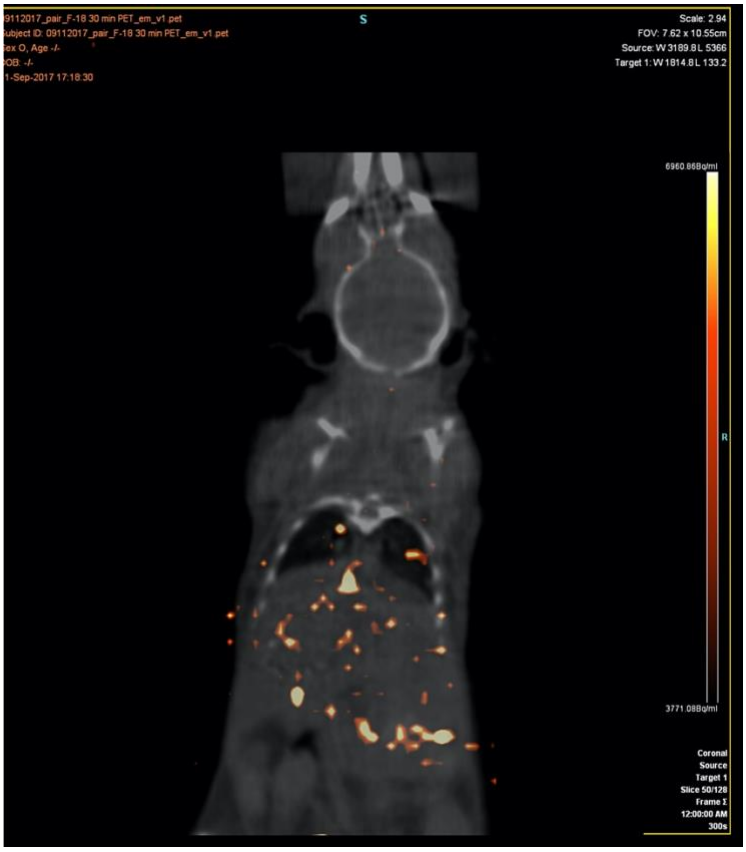

Figure 2.9 Coronal PET whole-body image shows a mouse 60 min after injection of the ^{18}F-labeled multi-ligand nanoparticles.

A mouse with D2.OR metastasis in the lungs was intravenously injected with a dose of 200 µCi (0.2 mL) of the radiolabeled multi-ligand nanoparticle, and immediately followed by a PET acquisition. PET/CT imaging was performed using a Siemens Inveon microPET/CT scanner.

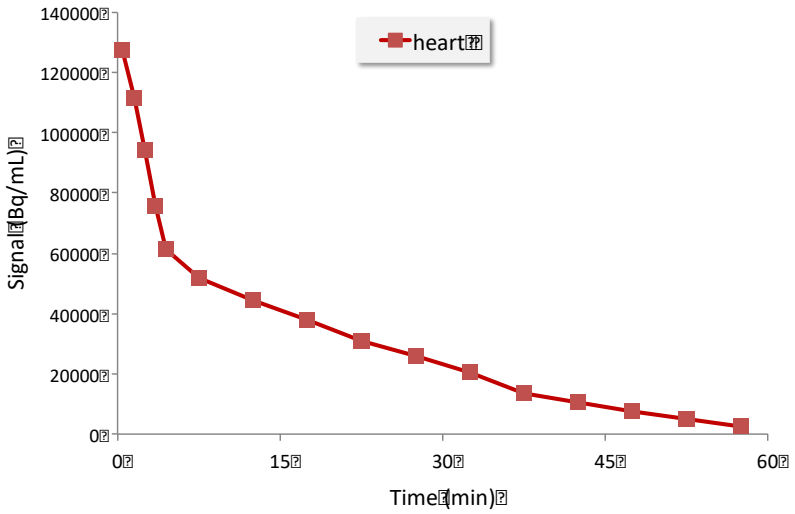

Figure 2.10 Quantification of the time-course of signal intensity in the heart is shown after injection of 200 µCi (0.2 mL) of the radiolabeled multi-ligand nanoparticle in healthy animals.

Figure 2.11 Representative PET image of lungs ex vivo.

A mouse with D2.A1 metastasis in the lungs was intravenously injected with a dose of 200 µCi (0.2 mL) of the radiolabeled multi-ligand nanoparticle, and immediately followed by a PET acquisition. To verify the findings of the *in vivo* imaging, mice were perfused and lungs were excised and imaged *ex vivo* using the Siemens Inveon microPET/CT scanner.

Chapter 3: Chemotherapeutic Delivery via Systemically Administered Tumor Targeted Nanoparticle Carriers

Effective Treatment of Cancer Metastasis Using a Dual-Ligand Nanoparticle
Gil Covarrubias, Felicia He, Shruti Raghunathan, Oguz Turan, Pubudu M. Peiris, William P. Schiemann, Efstathios Karathanasis

3.1 Abstract

Metastasis is responsible for the majority of deaths of breast cancer patients. While cytotoxic drugs are available with high potency to kill breast cancer cells, they are not designed to specifically seek and navigate in the dynamic and continuously changing microenvironment of metastatic disease. To effectively delivery chemotherapeutic agents to metastasis, we designed a dual-ligand nanoparticle loaded with doxorubicin by using two different types of ligands targeting EGFR and αvβ3 integrin. Metastatic cancer cells continuously change resulting in heterogeneity even across adjacent micrometastatic regions with variable expression of these targetable receptors. Using a mouse model of breast cancer metastasis, in vivo and ex vivo imaging showed that both EGFR and αvβ3 integrin-targeting were required to reliably direct the nanoparticle to metastasis and capture the spread and exact topology of the disease. Survival studies compared the anticancer efficacy of the standard drug, EGFR-targeting nanoparticle, αvβ3 integrin-targeting nanoparticle and the dual-ligand nanoparticle. While all the other treatments produced moderate therapeutic outcomes, treatment with the dual-ligand nanoparticle yielded significant improvement and event-free survival in a mouse model of breast cancer metastasis.

3.2 Introduction

Triple-negative breast cancer (TNBC) exhibits a very high risk of recurrence, resulting in disproportional mortality among breast cancer patients[60]. A total of 12–17% of newly diagnosed early breast cancers are TNBCs, corresponding to over 172,000 patients diagnosed annually worldwide[103,104]. Compared to other subtypes of breast cancer, metastatic relapse will occur in the majority of these patients following treatment [2,3]. Further, distant metastatic recurrence of TNBC (*m*TNBC) tends to occur in visceral organs, including the lungs, liver, and brain[2,3]. Due to its metastatic phenotype and characteristically high recurrence rate, nearly all women with metastatic TNBC will eventually die of their disease. This stems from the fact that traditional systemic therapies are not designed to specifically seek out and navigate into the hard-to-reach microenvironment of metastatic disease.

Since there are no targeted therapeutics available for TNBC, the standard-of-care is primarily based on systemic chemotherapy. While cytotoxic drugs are designed and selected based on their potency to kill cancer cells, they do not take under consideration the dynamic and continuously changing microenvironment of metastatic disease[25,105]. Even worse, the early stages of metastatic disease involves tiny colonies of cancer cells buried in healthy tissues[59], which makes early micrometastasis very challenging to target and differentiate from healthy tissues using drugs in their standard form. To increase drug delivery to tumor sites, targeting ligands have been used to direct deposition of drug-loaded nanoparticles to tumors that overexpress cancer-specific targetable receptors including folate, EGF, HER2, and integrin receptors. However, cancer cells at early micrometastatic

sites evolve and continuously change the expression of these targetable receptors[15,22,41,42,54–58,102].

Recently, we developed targeting schemes using multi-ligand nanoparticles to account for the spatiotemporal changes in the expression patterns of targetable receptors in metastasis[15,18,19]. Due to their nanoscale size, we showed that nanoparticles are ideal for incorporating more than one types of ligands on their surface at sufficiently high ligand density to achieve accurate targeting of their corresponding targeted receptor. By decorating the surface of the nanoparticle with more than one types of targeting ligands, multi-ligand nanoparticles exhibited highly precise targeting of different subsets of metastasis that predominantly express different targetable receptors at any given time that were otherwise missed by single-ligand strategies. For instance, a dual-ligand nanoparticle targeting EGFR and $\alpha_V\beta_3$ integrin can achieve a nearly 2-fold higher deposition into breast cancer metastasis in the lungs than its single-ligand nanoparticle counterparts[19]. We should mention that non-targeted nanoparticles achieve significantly lower deposition in metastasis than their single or dual-ligand targeting nanoparticle counterparts. This stems from the fact that the endothelium of early metastasis is not as leaky as observed in primary tumors. Our earlier studies focused on the imaging and diagnostic application of multi-ligand nanoparticles. Here, we exploit a dual-ligand drug-loaded nanoparticle for treatment of breast cancer metastasis (**Fig 3.1**). We selected a dual-ligand system using two peptides that target 1) EGFR, which is an overexpressed receptor on TNBC cells [81–89], and 2) $\alpha_V\beta_3$ integrin, which a receptor involved with the leukocyte adhesion cascade that circulating TNBC cells use to attach to the endothelium of future metastasis[23,71–74]. Considering the topology of these two receptors, the target sites involve surface receptors on metastatic foci

resident on the remodeled endothelium of micrometastasis[16,53,64]. As our nanoparticle, we chose the liposome, which is an all-purpose, highly versatile drug carrier with a long clinical history. Using a mouse model of metastatic TNBC, we demonstrate that the dual-ligand targeting scheme leads to precise and effective delivery of a clinically used cytotoxic nanoparticle (*i.e.*, liposomal doxorubicin) to different metastatic sites, which are typically missed by the free unmodified drug or single-ligand drug-loaded nanoparticle.

3.3 Methods and Materials

3.3.1 Nanoparticle Fabrication

To prepare DSPE-PEG-ligand conjugates, the c(RGDfC)[16] or the CYHWYGYTPQNVI[17] peptide (Peptides International) was conjugated to DSPE-PEG-NH_2. Using the cross-linker sulfo-SMCC (Thermo Fisher Scientific), the amine of DSPE-PEG-NH_2 reacted for 2 h with the thiol of the cysteine residue on the peptides. Sulfo-SMCC contains an amine-reactive *N*-hydroxysuccinimide (NHS ester) and a sulfhydryl-reactive maleimide group to form stable amide and thioether bonds. To guarantee complete conjugation of DSPE-PEG-NH_2, the peptide was at a 2-fold molar excess over the PEG. To remove unreacted peptide, the conjugates were dialyzed for 1 day against PBS. The completion of the reaction was confirmed using thin layer chromatography (TLC). TLC was carried out on silica gel coated fiber sheets using a mixture of $CHCl_3$/MeOH as the mobile phase. More details can be found in previous publications[15,19].

We prepared 100-nm liposomes encapsulating doxorubicin (DOX) using standard intraliposomal stabilization technology[69,90]. A lipid composition of DPPC, cholesterol and DSPE-PEG(2000)-ligand in the molar ratio of 60-X:40:X was used. For the single-ligand or dual-ligand nanoparticle variants, X was 2.5 or 5%, respectively. An equal ratio of the two DSPE-PEG-peptide conjugates was used in the case of the dual-ligand nanoparticle. The lipids were dissolved in ethanol and hydrated with 300 mM ammonium sulfate at 60 ℃ followed by sequential extrusion in a Lipex Biomembranes Extruder (Northern Lipids, Vancouver, Canada). Finally, DOX was loaded into the liposomes across a gradient of the inner phase (pH 4.0) and the extraliposomal phase (pH 7.5). Following dialysis to establish an ammonium sulfate gradient, the liposome suspension was mixed with DOX for 30 min

at 60℃. The liposomes were dialyzed against PBS for 1 day using a 100 kDa MWCO dialysis tubing (Spectrum Laboratories, CA). The size of the nanoparticles was characterized using dynamic light scattering (DLS, Brookhaven Instruments). The number of peptides on each nanoparticle variant was measured using a direct protein assay (Bio-Rad Protein Assay using Coomassie Blue G-250 dyes).

The nanoparticle variants were labeled with either an NIR fluorophore (Vivotag-S 680 or 750) or an Alexa fluorophore (Alexa 647 and 750), which contained an NHS functional group (Perkin Elmer)[15]. The fluorophore was conjugated directly onto the lipid 1,2-Distearoyl-sn-glycero-3-phosphoethanolamine (DSPE) in chloroform at 55℃ in the presence of triethylamine. A 2-fold molar excess of the fluorophore was used over DSPE. Thin layer chromatography confirmed completion of the reaction. Following evaporation of the solvent, the lipids were used as part of the lipid matrix at 2.5 mol%. The unreacted fluorophore was eventually removed after formation of the liposomes using dialysis. The final level of the fluorescent label of liposome variant was measured using the Fluorescence Molecular Tomography (FMT) or the Spectrum In Vivo Imaging System (IVIS, Perkin Elmer).

3.3.2 Animal Model

All animal studies were conducted under a protocol approved by the Institutional Animal Care and Use Committee (IACUC) at Case Western Reserve University. The well-being of the animals took priority over precise measurements in decisions regarding euthanasia or other interventions. We used a mouse-syngeneic tumor model based on the D2.A1 breast cancer cells. The D2.A1 cancer cells were obtained from Dr. Fred Miller

(Barbara Ann Karmanos Cancer Institute, Detroit, MI; ref.[106]). The D2.A1 cells stably expressed firefly luciferase and green fluorescent protein (GFP). Female BALB/c mice were injected *via* the tail vein with 5×10^5 D2.A1 cells. After tumor implantation, mice were randomized into groups for subsequent studies. Bioluminescence imaging was performed every 3–7 days to monitor the progression of metastatic disease. Images were collected 10 min after intraperitoneal administration of 200 μl of D-luciferin (10 mg/ml) using an IVIS Spectrum system. Bioluminescence imaging (BLI) was performed every 3–7 days until the terminal point of the study. The animals were closely monitored on a daily basis to ensure they did not suffer adverse effects resulting from tumor inoculations.

3.3.3 Animal Research Ethics Statement

All animal procedures were conducted under a protocol approved (#2015–0116) by the Institutional Animal Care and Use Committee (IACUC) at Case Western Reserve University. The well-being of the animals took priority over continuation of planned interventions. All animals received standard care, including ad libitum access to food and water, a 12/12 light/dark cycle, appropriate temperature and humidity. All animals received standard care ensuring proper protocol guidelines were followed. The animals were closely monitored on a daily basis to ensure they did not suffer adverse effects resulting from tumor inoculations. The well-being of the animals took priority over precise measurements in decisions regarding euthanasia. All procedures were conducted using anesthetic to minimize pain and distress. The inhalant anesthetic, isoflurane, was used as the primary anesthesia in our experiments. However, developing tumors may ultimately result in some level of distress or discomfort in these mice. If, during the time following tumor inoculation the animal showed signs of post-procedure pain, the animal was euthanized. The research

team, as well as the veterinary team of the animal facility, diligently monitored the condition of the animals, and removed any animal exhibiting signs of pain or distress as soon as humanly possible. When an animal showed distress or stopped eating and drinking (visually evaluated or there was a 15% loss of body weight), the animal was immediately euthanized. If it was observed that the tumor became 10% of the body mass of the animal or if there were changes in grooming, weight, behaviors, or kyphosis, the animal was immediately euthanized. Additionally, if we observed that an animal was suffering from inactivity, prostration, labored breathing, sunken eyes, hunched posture, piloerection/matted fur, unresolving skin ulcers, abnormal vocalization when handled, emaciation or anorexia, the animal was immediately euthanized. In all cases euthanasia was carried out in a CO_2 chamber. Euthanasia was confirmed by cervical dislocation.

3.3.4 Fluorescence in vivo and ex vivo imaging

Following injection of a cocktail of the two single-ligand nanoparticle variants, FMT imaging was performed at multiple time points after (t = 0, 30 min and 3, 24 h). The cocktail contained equal number of particles of RGD-targeted and EFGR-targeted nanoparticles (RGD-NP and EFGR-NP). The mice were injected with a dose containing ~5.3×10^{11} nanoparticles of each formulation. For the *in vivo* imaging studies, the nanoparticle formulations were labeled with a different NIR fluorophore. Using phantoms of each formulation, the FMT was calibrated to take quantitative deposition measurements. For the *ex vivo* imaging studies, the IVIS Spectrum system was used to image the lungs *ex vivo*. After injection of a cocktail containing the two single-ligand nanoparticle variants, the animals were anesthetized with an IP injection of ketamine/xylazine and transcardially perfused with heparinized PBS followed by 4% paraformaldehyde in PBS. After the organs

were explanted, the lungs were precisely sliced in 500 μm sections using a mouse organ slicer. We have confirmed that negligible attenuation of fluorescence signal occurs through the 500-μm tissue thickness at the selected excitation wavelengths[19]. All the lung slices of each animal were imaged with the IVIS system to quantitatively assess the deposition of the various targeted nanoparticle formulations in lung metastasis. Using calibrations from phantoms of the fluorescently labeled nanoparticles, the signal from each lung slice was quantified, then added together for the entire lung and finally converted to total accumulation of nanoparticles. As control, we used lungs from salineinjected animals to subtract background fluorescence at the selected excitation wavelengths.

3.3.4 Histological Evaluation

Histological analysis was performed to evaluate the microdistribution of fluorescently labeled RGD-NP and EGFR-NP in metastasis in the lungs of mice. Mice were anesthetized with an IP injection of ketamine/xylazine and transcardially perfused with heparinized PBS followed by 4% paraformaldehyde in PBS. Organs were explanted and post-fixed overnight in 4% paraformaldehyde in PBS. The tissues were soaked in 30% sucrose (w/v) in PBS at 4℃ for cryosectioning. Serial tissue sections of 12 μm in thickness were obtained. Using a fluorescence microscope, the tissue sections were imaged directly for green (GFP-expressing cancer cells), and the Alexa 647 and 750 fluorophore (nanoparticles). The tissue sections were imaged at 5, 10 or 20x on a Zeiss Axio Observer Z1 motorized FL inverted microscope. Immunohistochemistry was performed to evaluate the expression of $\alpha_V\beta_3$ integrin and EGFR in D2.A1 metastasis in the lungs. Serial tissue sections were stained with the nuclear stain DAPI and the specific antibody for $\alpha_V\beta_3$ integrin or EGFR.

3.3.5 Survival Study

Mice bearing D2.A1 metastasis were treated with EGFR-NP, RGD-NP or dual-ligand NP *via* tail vein injection at a dose of 7.5 mg/kg DOX at days 3, 4 and 5 after tumor inoculation. Control animals were treated with free DOX at a dose of 2 or 7.5 mg/kg. The tumor growth was allowed to progress until the animals showed changes in grooming, weight, behaviors, at which point animals were euthanized in a CO_2 chamber. Time of death was determined to be the following day.

3.3.6 Statistical Analysis

Statistics were performed in Prism version 7 for Mac (GraphPad Software, La Jolla, CA, USA). All the experiments were performed in triplicates unless stated otherwise. Data are represented as mean±s.d. Statistical significance between survival curves was determined using the log-rank (Mantel-Cox) test. In cases where data met the assumptions necessary for parametric statistics, analysis of differences between two groups was performed using two-tailed Student's t-test assuming equal variance. Data from three or more groups were analyzed with a two-way analysis of variance (ANOVA) that was corrected for multiple comparisons using the Holm −Sidak method.

3.4 Results

3.4.1 Synthesis of Nanoparticle Variants

We synthesized a 100-nm liposomal nanoparticle in a manner similar to our previously published work[15,19]. Using remote loading, the nanoparticle's cargo was measured to be 0.2 mg DOX per 1 mg of lipids. The stability of the drug encapsulation was confirmed by dialyzing the formulation against PBS at 37℃. The drug leakage was less than 5% of the total encapsulated drug after 24 h. Using dynamic light scattering, the size of the nanoparticles was uniform with an average diameter of ~105 nm (with a polydispersity index of 0.03).

To be detectable in the *in vivo* imaging studies, the nanoparticle was labeled with an NIR fluorophore using Vivotag-S 645 or 680 or 750 and the Alexa 647 or 750, which contained an NHS functional group[15]. The fluorophore was conjugated directly onto the lipid 1,2-Distearoyl-sn-glycero-3-phosphoethanolamine (DSPE). To ensure complete conjugation of DSPE with Vivotag, a 2-fold molar excess of fluorophore was used over DSPE. Once thin layer chromatography (TLC) confirmed that the reaction was complete, the unreacted fluorophore was removed by dialysis. DSPE-fluorophore was used as part of the lipid matrix at 2.5 mol%. The final levels of the fluorescent label on each liposome were directly measured using Fluorescence Molecular Tomography (FMT) or the Spectrum In Vivo Imaging System. Stable fluorescence labeling was confirmed by dialyzing the nanoparticle formulations for 24 h dialysis resulting in no change in fluorescence signal.

To fabricate the targeting variants of the nanoparticles, the $\alpha_V\beta_3$ integrin-targeting peptide *c (RGDfC)* and the EGFR-targeting peptide *CYHWYGYTPQNVI* were linked on the distal end of the PEG(2000)-NH_2 of the parent nanoparticles. The two DSPE-PEG-peptide conjugates were prepared according previously established methods[19]. We prepared three nanoparticle variants including the EGFR-targeting nanoparticle (EGFR-NP), the $\alpha_V\beta_3$ integrin-targeting nanoparticle (RGD-NP) and the dual-ligand nanoparticles (dual-ligand NP). The number of peptides on each nanoparticle variants was determined using direct protein assays (Bio-Rad Protein Assay using Coomassie Blue G-250 dyes), which showed that single-ligand nanoparticle contained ~2,000 peptides per particle whereas the dual-ligand variant had ~4,200 peptides per particle[19]. The zeta potential of the nanoparticles was measured to be slightly positive (~4 mV)[19].

3.4.2 Targeting Studies in the D2.A1 Model

To evaluate the targeting and therapeutic performance of the dual-ligand nanoparticle, we used a mouse model of metastatic TNBC. Specifically, we used the D2-Hyperplastic Alveolar Nodules (HAN) series, which consists of various clonally related cell lines derived from the same premalignant murine hyperplastic alveolar nodule[107]. We used the metastatic D2.A1 cells that extravasate and initiate metastatic outgrowth in the lungs of syngeneic immunocompetent Balb/c mice. This is a well characterized model that provides a reliable assay system to thoroughly evaluate nanoparticles in metastatic TNBC in animals with intact immune systems[94,95]. The D2.A1 cells stably expressed both fluorescent and bioluminescent reporter genes that allowed monitoring of the dissemination of metastatic disease in mice using *in vivo* imaging, *ex vivo* fluorescence imaging and histology. Mice were used in the targeting studies on day 15 after tail vein

injection of the D2.A1 cells. At that point, bioluminescence imaging (BLI) indicated that metastasis was present in the lungs with a signal of ~$3x10^7$ photons/sec. Immunohistochemical analysis showed that both EGFR and $\alpha_V\beta_3$ integrin are overexpressed in lung areas with metastatic D2.A1 cells (**Fig 3.6**).

First, we compared the two single-ligand targeting variants, EGFR- and RGD-targeted nanoparticles in their ability to direct the nanoparticles to early metastasis. A cocktail of the two single-ligand nanoparticles was systemically injected into the same animals (n = 5 mice). The cocktail contained an equal number of nanoparticles of EGFR-NP and RGD-NP labeled with the NIR fluorophores Vivotag 680 and 750, respectively. Fluorescence molecular tomography (FMT) was used to perform *in vivo* imaging. FMT uses four NIR fluorescence channels that facilitate quantitative and simultaneous imaging of four different NIR fluorophores in the same animal [14,42]. We have performed extensive studies that validate the quantitative accuracy of the results obtained from FMT imaging *in vivo*[14–17,53]. Each animal presented one or two metastatic sites in the lungs. **3.2**A shows an example of representative BLI and FMT images from the same mouse. **3.2**B summarizes the quantification of NIR fluorescence signal for the two single-ligand nanoparticle variants in each metastatic site. The data indicate that the two single-ligand formulations had different targeting performance varying from one metastatic site to the next. We should mention that the accumulation of non-targeted liposomal nanoparticles in metastasis was significantly lower than their EGFR- or RGD-targeting nanoparticle counterparts[19].

In another animal study, we sought to confirm the results from the *in vivo* imaging studies. To do so, we used the IVIS Spectrum system to image the lungs *ex vivo*. Our

previous work has showed that EGFR and $\alpha_V\beta_3$ integrin-targeting nanoparticles achieve maximum deposition in metastasis within 3 h after systemic administration[14–16,18,19]. A cocktail of EGFR-NP and RGD-NP labeled with different Alexa fluorophores (Alexa 647 and 750) was systemically injected (n = 4 mice). After 3h from nanoparticle injection, lungs were perfused, excised and precisely sliced in 500-μm sections using a mouse brain slicer. In previous studies, we confirmed that tissue sections with a thickness of 500 μm cause minor attenuation of signal from Alexa 647 and 750 fluorophores, which facilitated quantification of the concentration of the nanoparticle variants in lungs with metastasis. Representative images are shown in **Fig 3.2**B. It can be seen that the deposition of RGD-NP and EGFR-NP coincided with the locations of D2.A1 metastasis (green: GFP-expressing cells). Signal quantification shows a variable targeting performance from each nanoparticle variant. We then converted the fluorescence signal to percentile of the injected dose. Overall, 7.8% of the injected cocktail deposited at sites of metastasis with RGD-NP and EGFR-NP being 5.1 and 2.7% of the dose, respectively. In a previous study[19], the dual-ligand nanoparticle achieved an about two-fold higher deposition in metastasis than either single-ligand nanoparticle variant. To evaluate non-specific uptake of the nanoparticle by the lungs, the same cocktail of targeted nanoparticles was systemically injected in healthy animals resulting in negligible signals from the lungs.

3.4.3 Evaluation of Therapeutic Efficacy

To assess the therapeutic efficacy of a drug-loaded nanoparticle with the capability of simultaneously targeting EGFR and $\alpha_V\beta_3$ integrin, we fabricated a dual-ligand nanoparticle (dual-ligand NP), which contained an equal number of the EGFR and RGD-targeting peptides (total ~4,200 peptides per particle). Doxorubicin was the drug of choice

due to the long clinical history of liposomal doxorubicin. First, we evaluated the cytotoxicity of DOX against the D2.A1 cells. As shown in **Fig 3.3**A, DOX demonstrated significant cytotoxicity against D2.A1 cells with the 50% inhibitory concentration (IC50) being 0.3 μM. This indicates that DOX has a strong anticancer activity against D2.A1 cells.

Fig 3.3B shows the timeline and schedule of treatments (n = 6–8 mice per treatment). As an initial metric of responsiveness of metastatic disease to the treatments, quantification of BLI signal in the thoracic region was used. Animals were treated at days 3, 4 and 5 after tumor inoculation with standard free DOX, the standard non-targeted nanoparticle (NT-NP), the two single-ligand nanoparticle variants or the dual-NP at a dose of 7.5 mg of DOX per kg bw. At the beginning of treatment (day 3), the BLI signal from the lungs of the animals was ~$4x10^5$ photons/sec indicating the presence of metastasis. BLI imaging was performed every 3–4 days. As shown in **Fig 3.3**C, metastatic disease progressed rapidly in the case of the untreated group and animals had to be euthanized by day 25. Even though DOX is a highly potent cytotoxic agent, the group treated with standard DOX exhibited similar progression of the disease to the untreated group. Similarly, the NT-NP did not have any therapeutic effect on metastatic disease. On the contrary, metastatic outgrowth was delayed in the groups treated with either single-ligand nanoparticle variant with the EGFR-NP treatment being more effective. The BLI signal of the groups treated with RGD-NP and EGFR-NP reached the high value of 10^8 photons/sec by day 27 and 30 respectively. Most notably, the entire group treated with dual-NP displayed very low BLI signal until day 30, at which point aggressive metastatic disease recurred only in a subset of the animals.

In addition to BLI imaging, we compared the survival rates of the different treatment groups (**Fig 3.4**). The survival rate was in good agreement with BLI imaging. The treatments were generally well tolerated. The body weight change for representative groups is shown in **Fig 3.7**. While exact longitudinal measurements of the group treated with the dual-ligand NP were not recorded, the weight of these mice was similar to the single-ligand NP treatments with a less than 10% loss immediately after treatment. All the groups treated with DOX-loaded nanoparticles maintained their body weight without any dramatic weight loss at the time of treatment. The survival of the untreated and free DOX-treated group (2 mg/kg) was comparable indicating the standard form of the chemotherapeutic drug had negligible therapeutic benefits. In the case of free DOX, we used a low and a high dose (2 and 7.5 mg/kg DOX). Notably, treatment with the high dose of DOX (7.5 mg/kg) affected negatively the survival of the animals, which can be attributed to the high toxicity of the treatment itself. The survival rates of the two single-ligand nanoparticle treatments were also in good agreement with the BLI data. Both targeted nanoparticles prolonged survival compared to the free drug treatment with the EGFR-NP being more effective. While 100% of the mice in the other groups did not survive more than 43 days, about a third of the dual-ligand NP-treated group was still alive at 120 days.

3.4.4 Histological Characterization

We sought to histologically assess the deposition of RGD-NP and EGFR-NP in metastasis. We labeled EGFR-NP and RGD-NP nanoparticles with the Alexa 350 and 568 fluorophore respectively, which allowed both nanoparticles to be visualized in the same histological section using fluorescence microscopy. Mice bearing D2.A1 metastasis were injected with a cocktail containing an equal number of EGFR-NP and RGD-NP particles

was injected to mice bearing D2.A1 metastasis. After 3 h from the injection of the cocktail, the lungs were perfused, excised, and processed for histology. **Fig 3.5** shows representative images. Both EGFR-NP and RGD-NP were predominantly deposited in locations with dispersion of metastatic cancer cells by targeting the near-perivascular regions and remodeled endothelium of metastasis (**Fig 3.5**A). While both EGFR-NP and RGD-NP colocalized in regions with metastatic cancer cells, some metastatic regions were primarily targeted only by EGFR-NP (**Fig 3.5**B) or RGD-NP (**Fig 3.5**C). **Fig 3.5**D shows a quantification of multiple histological sections indicating that frequency of individual events for EGFR-NP and RGD-NP or their overlap.

3.5 Discussion

In this work, we explored the ability of multi-ligand targeting schemes to direct drug-loaded nanoparticles to breast cancer metastasis and its highly heterogeneous microenvironment. In previous studies[15,18,19], we employed and tested different combinations of peptides as ligands on nanoparticles that target EGFR, β_3 and β_1 integrins, P-selectin, and fibronectin. These different biomarkers represent different processes and stages of development of metastatic breast cancer[19,108] . The processes include the molecular mechanisms that underlie the interplay between epithelial-mesenchymal transition (EMT) and its counterpart mesenchymal-epithelial transition and the processes that enable metastatic outgrowth and proliferative programs[108,109]. By using various animal models of metastasis including 4T1, D2.A1, D2.OR and MDA-MB-231, those earlier studies showed that only multi-ligand nanoparticles were able to accurately target a broad spectrum of breast cancer metastasis either at dormancy or very early transient stages of aggressiveness[19]. Here, we selected two ligands that target $\alpha_V\beta_3$ integrin and EGFR that exhibit spatiotemporal variability representing different cancerous activities and stages of metastatic development. The adhesion and attachment of circulating tumor cells to the endothelium of distant metastasis is mediated by $\alpha_V\beta_3$ integrin present on both cancer and endothelial cells[23]. In addition to adhesion-specific markers, metastatic breast cancer cells carry a continuously varying overexpression of the cell-surface EGF receptor, which contributes to tumor invasiveness and metastasis[108,110]. The targeting data for the single-ligand variants indicated that RGD-NP and EGFR-NP resulted in deposition at metastatic sites of 5.1 and 2.7% of the injected dose, respectively. While $\alpha_V\beta_3$ integrin-targeting frequently led to higher nanoparticle deposition than EGFR-targeting, histological analysis

illustrated the significant spatial variability between the two targeting variants, suggesting that a single-ligand formulation is not capable of capturing each and every region with metastatic cancer cells. This indicates that EGFR-NP and RGD-NP exhibited complimentary targeting of metastatic sites and their various tumor microenvironments.

Nanoparticles are highly suitable to multi-ligand schemes due to their ability to accommodate a high number of ligands on their surfaces and enhanced multi-targeting avidity as a result of geometrically enhanced multivalent attachment on the targeted receptor. Importantly, multi-ligand targeting schemes are not restricted to one nanoparticle type and can be adapted by most nanoparticle systems. To showcase the application of multi-ligand targeting, we selected a liposomal nanoparticle, because it is an all-purpose, versatile drug carrier for numerous types of drug molecules with high potential for clinical translation. More specifically, we rethought the 100-nm PEGylated liposome with a size, composition and drug cargo similar to that used in the clinic for patients with metastatic breast cancer. In typical scenarios, adjuvant chemotherapy is given to high-risk patients even though often the disease has not become clinically apparent. Here, we sought to address this unmet clinical need for metastasis specific chemotherapy and improve treatment regimens by replacing a traditional nanoparticle antineoplastic agent with a safe, effective variant. The survival studies indicate that the dual-ligand liposome could identify clinically silent metastasis with a high degree of precision. It should be noted that the treatment started at an early time point of the metastatic progress, which represents the early stage of micrometastasis. Similar to the clinical experience, micrometastasis in its early and transient stages does not exhibit a fully developed mass and lacks angiogenic activity, which makes it inaccessible *via* passive accumulation through leaky vasculature.

Due to efficient vascular targeting, we suggest that a long-term therapy can be administered to asymptotic high-risk patients to effectively establish remission and ultimately cure. Further, when we administered the cytotoxic drug in its free form at the same dose as the dual-ligand nanoparticle (*i.e.*, 7.5 mg/kg), the treatment had adverse effects resulting in reduced survival, probably due to enhanced systemic toxicity.

This work shows that multi-ligand nanoparticles can successfully deliver drugs to the majority of metastatic sites and effectively treat this lethal disease. Overall, efficient and precise delivery of potent chemotherapy yielded significant improvement in event-free survival in mouse models of triple-negative breast cancer metastasis at a safe dose compared to typical clinical regimens.

3.6 Figures

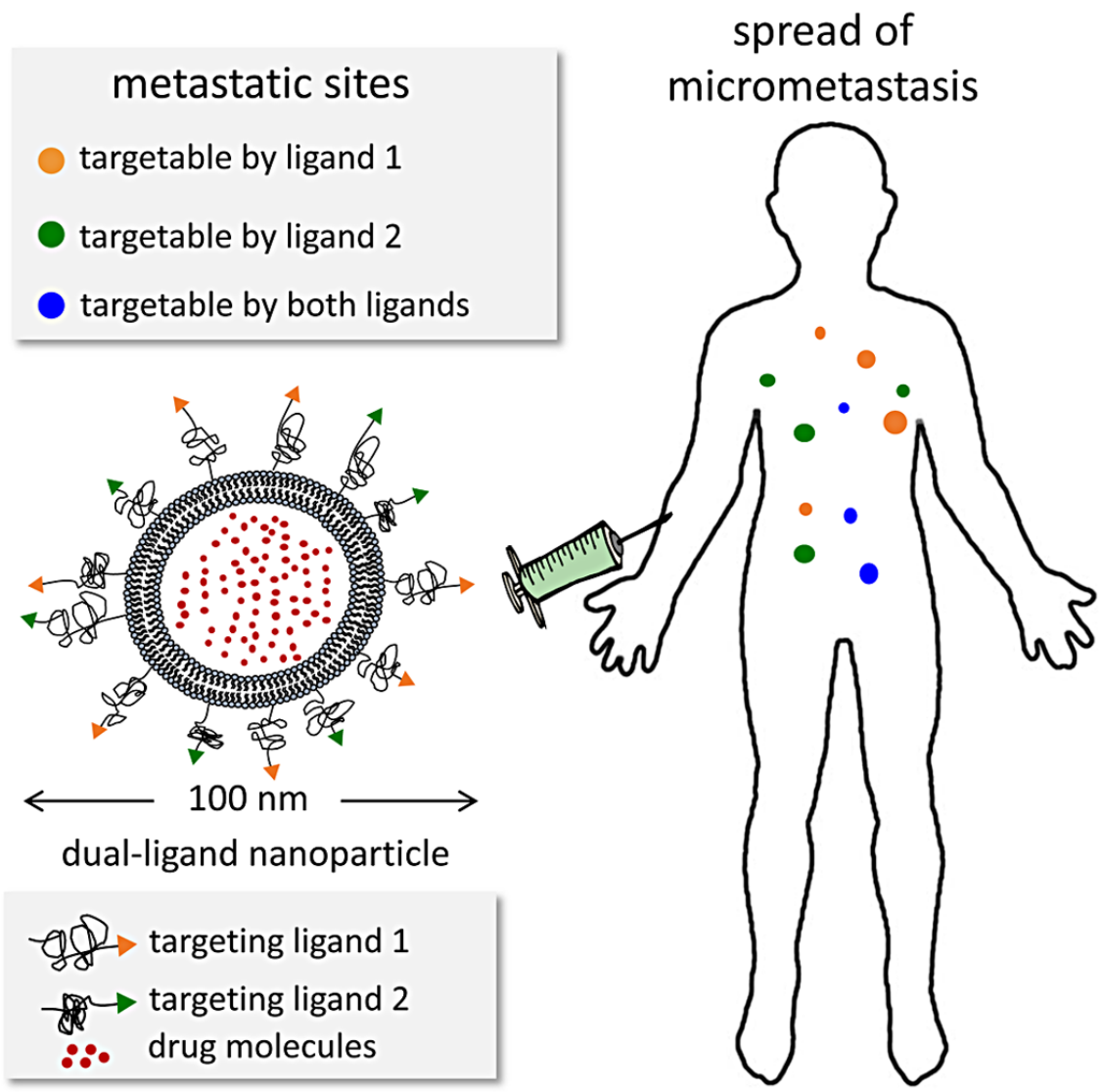

Figure 3.1 Illustration of the multi-targeting concept shows a dual-ligand nanoparticle targeting the dynamic nature of metastatic disease.

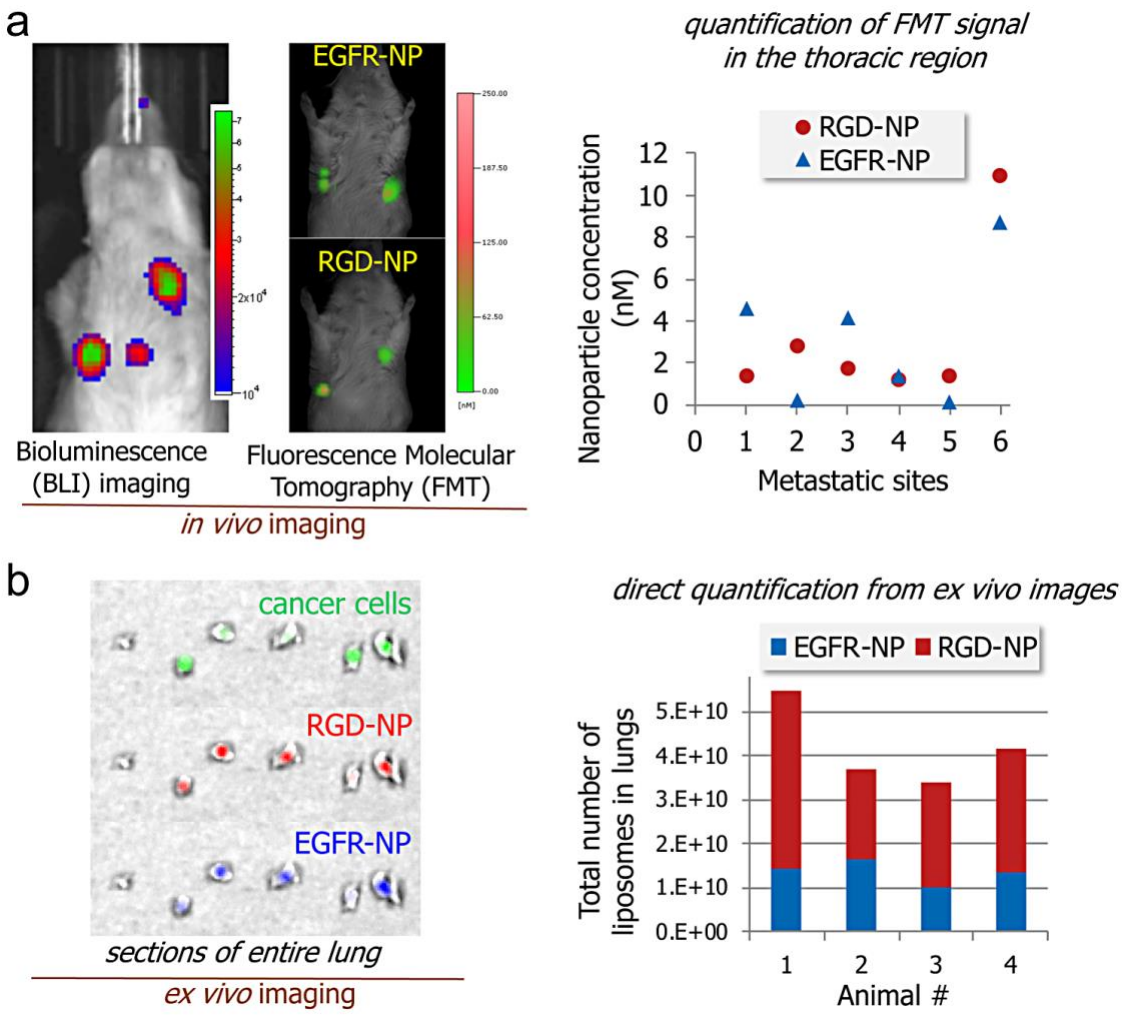

Figure 3.2 Targeting EGFR and αvβ3 integrin in the D2.A1 mouse model of metastasis.

(A) Bioluminescence imaging (BLI) shows the development of metastasis in the lungs (left). FMT in vivo imaging was performed 3 h after injection of a cocktail of EGFR-NP and RGD-NP. Using the different NIR fluorophores (Vivotag 680 and 750) on each nanoparticle variant, the fluorescence signal in each metastatic site of the FMT images was quantified for each formulation (n = 5 mice). On the basis of phantom measurements of each formulation using the FMT system, the fluorescence signal was converted to nanoparticle concentration. **(B)** In a different animal study, a cocktail of EGFR-NP and RGD-NP labeled with a different fluorophore (Alexa 647 and 750) was intravenously injected into animals with D2.A1 metastasis. After 3h from injection, lungs were perfused,

excised, sectioned into thin slices of equal thickness and imaged ex vivo using an IVIS Spectrum system. The signal from each lung slice was quantified and summarized for the entire lung indicating the total number of each nanoparticle variant in the lungs of different mice with metastasis (n = 4 mice).

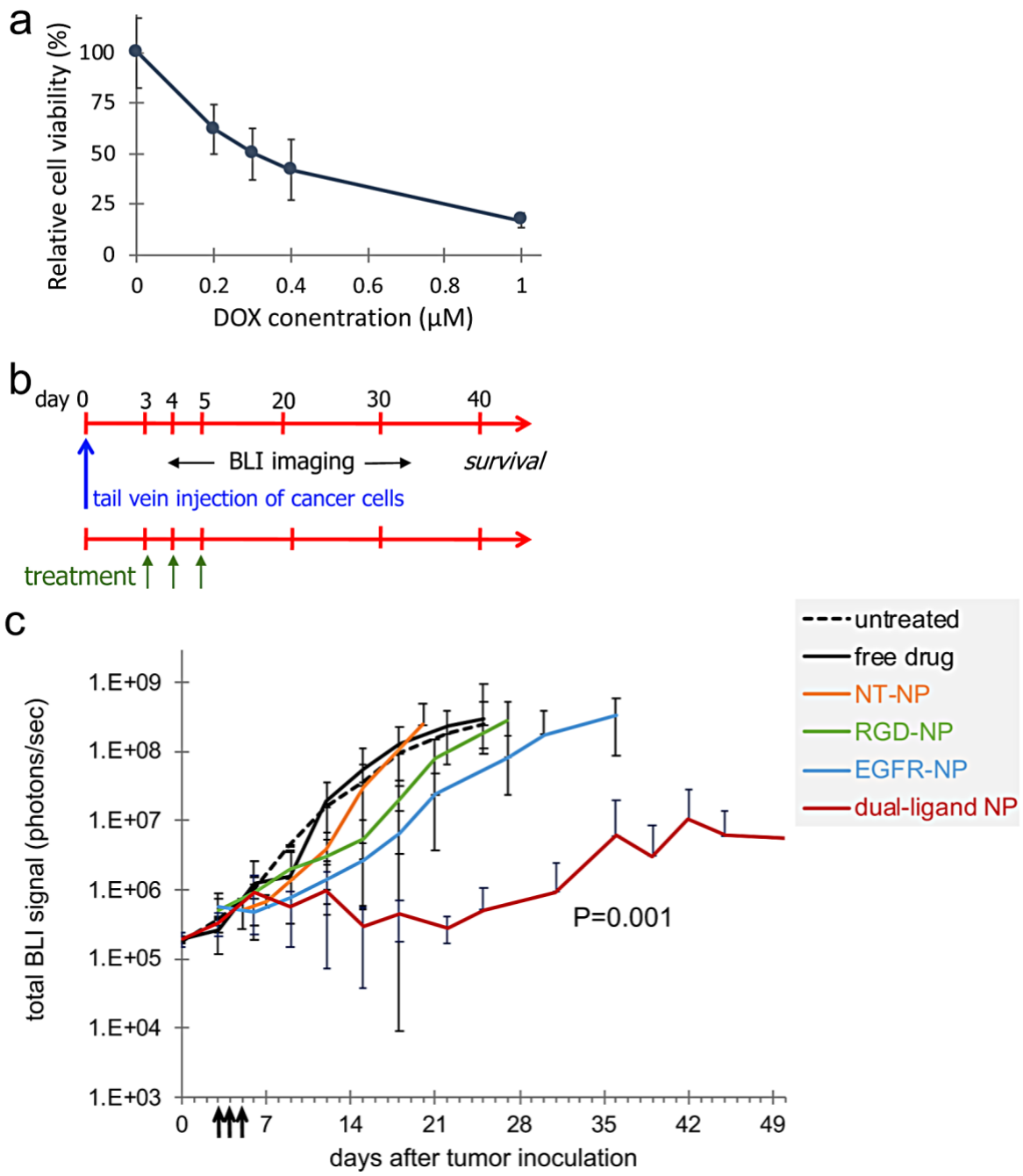

Figure 3.3 Treatment of mice with D2.A1 metastasis using dual-ligand nanoparticle loaded with doxorubicin.

(A) The cytotoxicity of doxorubicin (DOX) was evaluated on D2.A1 cells. Cytotoxicity studies were performed by seeding D2.A1 cells at a density of 5 x 10^3 cells per well. Cells were incubated with the treatment for 24 h at a concentration ranging between 0.2–1 µM

DOX. After treatment application, the cells were washed three times with fresh medium and then incubated for 48 h at 37℃. The number of viable cells was determined using a formazan-based cell counting assay (CCK-8). Untreated cells served as live controls for normalization of the data. Data points represent group mean ± s.d. **(B)** The timeline and schedule of treatments are shown with respect to tumor inoculation. **(C)** The response of cancer metastasis to treatment was monitored using longitudinal BLI imaging. Quantification of the BLI signal in the thoracic region is shown for mice with D2.A1 metastasis treated at days 3, 4 and 5. In addition to untreated animals, treatments included non-targeted NP (NT-NP), RGD-NP, EGFR-NP, dual-ligand NP, and free DOX (n = 6–8 mice per treatment). The y-axis is in logarithmic scale. All nanoparticle formulations were administered at 7.5 mg/kg DOX (two-way ANOVA with repeated measures).

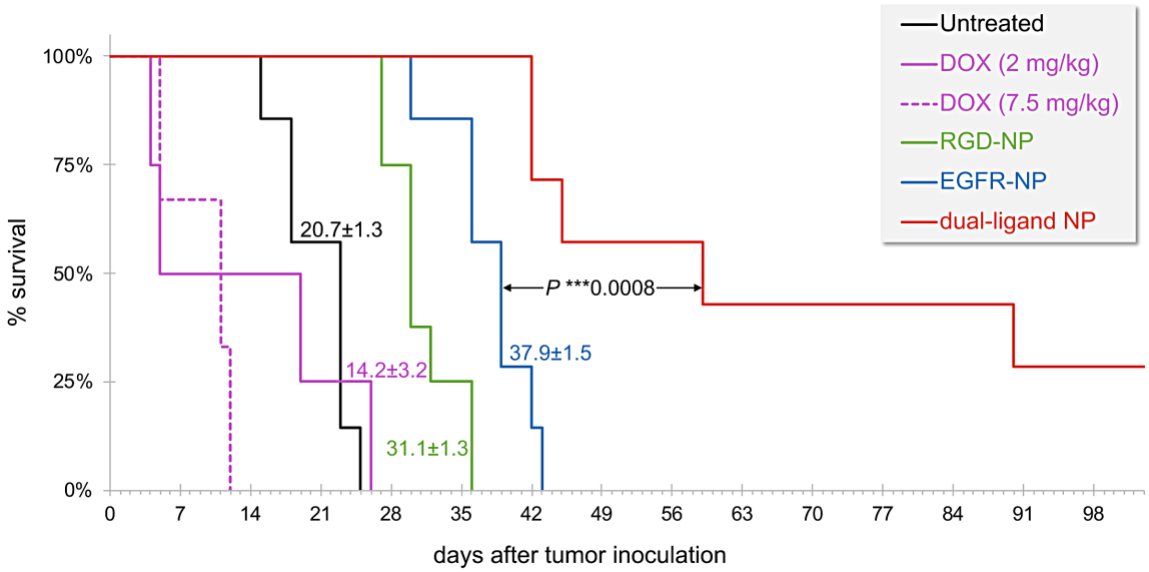

Figure 3.4 The survival time of metastasis-bearing mice treated with cytotoxic drugs was compared to untreated animals.

The animals were treated at days 3, 4 and 5. The dual-ligand nanoparticle formulation was administered at 7.5 mg/kg DOX. In addition to the nanoparticle formulation, treatments included free DOX injected at 7.5 or 2.5 mg/kg (n = 6–8 mice per treatment). The difference between the survival curves of the dual-ligand NP and EGFR-NP-treated groups was assessed by the log-rank (Mantel-Cox) test.

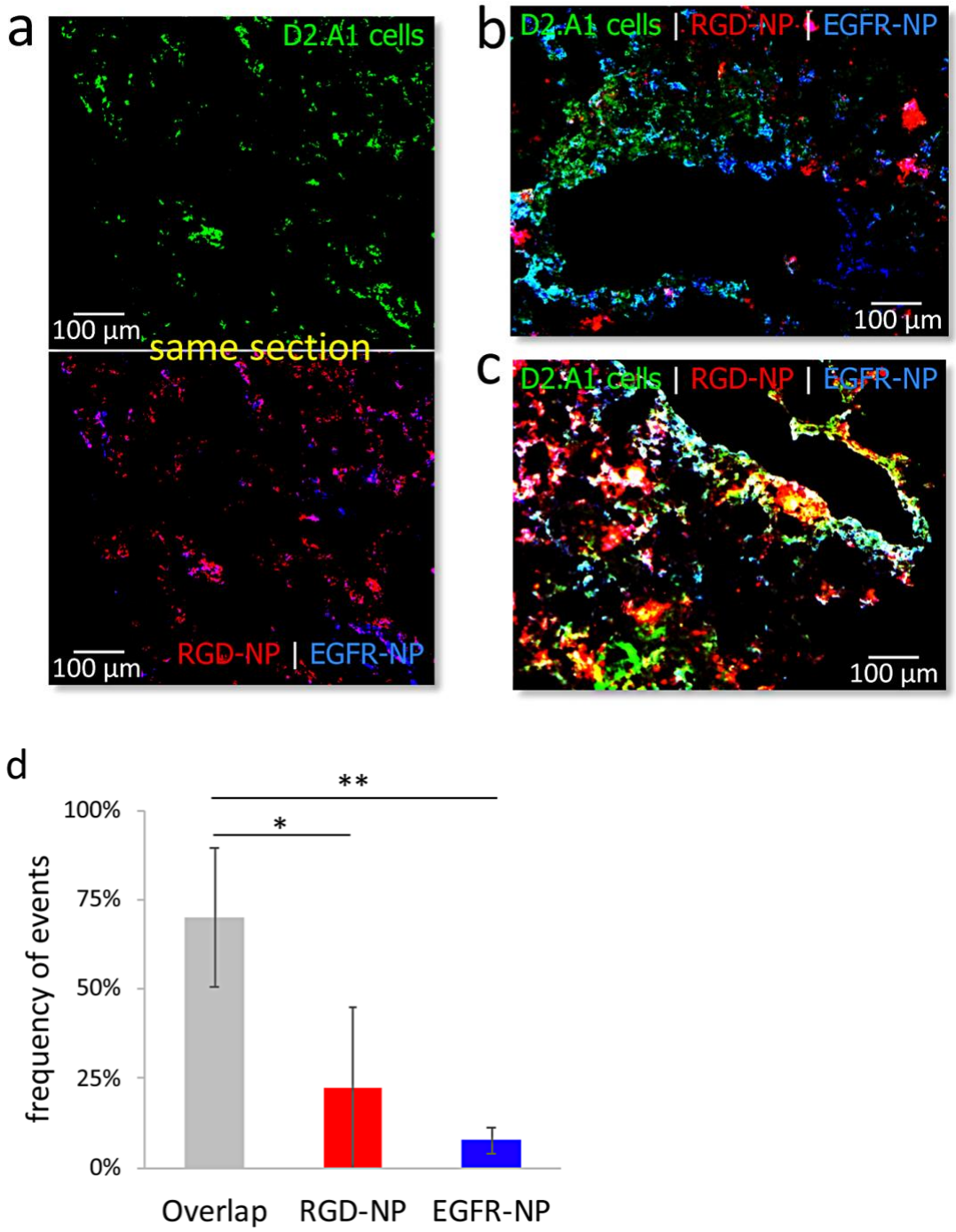

Figure 3.5 Histological evaluation of the microdistribution of RGD-NP and EGFR-NP nanoparticles in metastasis in the lungs of mice.

(A) Representative fluorescence image of lung tissue shows dispersion D2.A1 metastatic cancer cells (top; 20X magnification). After 3 h from injection of a cocktail containing

Alexa 350-labeled EGFR-NP and Alexa 568-labeled RGD-NP, the two targeting variants colocalized in locations with metastatic cancer cells (bottom). Different regions with metastatic cancer cells were predominantly targeted by **(B)** EGFR-NP or **(C)** RGD-NP (green: D2.A1 cancer cells; red: RGD-NP; blue: EGFR-NP). **(D)** A pixel-by-pixel quantification indicates individual events for EGFR and RGD-NP or their overlap (n = 3, grouped analysis ANOVA; correct for multiple comparisons using the Holm−Sidak method. *P* values: $^{*}0.024$, $^{**}0.002$).

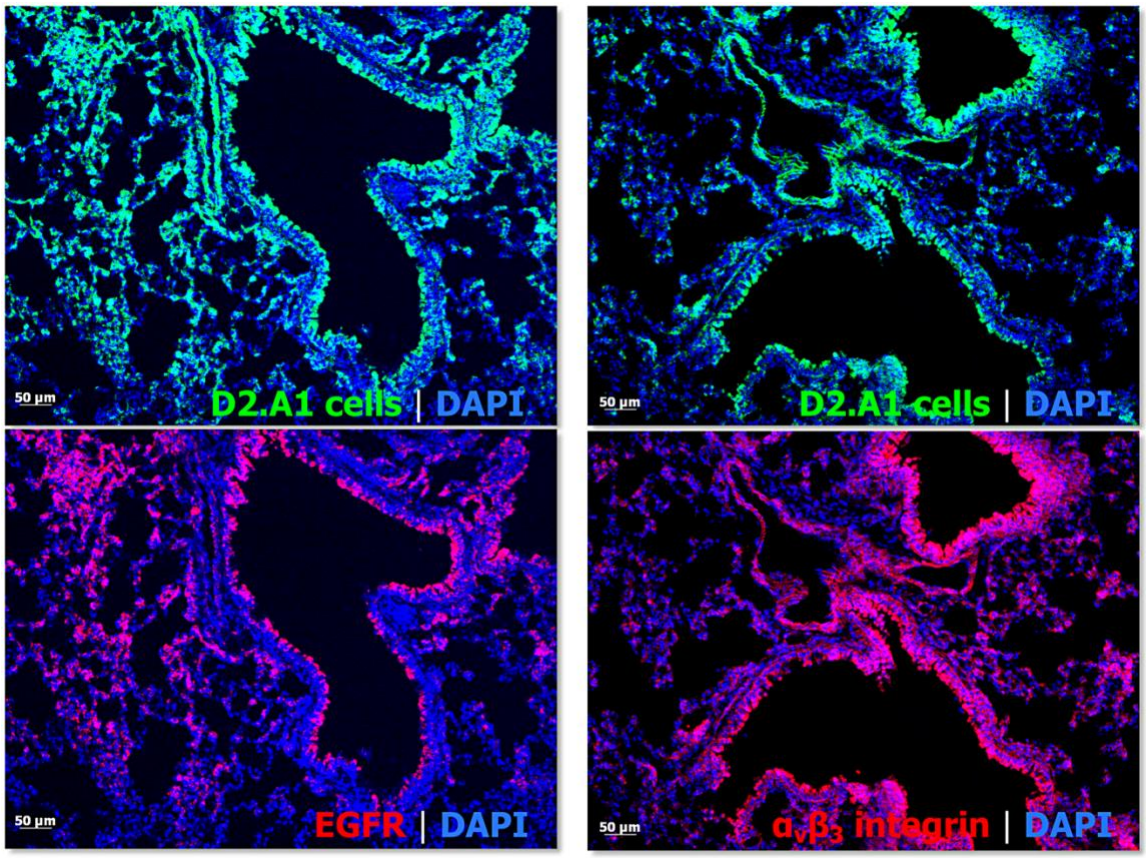

Figure 3.6 Availability of Targeting Moieties.

Immunohistochemistry was performed to evaluate the expression of $\alpha_V\beta_3$ integrin and EGFR in D2.A1 metastasis in the lungs. Serial tissue sections were stained with the nuclear stain DAPI and the specific antibody for $\alpha_V\beta_3$ integrin or EGFR.

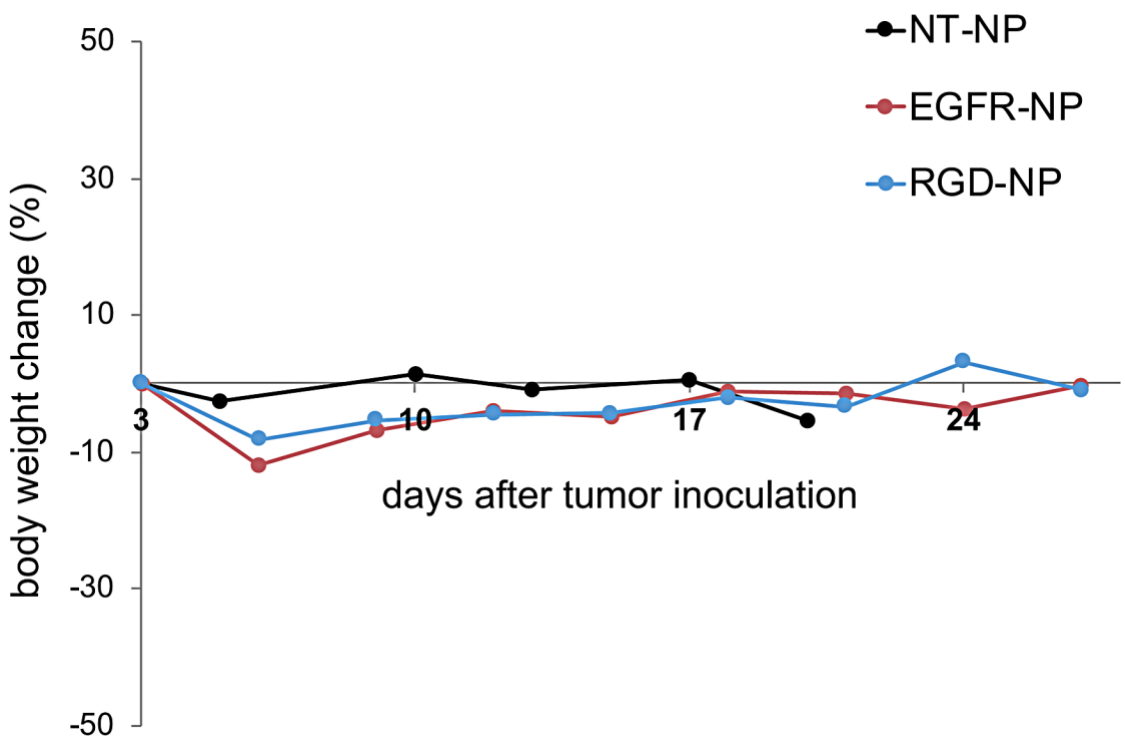

Figure 3.7 Body weight progression.

The average % change of body weight of mice bearing D2. A1 metastasis is shown after treatment with DOX-loaded nanoparticles (n = 6–8 mice per group), including the non-targeted NP (NT-NP), EGFR-targeted NP (EGFR-NP) and $\alpha_V\beta_3$ integrin-targeted NP (RGD-NP).

Chapter 4: Immune Agonist Delivery to Metastatic Triple Negative Breast Cancer via Site Specific Nanoparticle Targeting

Note: This chapter will be submitted for publication as:
Comparison of the uptake of untargeted and targeted immunostimulatory nanoparticles by immune cells in the microenvironment of metastatic breast cancer

Gil Covarrubias, Georgia Loutrianakis*, Haley M. Sims*, Mayura P. Umapathy, Morgan Lorkowski, Peter A. Bielecki, Taylor J. Moon, Michelle L. Wiese, Prabhani U. Atukorale, Efstathios Karathanasis

*These authors contributed equally

4.1 Abstract

Cancer immunotherapy elicits immune-recognition and T cell-mediated killing of tumor cells, thus is a powerful approach for treating metastatic breast cancer. However, one major hurdle is to overcome the profound immunosuppression within the tumor microenvironment (TME), which is associated with the accumulation of dysfunctional antigen-presenting cells (APCs). To alter the immunosuppressive TME, we developed an immunostimulatory nanoparticle (NP) to reprogram these inhibitory APCs into properly activated APCs that stimulate tumor-reactive cytotoxic T cells. Importantly, systemic delivery allows NPs to efficiently utilize the entire microvasculature and gain access into the majority of the perivascular TME, which coincides with the APC-rich tumor areas leading to uptake of the NPs predominantly by APC cells. In this work, the 60-nm NP was loaded with a STING agonist, which triggers a robust production of interferon β, resulting in activation of APCs. In addition to untargeted NPs, we employed 'mainstream' ligands targeting fibronectin, $\alpha_v\beta_3$ integrin and P-selectin that have been commonly used to direct nanoparticles to tumors. Using the 4T1 mouse model, we assessed the microdistribution of the four NP variants in the tumor immune microenvironment in three different breast cancer landscapes, including primary tumor, early metastasis and late metastasis. The different NP variants resulted in variable uptake by immune cell subsets depending on the organ and stage of the metastatic TME. Among the NP variants, therapeutic studies indicated that the untargeted NPs and the integrin-targeting NPs exhibited remarkable short and long-term immune response and long-lasting antitumor capacity.

4.2 Introduction

The majority of breast cancer-associated deaths occur due to drug-resistant relapse and metastatic disease[1,45,46]. Accordingly, breast cancer recurrence is often associated with aggressive and chemoresistant phenotypes. As a result, today's treatments are often ineffective against aggressive breast tumors. On the other hand, cancer immunotherapy is based on the premise of immune-recognition and targeted killing of tumor cells, which possess the promising potential of targeting treatment resistance and metastatic disease[111]. The presence of pro-inflammatory innate immunity within the tumor microenvironment (TME) that contains functional antigen-presenting cells (APCs), such as dendritic cells (DCs) and macrophages, is a critical determinant of the success of an immunotherapy. Notably, a significant portion of cancer patients have had suboptimal responses to immunotherapies. This stems from the fact that effective antitumor immunity strongly depends on overcoming the profound immunosuppression within the TME.[44,112–114] Breast cancer cells are responsible for inducing immunosuppressive cues effectively yielding tumor promoting and/or defunctionalized innate and adaptive immune cells.[11,12] As a result, the TME is enriched with depolarized tumor promoting M2 macrophages, myeloid derived suppressor cells (MDSCs) and T-regulatory cells amongst other 'bad' immune cells. Consequentially, a non-inflamed and unreceptive TME significantly inhibits systemic lymphocytes from effectively trafficking into tumors, thereby shielding tumors from systemic immuno-surveillance.[11,12]

Conventional approaches attempt to trigger systemic immunity by delivering an adjuvant and tumor-associated antigens to tumor-draining lymph nodes but fail to tackle

the issue of metastatic disease. Recent efforts have explored systemic delivery of immunostimulatory nanoparticles (NPs) that directly target, reprogram and activate the dysfunctional immune cells and local APCs in the TME. This research has facilitated an antitumor immune response leading to tumor clearance and prevention of disease relapse.[13,50,115] Systemic administration allows NPs to drain into the APC-rich perivascular niche of tumors, which leads to predominant uptake of NPs by the desirable subset of cells (**Fig 4.1**A).[13] Further, systemic delivery is the most effective approach to access micrometastasis. Importantly, such an approach enables activated tumor-resident APCs to directly process temporally present tumor-associated antigens shed from cancer cells. While nanoparticle-based delivery systems have typically focused on delivery of drugs to cancer cells, NPs are uniquely suited to reach APCs within the perivascular TME due to their ability to preferentially accumulate in these regions.

To further explore nanoparticle deposition and their respective uptake within tumor associated lymphocytes, we investigate the use of nanoparticle targeting using variant targeting ligands. This approach allowed us to detail the immunostimulatory NPs microdistribution (*i.e.* APC uptake) in the near-perivascular space of primary tumor and metastatic TMEs. We used a 60-nm NP loaded with cyclic diguanylate monophosphate (cdGMP),[116] an agonist of the stimulator of interferon genes (STING) pathway (**Fig 4.1**B). The STING agonist is a cyclic dinucleotide (CDN) that binds the STING machinery to trigger a robust production of Type I interferons leading to activation and expansion of APCs.[48,49,116–118] We compared three targeting NP variants and a non-targeted NP by measuring their uptake by different immune cell subsets in tumors (**Fig 4.1**C). As ligands,

we selected three different peptides targeting fibronectin, P-selectin or $\alpha_v\beta_3$ integrin. While these ligands have been widely employed for targeting nanoparticles to tumors,[15,16,18–20,119] they are also suitable for targeting immune cells in the near-perivascular TME and tumor's remodeled endothelium. Specifically, perivascular overexpression of fibronectin in the extracellular matrix plays a critical role in the migration of cancer cells. [21,27,30,31] Both non-targeted and fibronectin-targeting NPs preferentially deposit in the extracellular matrix of the TME and remain available for uptake by APCs. On the other hand, STING activation of tumor endothelial cells has shown to generate strong antitumor response.[51,52] This makes P-selectin an interesting target due to its overexpression by endothelial cells in the remodeled tumor vasculature.[75–80] Finally, while the role of integrins in angiogenesis, cancer progression and metastasis is well known,[23] several integrins, including $\alpha_v\beta_3$, are expressed by dendritic cells and macrophages for mediate binding and phagocytosis.[120–122] We assessed the uptake of the four immunostimulatory NP variants by immune cells in three different breast cancer landscapes, including primary tumor, early metastasis and late metastasis. We used the 4T1 model, as this is one of the standard models to study both solid and metastatic breast cancer in immunocompetent mice. We then characterized the cellular mechanisms of antitumor immune responses to the immunostimulatory NPs and the corresponding long-term therapeutic outcomes.

4.3 Methods and Materials

4.3.1 Nanoparticle Synthesis and Characterization

Nanoparticles were developed by drying lipid films consisting of 48.5 mol% DOPC (1,2-dioleoyl-sn-glycero-3-phosphocholine, Avanti), 48.5 mol% DPPC (1,2-dipalmitoyl-sn-glycero-3-phosphocholine, Avanti), 3 mol% mPEG2000-DSPE (1,2-distearoyl-sn-glycero-3-phosphoethanolamine-N-[methoxy-(polyethylene glycol)-2000], Laysan Bio). Lipid films were hydrated using PBS at 60 ºC for 30 minutes and vortexed every 5-10 minutes. The nanoparticles were sized to 50-60 nm via ultra-sonication while under ice using a pulse sequence consisting of 10-second 20% power output intervals followed by a 20-second off cycle for a total of 5 minutes. Resultant nanoparticles were dialyzed for 2hrs using a 50 kDA MWCO dialysis membrane against PBS and subsequently stored at 4 ºC. Liposomal nanoparticles charge and size was ascertained using zeta potential and dynamic light scattering (DLS) measurements, respectively. For fluorescently labelled nanoparticles a 0.5 mol% DiR (DiIC18(7) (1,1'-Dioctadecyl-3,3,3',3'-Tetramethylindotricarbocyanine Iodide)) dye was added during the lipid drying process by equally reducing the molar percentage of DOPC and DPPC. For treatment and immune cell recruitment studies, the dry lipid films were hydrated in PBS containing 200 μg cyclic di-GMP (InvivoGen). Encapsulated cyclic di-GMP was measured via absorbance readings taken from a high-performance liquid chromatography (Shimadzu) assay. Drug retention studies were performed over a 24 h time course at 25 ºC.

Functionalization of nanoparticles with vascular targeting ligands was achieved through a sulfo-SMCC crosslinker. For these studies, the 3 mol% mPEG2000-DSPE was replaced with 3 mol% DSPE-PEG2000 Amine (1,2-distearoyl-*sn*-glycero-3-

phosphoethanolamine-N-[amino(polyethylene glycol)-2000], Laysan Bio). As described previously, lipids films were developed, hydrated and ensuing nanoparticles were sized via ultra-sonication. Here the targeting ligands of interest were $\alpha_v\beta_3$ integrins, P-selectins, and fibrin-based proteins using their targeting moieties; c(RGDfC), CDAEWVDVS, and CREKA, respectively. Using sulfo-SMCC chemistry, we chemically linked the amine functionalized nanoparticles to the thiol groups of the previously indicated peptides. Available amine functional groups on the nanoparticle were linked to sulfo-SMCC and then the desired peptide in a 1:2:3 molar ratio, respectively, and allowed to react for 2.5 hrs. The molar ratio was consistent across all the peptide to secure similar peptide densities across the formulations. The nanoparticle-peptide constructs were dialyzed for 2hrs using a 50 kDA MWCO dialysis membrane against PBS. To validate that the peptide density was similar, the number of peptides on each nanoparticle variant was measured using a Bio-Rad Protein Assay. Furthermore, particles were again subjected to DLS and zeta potential measurements to further guarantee consistency across nanoparticle batches. For treatment and immune cell recruitment studies, the resultant nanoparticle-peptide constructs were lyophilized until they were completely desiccated. The desiccated lipids were then re-hydrate in PBS containing 200 μg cyclic di-GMP (InvivoGen) followed by subsequent formulation steps. Cyclic di-GMP was incorporated after the nanoparticle-peptide conjugation and cleaning to prevent the exposed amine groups on cyclic di-GMP from participate in the functionalization reaction.

4.3.2 Institutional Animal Care and Use Committee Statement

All animal procedures were conducted under a protocol approved by the Institutional Animal Care and Use Committee of Case Western Reserve University.

Animal well-being took priority over the studies conducted when it came to decisions regarding euthanasia or other interventions.

4.3.3 Tumor Model

The 4T1 model was established in BALB/c mice (Jackson Laboratories). 4T1 cells were stably transfected with a lentivirus to express cytosolic firefly luciferase and green fluorescent protein (GFP). 4T1 cells were cultured in RPMI medium (Gibco, Gaithersburg, MD) containing 10% fetal bovine serum (FBS) and 1% penicillin-streptomycin. Cells were routinely tested for mycoplasma contamination to ensure cell line health and stability. Briefly, 4T1 inoculations were performed while mice were under a surgical anesthesia of 2-3% isoflurane inhalant. The no. 9 inguinal mammary fat pad was surgically exposed and an inoculant containing $5x10^5$ 4T1 cells/50 μL was injected. Tumors were closely monitored with bioluminescent imaging (BLI) and caliper measurements to track lesion progression. For tumor removals, mice were similarly anesthetized under a surgical plane. Solid tumors were surgically exposed and removed on either day 10 or 14 as described by the study. Meloxicam and bupivacaine were administered pre- and post-surgery, respectively. Complete surgical resection was verified using bioluminescent imaging the day after tumor removal. In the case where mice were re-challenged, an inoculant containing $1x10^5$ 4T1 cells/50 μL was subcutaneously injected into the right flank. Tumor-bearing mice were intravenously treated with nanoparticles as indicated by the respective study. Cyclic di-GMP (InvivoGen) was administered at a 10 μg dosage. Anti-PD1 was subcutaneously administered adjacent to the solid tumor mass at a dosage of 250 μg (BioXCell).

4.3.4 Bioluminescent Imaging

Bioluminescent imaging (BLI) was performed using an IVIS Spectrum Imaging System (Perkin Elmer, Waltham, MA). Imaging took place 10 minutes after a 200 μL solution of D-luciferin (12.5 mg/mL) was interperitoneally administered. BLI imaging was conducted every 2-5 days until the terminal point of the study. At the terminal point, if required by the study, lungs, liver, spleen and tumors were collected for either immunohistochemistry or flow cytometry analysis.

4.3.5 Flow Cytometry

Anti-mouse antibodies including, CD45 (30-F11), CD11c (HL3), F4/80 (T45-2342), CD11b (M1/70), Ly6G (1A8), Ly6C (AL-21), CD49b (DX5), CD3e (145-2C11), CD8a (53-6.7) and CD4 (GK1.5), were purchased from BD Biosciences and Biolegend with a dye-conjugate for flow cytometry. Flow cytometry analysis was performed 24hrs after a fluorescently labeled-nanoparticle or the last treatment was administered. Blood was collected via retro-orbital bleeding. Mice were subsequently euthanized and the tumor, liver, lungs and spleen were removed. Tumors and lungs were digested for 1hr in 1mg/mL collagenase in serum free RPMI medium (Sigma Aldrich/Thermo Fischer Scientific). Organs were gently homogenized and passed through a 70 μm filter to obtain a single cell suspension. Lungs, liver and blood single cell suspensions were washed with ACK lysis buffer (Gibco). Resultant. single cell suspensions were blocked with anti-mouse CD16/CD32 (2.4G2; BD Biosciences) and stained with the dye-conjugate antibodies and then counterstained with DAPI (BD Biosciences). Fluorescently tagged samples were read on a BD LSR II flow cytometer. Flowjo software was used to analyze and quantify immune cells with the respective markers.

4.3.6 Histological Staining and Microscopy

Immunohistochemistry was conducted to identify the tumor burden in visceral organs and the topological distribution of the targeted nanoparticles within tumor associated microenvironments. Briefly, 4T1 bearing-mice were intravenously injected with fluorescently labeled nanoparticles 24 hrs prior to organ resection. Mice were anesthetized with a 5% isoflurane inhalant and transcardially perfused with heparinized PBS followed by a 4% paraformaldehyde solution in PBS. The solid mammary tumor, lungs and liver were harvested and placed in 4% paraformaldehyde for 24hrs and then dried in a 30% sucrose (w/v) in PBS solution for 48hrs. Resulting tissues were embedded and frozen in optimum cutting temperature (Thermo Fisher Scientific). Frozen tissue blocks were sliced into 10 μm sections and mounted on gold plated tissue slides. Resultant tissues were counterstained with a DAPI mounting medium (Vector Laboratories). Tissue sections were imaged at 10x and 20x magnification using either a Zeiss Axio Observer Z1 inverted fluorescent microscope or a Leica TCS SP8 gated STED confocal microscope. Larger montages were collected using the automatic tiling via the Mosaic acquisition feature with the associated software.

4.3.7 Statistical Analysis

All statistical analysis was executed using Prism 7 (GraphPad Software). The data depicted was analyzed using a one- or two-way ANOVA with either a *post hoc* Tukey or Sidak's test; the statistical analysis used is described in each figure legend. Statistical significance is determined by a P-value less than 0.05. Unless mentioned, all values are reported as mean ± SE.

4.4 Results

4.4.1 Characterization of Tumor Model

The 4T1 murine model is a standard model to study metastatic breast cancer in immunocompetent mice. The 4T1 murine model was orthotopically inoculated into the no.9 inguinal mammary fat pad; and as time progressed, it developed spontaneous metastasis in visceral organs including the lungs and liver reminiscent of those observed in human patients.[15,20,123] The 4T1 cells were transfected with a lentivirus to stably express cytosolic firefly luciferase and GFP for *in vivo* and *ex vivo* cell tracking. After the primary tumor was established, it was surgically removed, so that metastatic foci remained intact and metastatic disease could be studied at early or later stages. Representative BLI images (**Fig 4.2**A) and quantification of BLI signal from the primary site (**Fig 4.2**B) and thoracic region (**Fig 4.2**C) indicate the progression of disease. Using flow cytometry, the 4T1 cancer cells and $CD45^+$ leukocytes were quantified in the primary tumor and lungs 10 days after tumor inoculation. First, it is important to highlight that the immune cells were the dominant cell subpopulation in the primary tumor site with the leukocyte to tumor cell ratio being about 3:1 (**Fig 4.2**D). Second, the early spread of the disease was observed in both liver and lungs (**Fig 4.2**E,F). To establish the late stage metastatic setting, the primary tumor was surgically resected on day 14. Analysis on day 23 indicated that metastatic disease progressed rapidly with the content of tumor cells doubling in the liver and lungs between days 10 and 23. Representative histological images show the difference of metastatic spread in the liver and lungs between days 10 and 23 (**Fig 4.2**G).

4.4.2 Uptake of Nanoparticle Targeting Variants by APCs in Different Tumor Microenvironments

To study the microdistribution and cell uptake of nanoparticle variants with different targeting ligands, we developed a 60-nm nanoparticle comprised of a lipid matrix containing DPPC, DOPC, and DSPE-PEG-ligand. DiR was added to the lipid matrix as a fluorescent reporter for flow cytometry analysis (**Fig 4.3**A). Nanoparticle variants included fibronectin-targeting nanoparticles (CREKA-NP), $\alpha_v\beta_3$ integrin-targeting nanoparticles (cRGD-NP), P-selectin-targeting nanoparticles (PSN-NP) and untargeted nanoparticles (mPEG-NP) (**Fig 4.3**B). We employed commonly used peptides including the $\alpha_v\beta_3$ integrin-targeting c(RGDfC),[14–16,19,20] the P-selectin-targeting CDAEWVDVS,[15,18,19] and the fibronectin-targeting CREKA. [15,18,19] Sulfo-SMCC chemistry was used to conjugate the peptides on the distal end of PEG-amines on the nanoparticle's surface; the respective ligand density was determined to be approximately 2,000 peptides per particle across all formulations (Bio-Rad Protein Assay). [13,77] All nanoparticle formulations had similar size and zeta potential (**Fig 4.3**C,D).

As shown in Figure 3A, we examined the uptake of nanoparticles in the primary tumor, early metastasis and late metastasis. The nanoparticle variants were intravenously injected at an equal dose ($1x10^{13}$ nanoparticles per mouse) and organs were analyzed by flow cytometry 24 h after injection. Histological analysis showed that NPs deposited throughout the primary tumor (**Fig 4.7**A). Most notably, the deposition of NPs in lungs and liver was significant in regions of metastasis compared to minimal accumulation in the healthy portions of these organs (**Fig 4.7**B,C). Considering that the four NP variants had no cargo, the tumor masses after surgical resection was similar for all 4 groups (**Fig 4.8**A).

In the primary tumor, the vast majority of NPs for all the targeting variants were taken up by $CD45^+$ leukocytes ranging from 3- to 11-fold higher than cancer cells (**Fig 4.3**E). Notably, the highest uptake by $CD45^+$ leukocytes was observed for the untargeted NP variant. Specifically, for APCs, the untargeted NP exhibited the highest uptake by both DCs and macrophages (**Fig 4.3**F). In the case of the scenario of early stage metastasis, integrin-targeting NPs had the highest uptake by lung DCs and macrophages as well as liver macrophages (**Fig 4.3**G,H). Similar to lungs and liver, the integrin-targeting NPs had the highest uptake by APCs in the blood and the spleen (**Fig 4.8**B,C). In the case of the scenario of late stage metastasis, the untargeted NP was the best overall performed in terms of uptake by APCs in lungs and liver (**Fig 4.3**I,J), which is consistent with a more advanced TME with a leaky endothelium. All the formulations exhibited similar levels of uptake by APCs in blood and spleen at the late metastasis stage (**Fig 4.8**D,E). In the late stage setting, P-selecting-targeting NPs were significantly taken up by endothelial cells which coincides with expectations (**Fig 4.8**F,G).

4.4.3 Evaluation of Cellular Response to Immunostimulatory NP Treatment

Based on the findings of the cell uptake studies, we selected to evaluate the antitumor immune response of the untargeted NP and integrin-targeting NP being the overall best performers in primary tumors and early metastasis, respectively. For these studies, the nanoparticles were loaded with cdGMP, a small cyclic nucleotide (CDN) that is a STING agonist. The two formulation, indicated as cRGD-CDN-NP and mPEG-CDN-NP, exhibited stable and similar loading of the agonist at about 115 μg/mL cdGMP (**Fig 4.9**A). Mice bearing mammary 4T1 tumors were treated on day 8 with a single dose of untargeted NP or integrin-targeting NP at a dose of 10 μg of cdGMP per mouse (**Fig 4.4**A).

On day 10, organs were resected and analyzed for immune cell content to evaluate the cellular response to the immunostimulatory NP treatment 48 h after intravenous administration. Specifically, we focused on the primary tumor and organs prone to metastasis, such as lungs and liver. BLI indicated the immunostimulatory NP treatments produced a decrease of the tumor burden in both the primary tumor site and the thoracic cavity when compared to an untreated control (**Fig 4.4**B,D). Further, there was a significant decrease in the primary tumor volume for both treatment groups (**Fig 4.4**E). It should be noted that the mass of the tumor mass was reduced by one third in the case of the untargeted NP (**Fig 4.9**B). In the primary tumor, the untargeted NPs produced a significantly higher increase of DCs and natural killer (NK) cells than the integrin-targeting NPs (**Fig 4.4**F). Similarly, untargeted NPs had superior results in the lungs achieving significant elevation of DCs, macrophages and NK cells (**Fig 4.4**G). Considering the early-stage metastasis on day 10, the integrin-targeting NPs outperformed the untargeted NPs in the liver (**Fig 4.4**H). Further, the integrin-targeting NPs caused a significant increase of NK cells in the blood (**Fig 4.9**C), whereas elevation of macrophages was observed in the spleen in the case of untargeted NPs (**Fig 4.9**C). Besides innate immune cells, $CD4^+$ T cells were significantly elevated in primary tumor and lungs for both NP treatments (**Fig 4.9**E,F) and blood for only integrin-targeting NPs (**Fig 4.9**H)**.** Due to the short time scale of the study, no significant changes in $CD8^+$ T cells were observed in any organ 48 after the immunostimulatory NP treatments (**Fig 4.9E-I)**.

4.4.4 Long-term Therapeutic Efficacy

The long-term therapeutic efficacy of the untargeted and integrin-targeting immunostimulatory NPs was evaluated in a neoadjuvant scenario. The treatment scheme

involved untargeted or integrin-targeting immunostimulatory NP, surgical resection of primary tumor and the checkpoint inhibitor anti-PD-1. Prior to surgical resection on day 8, mice were treated with two consecutive doses of immunostimulatory NPs on day 6 and 7 (**Fig 4.5**A). After surgical resection, two consecutive doses of immunostimulatory NPs was administered in combination with anti-PD1 on day 12 and 13. The treatment conditions included the following groups: 1) untreated, 2) anti-PD1, 3) untargeted NP (before surgery-1x) + anti-PD1, 4) untargeted NP (before and after surgery-2x) + anti-PD1, and 5) integrin-targeting NP (before and after surgery-2x) + anti-PD1. Representative BLI images show the positive long-term outcomes of the immuno-stimulatory NP treatments (**Fig 4.5**B). Peripheral $CD8^+$ T cells in the blood provides a measure to evaluate activation of APCs in the TME and subsequent priming of effector T cells. In particular, the untargeted NP treatments in combination with anti-PD1 resulted in significant elevation of $CD8^+$ T cells in the blood (**Fig 4.5**C). The treatment scheme consisting of untargeted NP treatments before and after surgery outperformed all treatment schemes producing a remarkable increase of $CD8^+$ T cells in the blood on day 21. Increases were also observed for macrophages, NK cells and $CD4^+$ T cells in the blood mostly for the treatment schemes involving the untargeted NP (**Fig 4.10**A-D). Based on caliper measurements of tumor recurrence in the abdominal area, only the treatment schemes that included the untargeted NP treatments, either only before or before and after surgery, produced a complete response with no measurable tumor in the abdominal area (**Fig 4.5**D). While 100% of the untreated group and the anti-PD1-treated group did not survive, the treatment scheme that included untargeted NP before and after surgery showed the highest survival with more than 85% of this group showing no sign of the disease 2 months after the initial tumor inoculation

(**Fig 4.5**E). The survival data are in good agreement with the BLI signal from the lungs and abdominal region indicating that no metastatic disease was observed in the majority of the two groups that their treatment scheme included untargeted NP (**Fig 4.5**F,G). These mice from these two groups with BLI signal below the background baseline were considered good responders and were included in subsequent studies assess antitumor immunologic memory. The good responders from the two groups that received untargeted NP (n=4 for each group) were subjected to a tumor rechallenge by the inoculation of $1x10^5$ 4T1 cancer cells in the flank of the animals, a fifth of the original inoculant cell count. Both groups exhibited a significant increase in survival and decrease in tumor burden when compared to a naïve control group (**Fig 4.6**A,B). However, the group that was treated with untargeted NP before and after surgery outperformed the group that received the NP treatment only before surgery.

4.5 Discussion

Metastatic breast cancer is often incurable with mortality being associated to drug-resistant relapse and metastatic spread in visceral organs.[1,45,46] Even worse, about 30% of breast cancer patients diagnosed with early-stage, noninvasive disease will progress to metastatic disease, which severely limits treatment options. While short-term response to first-line therapies is achievable and patients appear to be disease-free and within stable remission, most patients succumb to metastatic recurrence due to a small population of disseminated tumor cells that is spread in secondary essential organs (*e.g.*, lungs, liver, bone, and brain).[2,3] Recurrent cancers acquire pro-survival and chemoresistant phenotypes, which results in today's treatments being ineffective against metastatic breast cancer. On the other hand, cancer immunotherapy holds an inherent ability to effectively treat the aggressive and metastatic forms of breast cancer. Current immunotherapy efforts have primarily focused on modulating the adaptive immune system (*e.g.*, killer T cells), which reacts slowly but provides long-lasting protection. However, the immunosuppressive "cold" TME of metastatic breast cancer inhibits activated systemic lymphocytes from effectively trafficking to tumor sites, thereby shielding developing tumors from systemic immuno-surveillance.[11,12] Alternatively, the rapid-onset of innate immune system can provide a powerful alternative and effectively bridge with the adaptive arm of the immune system. In this work, we designed immunostimulatory nanoparticles that specifically target and activate the dysfunctional and immunosuppressive APCs in the TME and reprogram them into T cell-stimulatory cells.

The immunostimulatory NP incorporates a cargo of a highly potent immune-potentiating molecule and systemic delivery targeting the APC-rich perivascular regions

of breast cancer. Systemic administration has significant advantages, because it allows immunostimulatory NPs to efficiently use the entire microvasculature, and readily seek and drain into the majority of the perivascular regions of breast cancer, which coincides with the APC-rich tumor areas. We show that this led to predominant uptake of immunostimulatory NPs by the desirable subset of immune cells in primary tumors. Also, we have shown in several previous studies show that systemic delivery of NPs is the ideal route to efficiently access micrometastasis.[14–20,39,53,53] Here, we establish that blood-circulating NPs were able to seamlessly access APCs in early and late sites of metastasis. In addition to 'standard' untargeted immunostimulatory NPs, we employed targeting ligands that have been commonly used with nanoparticles. In previous studies,[94,95,108,109,124–132] we exploited various targeting ligands to direct nanoparticles to metastatic breast cancers.

While these are 'mainstream' targeting ligands that have widely been used in a conventional manner to delivery anticancer drugs to cancer cells, we show that these ligands can further increase the uptake of NPs by immune cells in different landscapes of the TME. Considering the unique features and dynamic nature of the TME, the different variants of the targeted immunostimulatory NPs resulted in variable uptake by immune cell subsets depending on the location and stage of the TME (*e.g.*, primary tumor, early or late metastasis in liver or lungs). Future work can expand on testing more specialized targeting ligands for improved binding and enhanced uptake of immunostimulatory NPs by APCs including chemokine receptors CCR2, mannose, and ICAM-1.[133–137] By targeting these tumor-associated biomarkers correlated with APC transmigration or trafficking, we may be able to specifically localized nanoparticle carriers to these innate immune cell subsets.

In these studies, we observed the uptake of nanoparticles by APCs *via* passive and active targeting within different TMEs. Nanoparticles are designed to naturally drain and accumulate into the perivascular niche of TMEs due to the irregular growth of tumor-associated angiogenic blood vessels. Untargeted or mPEG-nanoparticles are the main beneficiary of the natural drainage that occurs in a well-developed TME due to their relatively high circulation time. This effect was directly observed when characterizing leukocytic uptake, and specifically its profound accumulation in dendritic cells and macrophages, in a solid primary tumor microenvironment. Integrin or cRGD-targeted nanoparticles displayed significant APC accumulation in sites of early metastasis. Upon evaluating the cellular response to the immunostimulatory nanoparticles, innate immune cell recruitment detailed a slightly different story. As expected mPEG-CDN-NPs induced increases in DC, macrophage and natural killer cells within the primary tumor, however this formulation also showed extensive recruitment in the lungs where, based on the uptake studies, integrin-targeting should have outperformed the untargeted formulation. A potential explanation may be that the cancer cell content and antigen payload within the solid tumor microenvironment is significantly greater than that available to APCs at metastatic sites. The reactivation and subsequent migration of innate immune cell within the solid tumor can potentially explain why APC recruitment was greater for the untargeted immuno-nanoparticle not only in the tumor but also within the lungs. Integrin-targeting however outperformed the untargeted formulation in the liver. This can be corroborated by ACP uptake and the near 3-fold deposition within activated endothelial cells which have also shown to have STING machinery.[52] The broad recruitment by the untreated

formulation, tumor and lungs, further exemplifies their outstanding survival and slowed rechallenge tumor outgrowth.

Harnessing the innate immune system using immunostimulatory NPs has the potential to dramatically improve tumor response to existing immunotherapies, such as immune checkpoint inhibitors (CPIs), which can bring transformative treatments for high-risk breast cancer patients. For example, clinical results show that immune checkpoint inhibitors achieve tumor control or regression in only 10-40% of patients,[9] even in the case of immunogenic tumors, which highlights the importance of the innate immune system and the local tumor immune microenvironment. By activating innate immunity within the TME, the immunity cycle can be restored allowing for the necessary communication between innate and adaptive immune cells. In this work, we modeled neoadjuvant therapy using the immunostimulatory NPs in combination with the anti-PD1 checkpoint inhibitor by surgically removing the primary tumor. STING and IFNβ-dependent antitumor immunity has shown to trigger production of immune checkpoint proteins (PD-1, IDO, CTLA-4) that cause immune resistance.[10,47,115] This made the combination of the immunostimulatory NPs with anti-PD1 highly synergistic resulting in amplification of T cell response and ultimately cure of 90% of mice. Our studies indicate that the untargeted immunostimulatory NP was sufficient to produce remarkable therapeutic outcomes in a neoadjuvant setting. In the future, we will explore whether targeted immunostimulatory NP are more effective in a purely metastatic setting.

4.6 Conclusion

In conclusion, we evaluated the ability of 'mainstream' targeting schemes to direct immunostimulatory NPs into the tumor immune microenvironment of metastatic breast cancer. We identified that the untargeted NP had the highest uptake by APCs in the primary tumor and late-stage metastasis, whereas the integrin-targeting NP variant was superior in sites of early metastasis. Using a STING agonist as the nanoparticle's cargo, successful trafficking of NPs in the perivascular TME resulted in activation and expansion of APCs in sites of primary tumor as well as early and late metastasis. Notably, the highest increase of immune cell infiltration was observed for the untargeted NPs as their uptake by APCs in the primary tumor was approximately 2-to-3 fold higher than that of the targeting NP variants. Considering the significant expansion of APCs and the tumor-associated antigens in the TME, long-term studies showed continuously increasing peripheral $CD8^+$ T cells. In combination with anti-PD1 treatment to boost the activity of $CD8^+$ T cells, the majority of the treated group was cancer-free and exhibited long-lasting antitumor capacity.

4.7 Figures

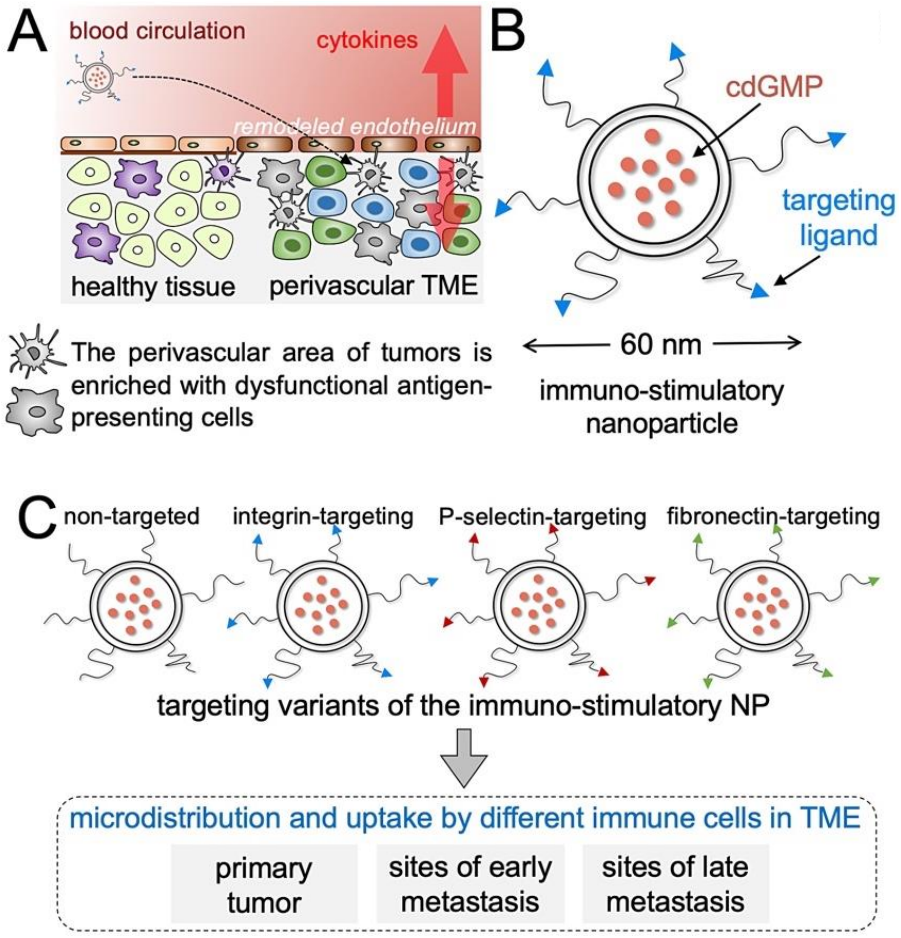

Figure 4.1 Illustration of targeting schemes for the delivery of immunostimulatory nanoparticles to tumors

(A) Systemic administration allows immunostimulatory nanoparticles to reach antigen-presenting cells in the near-perivascular area in sites of a primary tumor and metastasis. **(B)** Illustration of the 60-nm immunostimulatory nanoparticles loaded with a STING agonist (cdGMP). The distal ends of PEG coating can be used to link targeting ligands. **(C)** Schematic representation shows different immuno-stimulatory nanoparticle variants including untargeted, integrin-targeting, P-selectin-targeting and fibronectin-targeting. The microdistribution and uptake of the nanoparticle variants by different immune cell subsets

is evaluated in three different breast cancer landscapes including primary tumor, early metastasis and late metastasis.

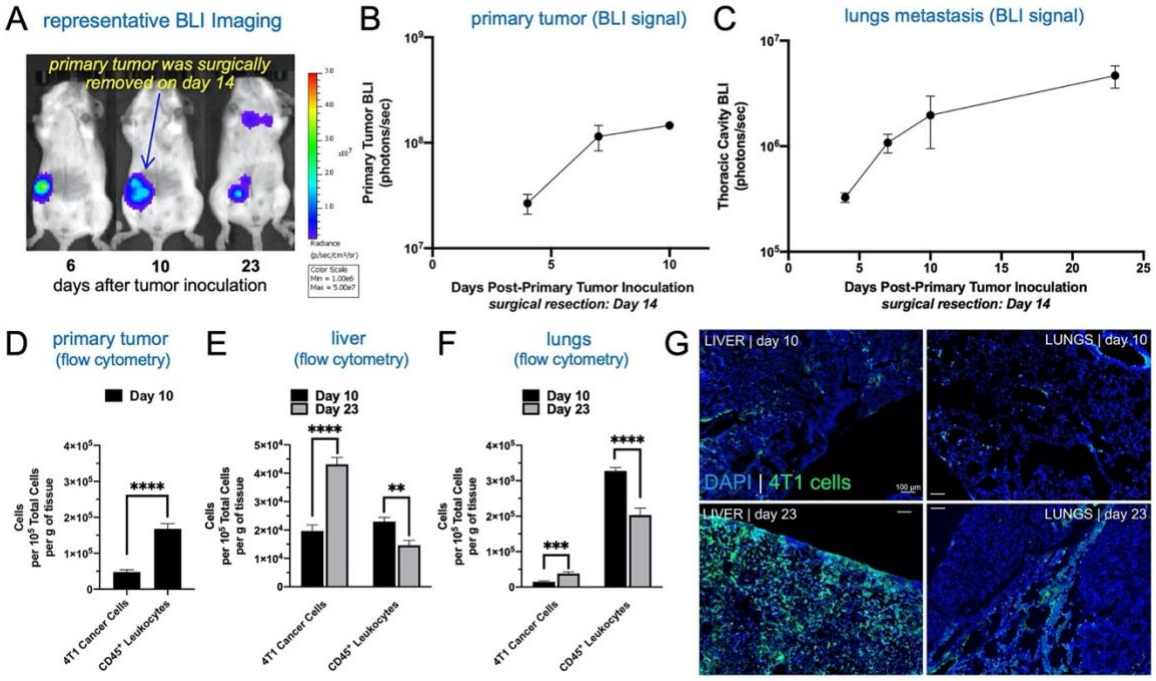

Figure 4.2 Characterization of mouse tumor model using bioluminescence imaging, flow cytometry and histology.

(A) Representative BLI images show an orthotopic 4T1 tumor in mice and its progression overtime. After surgical resection of the primary tumor 14 days after inoculation, metastatic outgrowth and recurrence is observed in the thoracic and abdominal regions. Quantification of the BLI signal from (B) the primary tumor and (C) thoracic region is shown., respectively (n=5). The 4T1 cancer cells (GFP reporter) and $CD45^+$ leukocytes were quantified using flow cytometry in the (D) primary tumor, (E) liver and (F) lungs. (G) Histological evaluation depicts the progression of metastatic disease in the liver and lungs (20x magnification; scale bar = 100 μm; blue: nuclear stain; green:4T1 cancer cells). Mean ± SEM are plotted with statistics by one-/two-way ANOVA with a *post hoc* Tukey or Sidak's test. **P<0.01; ***P<0.001; ****P<0.0001.

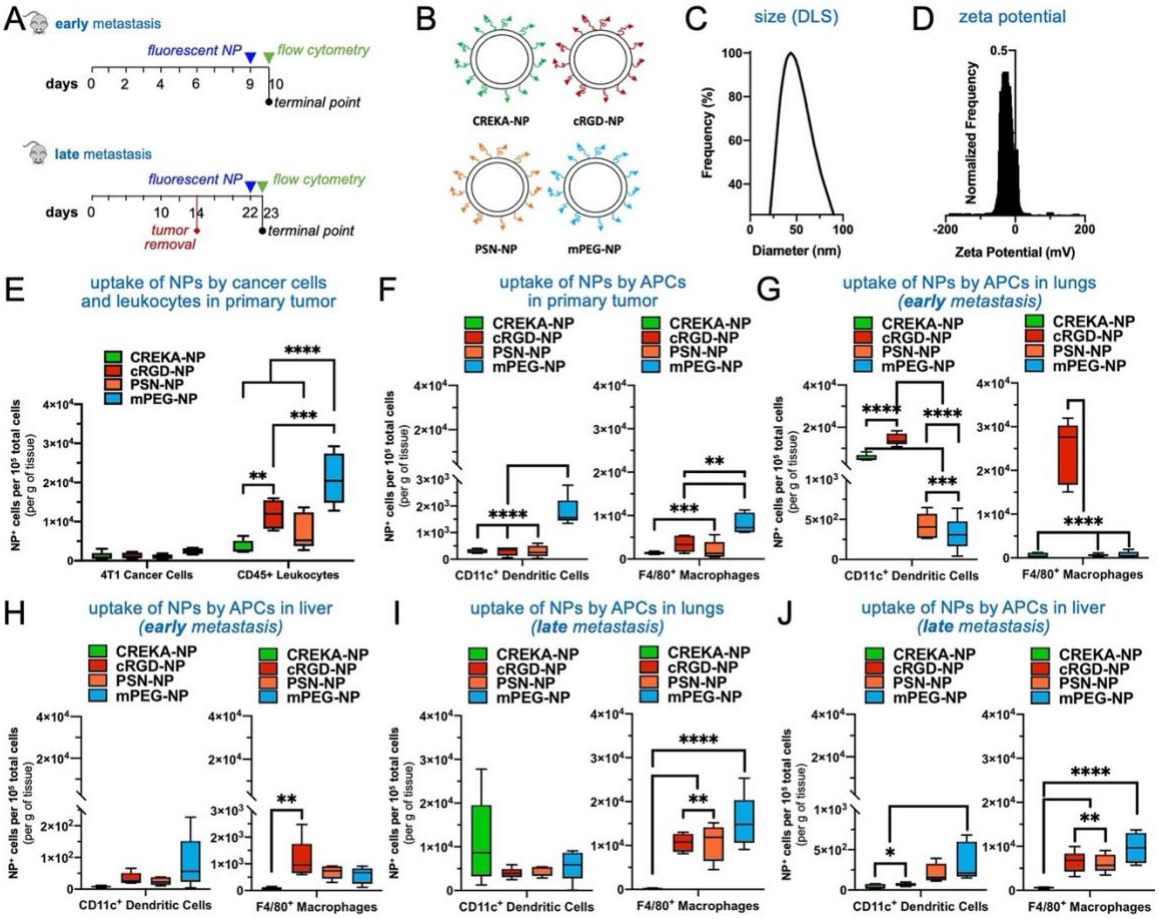

Figure 4.3 Quantification of nanoparticle uptake by APCs across different TMEs.

(A) Timelines show animal modeling, nanoparticle administration and flow cytometry analysis. **(B)** Schematic shows the different nanoparticle variants and their respective targeting moieties. **(C)** DLS measurement of nanoparticle size. **(D)** Zeta potential of nanoparticles. **(E)** Flow cytometry analysis of nanoparticle uptake by 4T1 cancer cells and $CD45^+$ leukocytes in primary tumor. Flow cytometry analysis of nanoparticle uptake by $CD11c^+$ dendritic cells and $F4/80^+$ macrophages in **(F)** primary tumor, **(G)** lungs at a stage of early metastasis, **(H)** liver at a stage of early metastasis, **(I)** lungs at a stage of late metastasis, and **(J)** liver at a stage of late metastasis (n=5 mice per group). Box and whisker plots (5-95 percentile) with statistics by one-/two-way ANOVA with a *post hoc* Tukey or Sidak's test**. ***P<0.05; **P<0.01; ***P<0.001; ****P<0.0001.

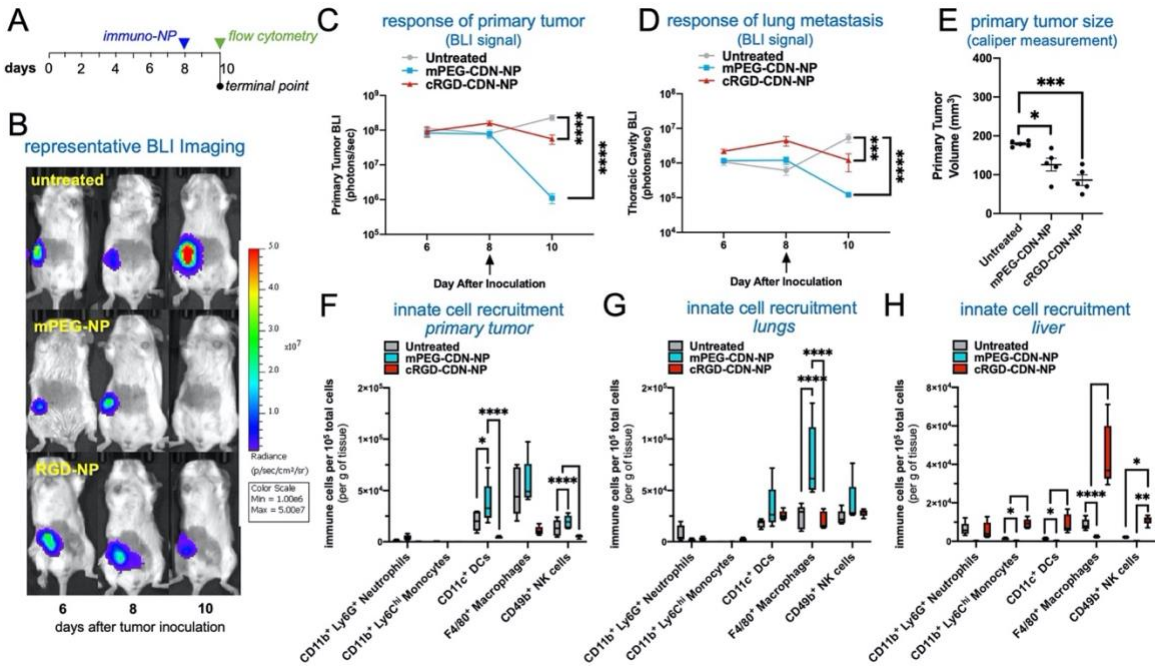

Figure 4.4 Mechanistic study of the cellular immune response to immunostimulatory NPs 48 h after systemic delivery.

(A) Timeline shows the treatment regimen. The untargeted or $\alpha_v\beta_3$ integrin-targeting immunostimulatory NP variants were loaded with the STING agonist cdGMP. Flow cytometry analysis was performed 48 h after intravenous administration of the formulations at 10 μg cdGMP per mouse. **(B)** Representative BLI images show the progression of the disease. Quantification of the BLI signal is shown for **(C)** the primary tumor and **(D)** lungs. Black arrow indicated the treatment day. **(E)** Primary tumor volume was obtained using caliper measurements at the terminal point on day 10. Flow cytometry analysis of innate immune cell recruitment to the **(F)** primary tumor, **(G)** lungs, and **(H)** liver 48 h after administration of formulations. N=5 mice per condition. Box and whisker plots (5-95 percentile) both with statistics by one-/two-way ANOVA with a *post hoc* Tukey or Sidak's test**. ***P<0.05; **P<0.01; ***P<0.001; ****P<0.0001.

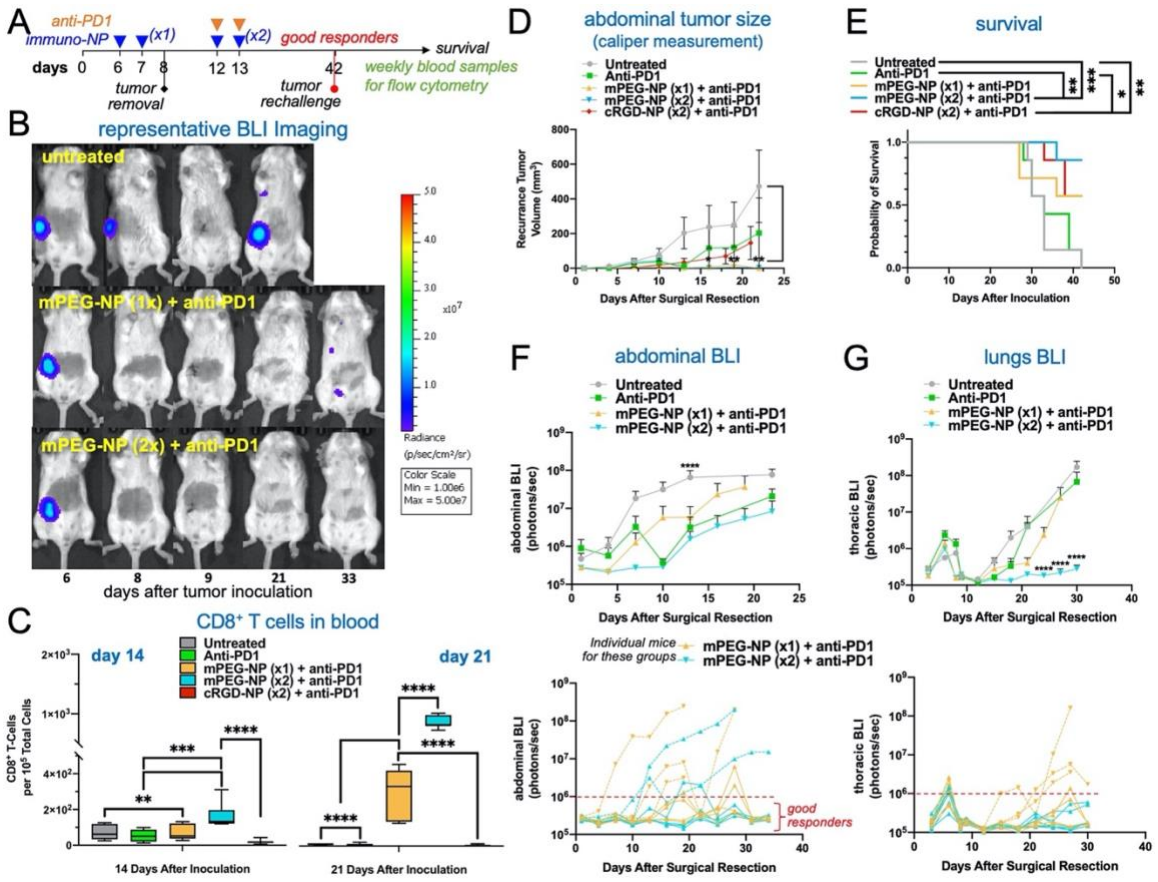

Figure 4.5 Long-term efficacy of immunostimulatory NPs in combination with surgery and anti-PD1.

(A) Timeline shows animal modeling, treatment schedule and related analysis. The immunostimulatory NP treatment included the untargeted NP or the integrin-targeting NP. The immunostimulatory NPs were administered on day 6 and 7 at a dose of 10 μg of cdGMP per mouse, followed by surgical resection on day 8. Some groups received a second immunostimulatory NPs (10 μg of cdGMP per mouse) on day 12 and 13 coupled with a subcutaneous administration of anti-PD1 (250 μg). **(B)** Representative BLI images show the progression of disease for some conditions. **(C)** The $CD8^+$ T-cells in the blood was measured on day 14 and 21 using flow cytometry. **(D)** Caliper measurement of tumor recurrence was performed in the abdominal area. **(E)** Kaplan-Meier survival analysis.

Quantification of BLI signal is shown for the **(F)** abdominal and **(G)** thoracic regions (top panels). The two groups that contained the untargeted NP treatment were further stratified into good and poor responders using the background BLI level (10^6 photons/second) as a threshold. N=7 mice per condition. Mean ± SEM are plotted with statistics by one-/two-way ANOVA with a *post hoc* Tukey or Sidak's test**. ***P<0.05; **P<0.01; ***P<0.001; ****P<0.0001.

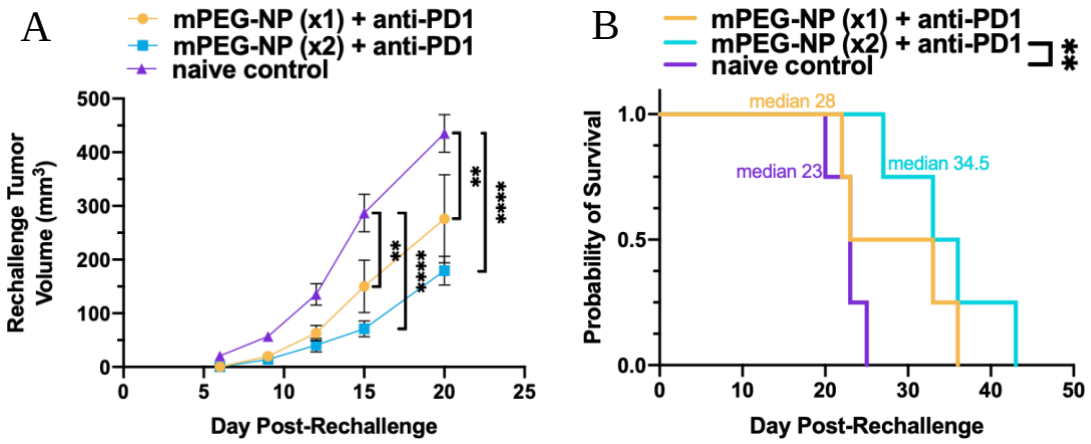

Figure 4.6 Response of good responders to a tumor rechallenge.

The treatment scheme of animals bearing 4T1 tumors included surgical resection of the primary tumor, anti-PD1 and untargeted immunostimulatory NP before and after surgery, indicated as mPEG-NP(x2), or only before surgery indicated as mPEG-NP(x1). The good responders from the two groups were rechallenged 42 days after the initial inoculation with $1x10^5$ 4T1 cells on their right flank. **(A)** Caliper measurement of the flank tumor size. **(B)** Kaplan-Meier survival analysis. N=4 mice per condition. Box and whisker plots (5-95 percentile) both with statistics by one-/two-way ANOVA with a *post hoc* Tukey or Sidak's test. **P<0.01, ****P<0.0001.

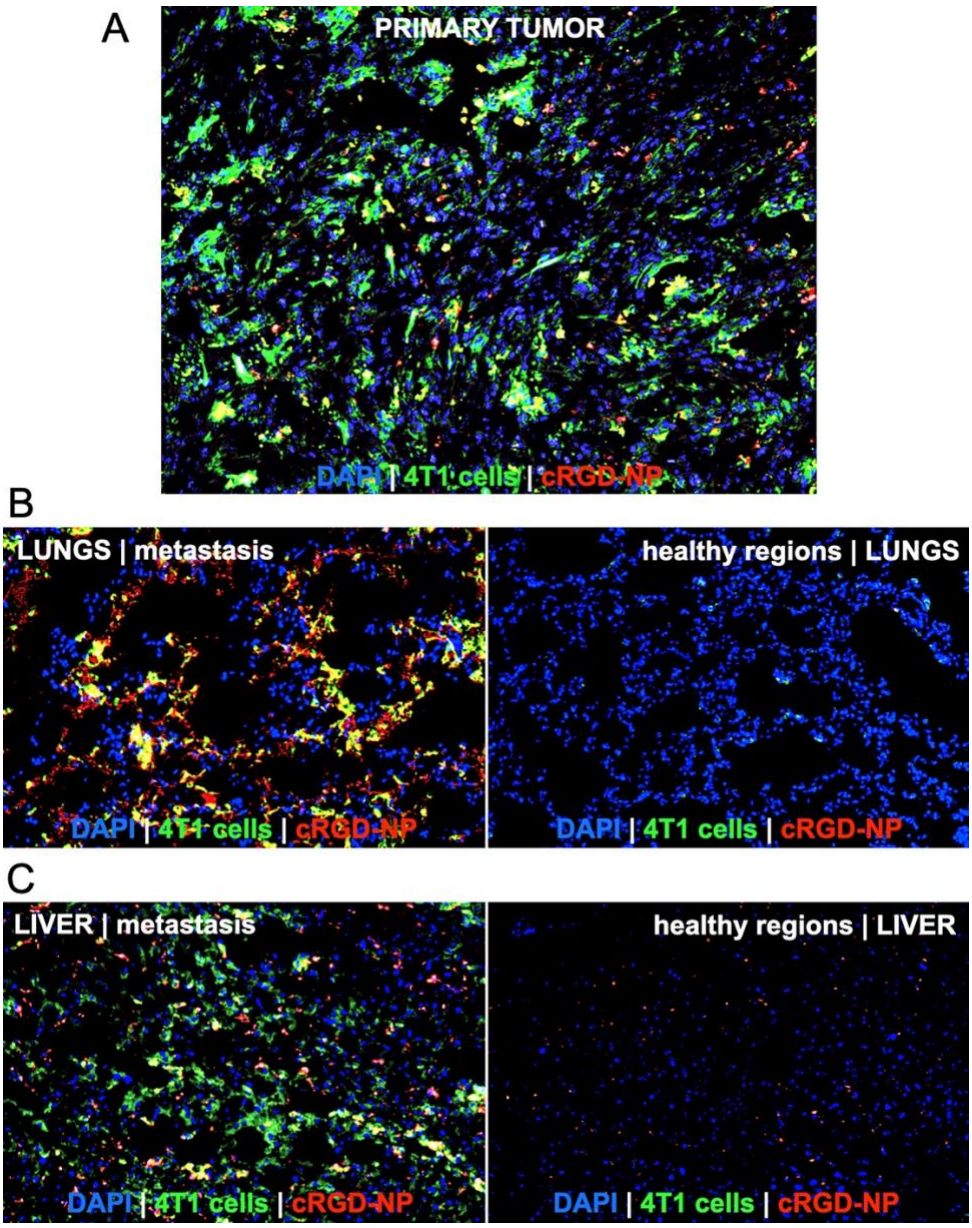

*Figure 4.7 Histological evaluation of the microdistribution of NPs in primary tumor and sites of metastasis and healthy tissue regions in liver and lungs***.**

(A) Primary tumor, **(B)** lungs, and **(C)** liver. (20x magnification; scale bar = 100 μm; blue: nuclear stain, green: 4T1 cancer cells, red: cRGD-NP; metastatic tissue sections left and healthy tissue regions right).

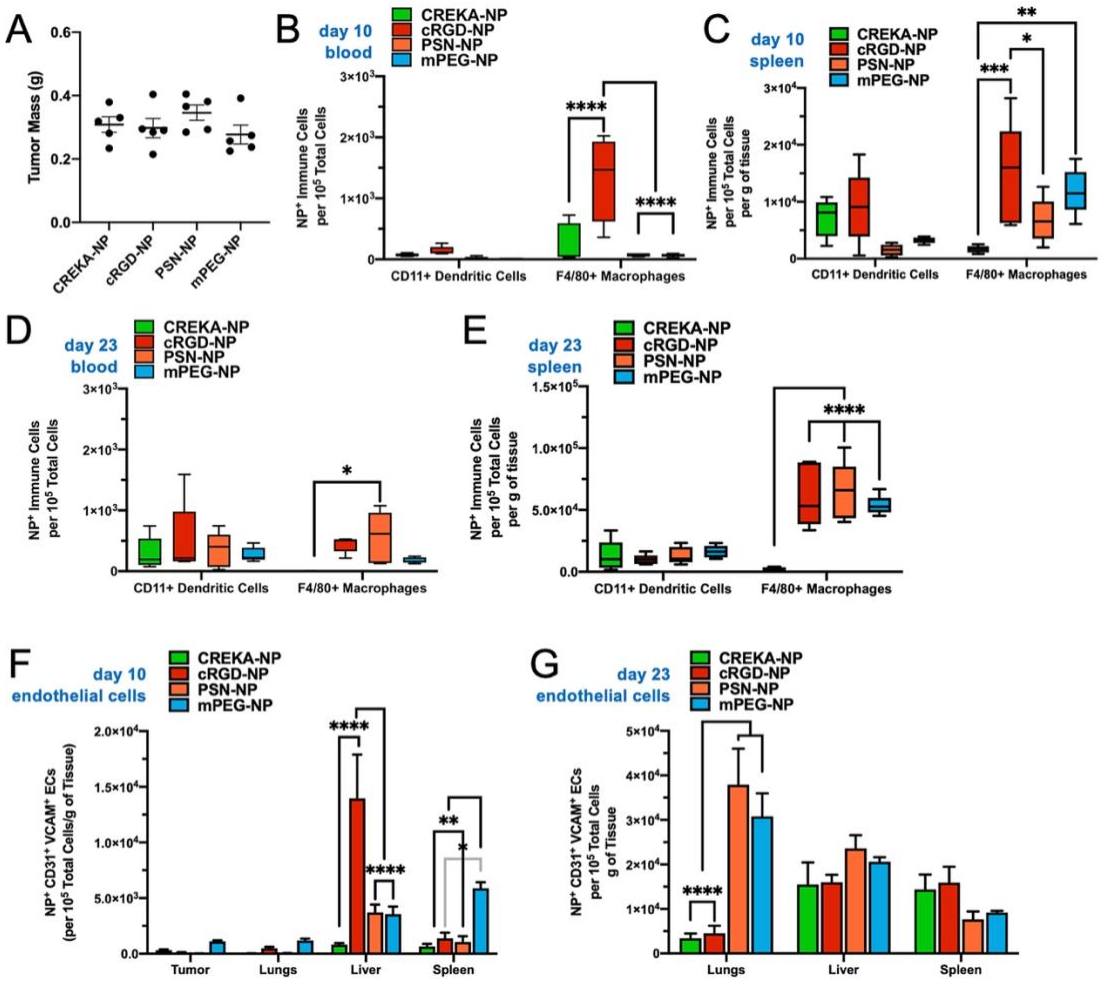

Figure 4.8 Microdistribution and uptake of untargeted and targeted NPs by innate immune cells in the blood and the spleen and endothelial cells in tumor, lungs, liver and spleen.

(A) Weight of primary tumors. **(B–E)** Flow cytometry analysis of nanoparticle uptake by APCs in the blood and the spleen on day 10 and day 23. Analysis of nanoparticle uptake by endothelial cells on **(F)** day 10 and **(G)** day 23. N=5 mice per condition. Box and whisker plots (5-95 percentile) with statistics by one-/two-way ANOVA with a *post hoc* Tukey or Sidak's test**.** *P<0.05; **P<0.01; ***P<0.001; ****P<0.0001.

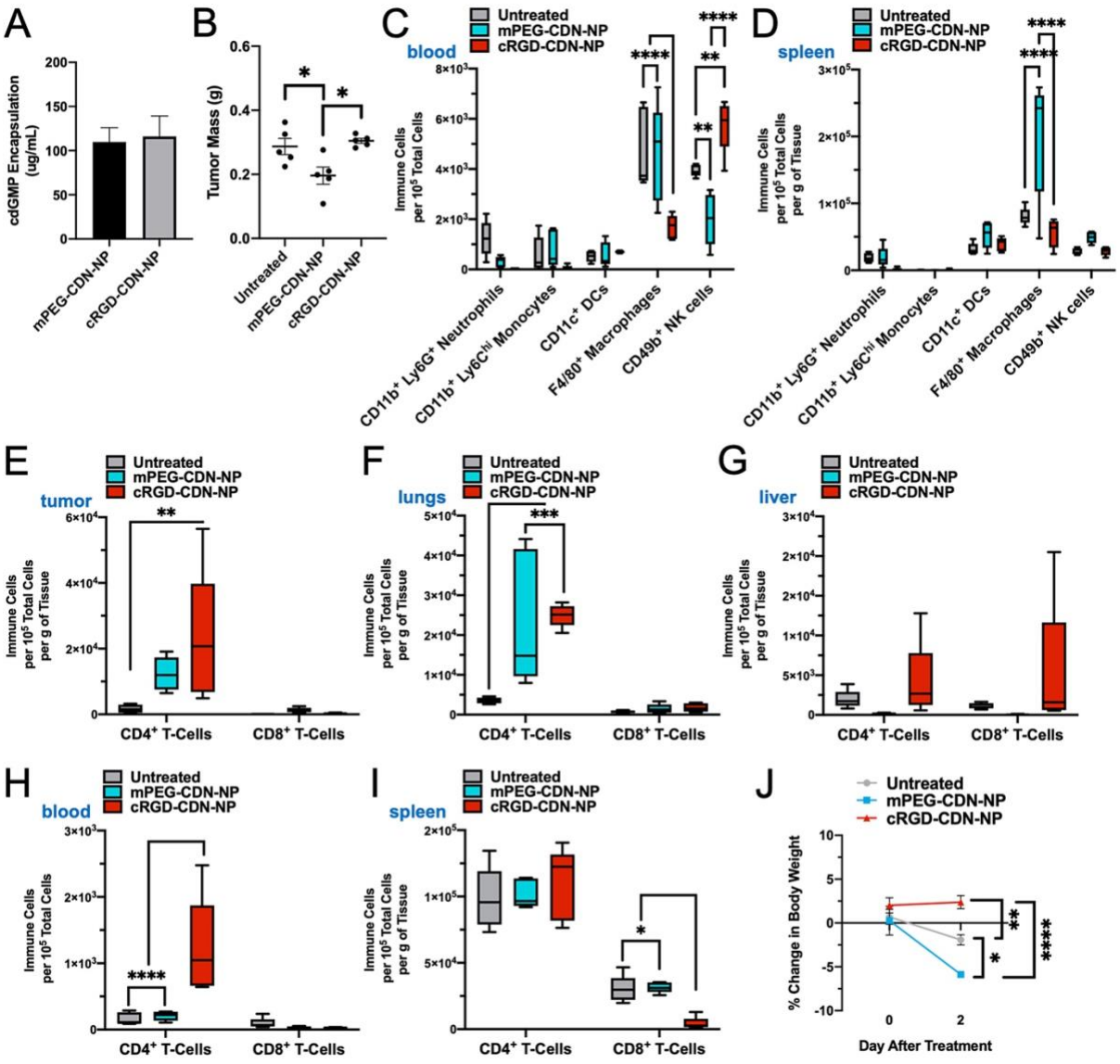

Figure 4.9 Mechanistic study of the cellular immune response to immunostimulatory NPs 48 h after systemic delivery.

(A) cdGMP encapsulation in untargeted and integrin-targeting NPs. **(B)** Weight of primary tumors was measured 2 days after NP treatment on day 10. Flow cytometry analysis of innate immune cells in **(C)** blood and **(D)** spleen, and $CD4^+$ and $CD8^+$ T cells in **(E)** Tumor, **(F)** lungs, **(G)** liver, **(H)** blood and **(I)** spleen. **(J)** Percent body weight change two days post-treatment. N=5 mice per condition. Box and whisker plots (5-95 percentile) both with

statistics by one-/two-way ANOVA with a *post hoc* Tukey or Sidak's test**.** *P<0.05; **P<0.01; ***P<0.001; ****P<0.0001.

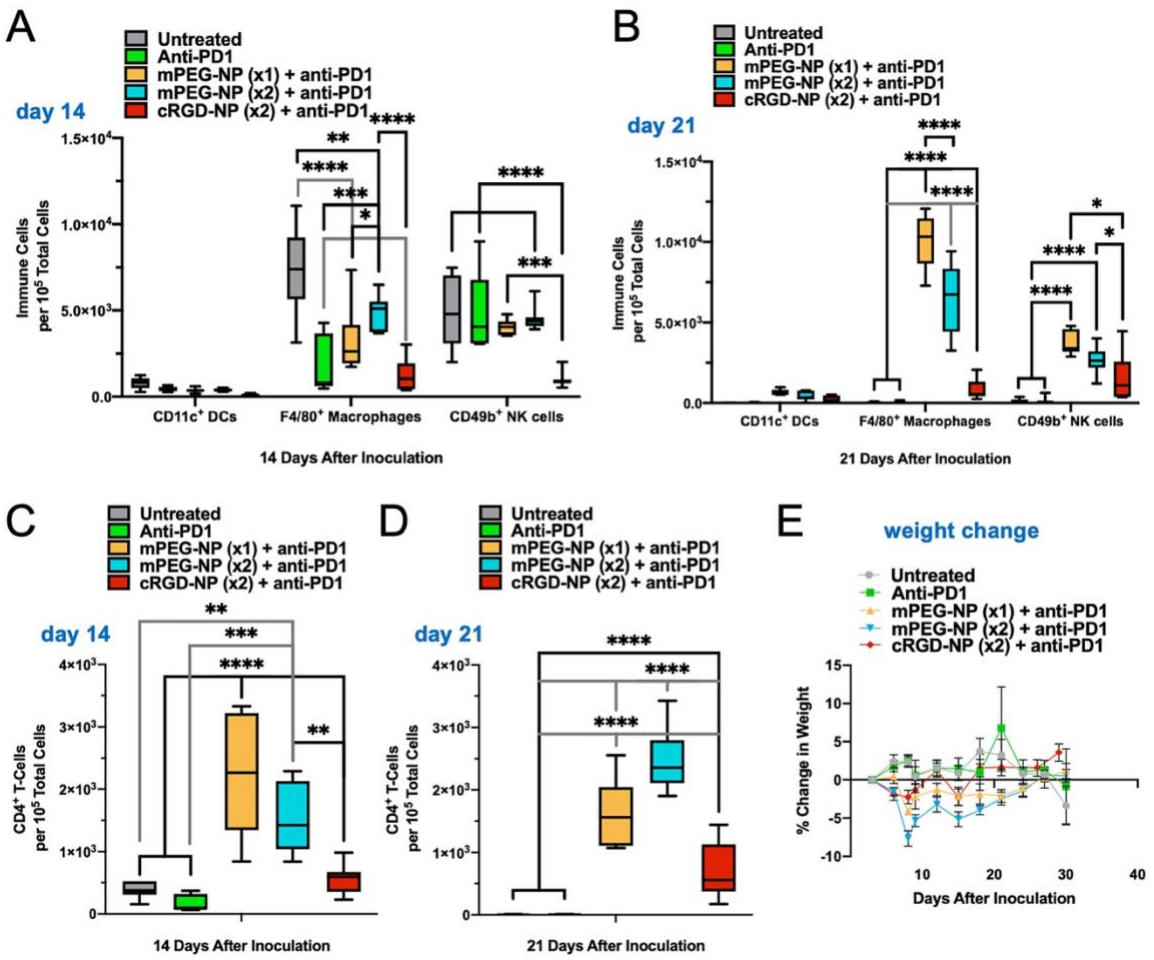

Figure 4.10 Peripheral innate and adaptive immune cells in blood after treatment with immunostimulatory NPs in combination with surgery and anti-PD1.

Flow cytometry analysis of circulating dendritic cells, macrophages and NK cells **(A)** 14 and **(B)** 21 days after tumor inoculation. Peripheral $CD4^+$ T cell counts **(C)** 14 and **(D)** 21 days after tumor inoculation. **(E)** Weight change of mice. N=7 mice per condition. Mean ± SEM are plotted with statistics by one-/two-way ANOVA with a *post hoc* Tukey or Sidak's test**.** *P<0.05; **P<0.01; ***P<0.001; ****P<0.0001.

Chapter 5: Summary and Future Directions

5.1 Summary

The goal of this dissertation was to improve upon current diagnostic and treatment techniques for metastatic breast cancer. Metastatic lesions are both spatially and temporally dynamic with a heterogenicity in respect to cellular and extracellular content. Metastatic tumor microenvironments (TMEs) also have unique characteristics that are not observed by healthy tissues. These TMEs overexpress biomarkers such as adhesion molecules, cell surface receptors, and matrix protein that assist in tumor progression and escape. Here we used nanoparticles to exploit these biomarkers by targeting them to deliver diagnostic and therapeutic agents.

The research objectives were: 1) to develop nanoparticle targeting schemes for imaging metastatic breast cancer, 2) to apply nanoparticle targeting schemes for chemotherapeutic delivery to metastatic breast cancer and 3) to apply nanoparticle targeting schemes for immunostimulatory delivery to metastatic breast cancer. The work and summarization of these objectives are described in the following sections. For future directions, we observe the implications of this research on targeting other hard-to-reach cancers such as pancreatic and brain tumors.

5.1.1 – Objective 1: To Develop Nanoparticle Targeting Schemes for Imaging Metastatic Breast Cancer

As described, metastatic tumor microenvironments display a host of vascular targetable biomarkers.[94,95,108,109,124–132] By targeting tumor-associated biomarkers via a nanoparticle surface decorated with targeting ligands, we can deposit imaging cargo to these difficult-to-target regions. **In Chapter 2, we hypothesize that developing a multi-ligand nanoparticle will allow for its maximal deposition across temporally and**

spatially variant metastatic niches capturing the dynamic and heterogenic tumor microenvironment. Through exploring this new paradigm of multi-targeted nanoparticles, we were able to observe nearly a 3-fold increase in nanoparticle deposition compared to that of its single-ligand nanoparticle variants; this yielded a near ~7% deposition of the injected dose. In a dual-ligand nanoparticle, a 2-fold increase in deposition was observed compared to the single-ligand analog, which still amounted to a significant accumulation percentage. While these initial targeting studies were performed *ex vivo*, *in vivo* imaging of metastasis using a multi-ligand nanoparticle exhibited a high degree of localization to metastatic regions as observed through PET imaging and confirmed via *ex vivo* metastatic cell tracking. The precise metastatic targeting of a nanoparticle contrast agent carrier pushes this platform technology to be used for therapeutic purposes as highlighted by the subsequent objectives.

5.1.2 – Objective 2: To Apply Nanoparticle Targeting Schemes for Chemotherapeutic Delivery to Metastatic Breast Cancer

In the case of a therapeutic protocol, we employed the use of a multi-ligand nanoparticle to deliver chemotherapeutic agents to metastatic breast cancer. **In chapter 3, we hypothesize that by using a similar multi-ligand targeting approach we will be able to deliver a maximal chemotherapeutic payload to an aggressive metastatic triple negative breast cancer in an effort to yield an improved prognosis and survival.** As a platform technology approach, we used a dual-ligand nanoparticle aimed to target adhesion molecules (β_3 and β_1 integrins) and cell specific markers (EGFR) involved in the onset of metastatic disease as cells transition through the epithelial-mesenchymal transition (EMT) and vice versa. When compared to its monolithic targeting versions, the dual-ligand

nanoparticle was able to more proficiently deliver chemotherapeutic agents to the metastatic disease; and as a result, it either reduced or prevented its outgrowth. In this approach, we delivered doxorubicin (DOX), an adjuvant chemotherapeutic, aimed to induced programmed cell death via apoptosis. This approach yielded a significant outcome when compared to freely administered DOX and/or its single-targeted nanoparticle variants. The versatility of the nanoparticle used, a liposome, not only enables the delivery of DOX but can be transformative such that other chemotherapeutic agents may also be encapsulated and administered using this platform technology. While chemotherapy can elicit remission, it does not ensure a prevention of recurrence. Thus, in the subsequent chapter we aimed to deliver an immunostimulatory molecule that would promote immunological memory in order to reduce the likelihood of recurrence.

5.2.3 – Objective 3: To Apply Nanoparticle Targeting Schemes for Immunostimulatory Delivery to Metastatic Breast Cancer

Similar to chapter 2, in chapter 3 we identified the need to develop a multi-ligand nanoparticle to deliver maximal chemotherapeutic and imaging agent cargo. In chapter 4, we address the question of the necessity of such targeting schemes for immunstimulatory delivery. **Here, we hypothesize that the identification of a targeting scheme for the delivery of an immuno-nanoparticle will yield a profound recruitment and expansion of both innate and adaptive immune cells within tumor margins and in circulation.** While previous research focused on solely metastatic disease, in this objective we aimed to develop a model closely tangent to that of a clinical scenario. Here we treated mice bearing both a solid tumor and visceral metastasis using our immuno-nanoparticle formulation. The immuno-nanoparticle was loaded with cdGMP, an immunostimulatory

molecule, where upon its delivery to STING expressing cells – primarily innate immune cells – could yield a robust and self-propagating release of interferons[48–52]. With an increase in interferon secretion, a reactivation of the innate immune system can be observed within a locally suppressive tumor microenvironment. Innate activation will lead to a recruitment of APCs (i.e. dendritic cells, NK cells and macrophages) and adaptive immune cells (i.e. $CD8^+$ T- and $CD4^+$ T-cells) post-antigen priming.

In terms of targeting strategies, nanoparticles are intrinsically designed to naturally drain and accumulate within the perivascular space of tumor microenvironments due to the leaky and ill-formed angiogenic blood vessels in cancerous regions. Untargeted nanoparticles are the main beneficiary of the EPR effect observed in established solid tumors due their long circulation times. [13,21] Thus, in this objective not only did we evaluate nanoparticle targeting schemes previously described but also untargeted nanoparticle formulations to identify which analog would significantly accumulate within APCs closely associated to the tumor microenvironment. It was observed that an untargeted nanoparticle had significant accumulation within solid tumor margins while integrin-targeted nanoparticles had significant accumulation in sites of early metastasis. Both of these conditions witnessed an increase in immune cell recruitment when compared to an untreated scenario with the untargeted formulation as a frontrunner. This can be explained such that the antigen payload observed in the solid tumor is fated to observe a more dramatic influx of macrophages, dendritic cells and NK cells. Regardless, both formulations yielded outstanding survival. For a purely metastatic tumor model, it is postulated that an integrin-targeted nanoparticle would be the beneficiary. The variance in

targeting approaches detail the complexity of the disease however, indicate that these targeting schemes may enable methods for successful diagnosis and treatment.

5.2 Significance

The low cure rate of metastatic breast cancer is due to two separate mechanisms: 1) micrometastasis are not dependably detected and 2) there is a reduction in therapeutic progression as systemically administered agents are not adequately facilitated to metastatic lesions. Therefore, a different systemic approach is required to effectively traffic such agents to improve upon the low response rate.

Metastatic niches are often associated with an increase in biomarker expression including matrix proteins, adhesion molecules and cell specific markers[94,95,108,109,124–132]. In an effort to exploit these upregulated receptors, nanotechnology is capable of incorporating site-specific targeting through the surface ligation of tumor targeting ligands. Furthermore, nanotechnology offers significant advantages as their design allows for a highly tunable structure-to-function relationship; for example, nanoparticles have the unique capability to efficiently encapsulate contrast and therapeutic agents[13,36,39]. Using these targeting strategies, we have evaluated the use of nanoparticles for diagnostic and therapeutic (chemotherapeutic and immunotherapeutic) purposes. We observed that multi-targeted nanoparticle constructs are able to successfully deliver contrast and chemotherapeutic agents because they are able to capture metastatic heterogenicity and its dynamic behavior. For diagnostic and chemotherapeutic purposes, it is vital for nanoparticle carriers to localize themselves to each metastatic lesion such that sufficient tumor margin discerning and eradication is possible.

Immunotherapeutic delivery as the treatment strategy requires a different approach. Immunotherapy is meant to initiate an anti-tumor response via immune cell reactivation. This response is systemic in that activated immune cells will traffic themselves to

metastatic microenvironments upon tumor antigen priming. Thus, our approach slightly differed in that multivalent targeting was no longer required as the immune system would compensate. The development of nanoparticle targeting schemes for variant approaches depicts the complexity but achievability of cargo delivery to sites of metastasis.

5.3 Future Directions

In this dissertation we focused on the delivery of contrast, chemotherapeutic and immunotherapeutic agents to metastatic breast cancers via tumor-targeted liposomal nanoparticles. When discussing the delivery of immunotherapeutic agents, we were able to develop an innate and adaptive response such that treated mouse tumor models entered remission, recurrence was reduced and an increase in systemic immunity was observed. Here, we choose to use a liposomal carrier as efforts to push this technology forward and to the clinic had more clarity than other nanoparticle variants. Liposomal nanoparticles have a long history in the clinic as they have been used to deliver a multitude of chemotherapeutic agents including both anthracyclines, taxanes and platinum-based agents.[138–141] Thus, the likelihood of scalability is realistic due to pre-existing GMP and GLP facilities.[138–141] Furthermore, the immunostimulatory molecule used to realize an *in situ* vaccination, the STING agonist (i.e. CDN), is currently undergoing clinical trials with the hopes of obtaining FDA approval.[142–144] Suitably, the integration of a liposomal carrier and CDN is possible and highly scalable. Additionally, in this research, we observed the categorical improvement of multitargeting schemes when it came to therapeutic outcomes. While multitargeting may be very attractive at the research level it may be difficult to implement when developing a product that requires extensive scaling. Future distillation of this work is required such that reproducibility is ensured. Lastly, upon reaching clinical trials with a formulation that assimilates both targeting and a *de novo* therapeutic extensive toxicity, dose escalation and safety profiles are required in order to effectively proceed.

While this dissertation focused on metastatic breast cancer, studies have been initiated to explore and develop targeting strategies for other hard-to-reach cancers

including pancreatic and brain tumors. Specifically, we have taken an extensive look at targeting glioblastoma multiforme (GBM) due its aggressive and infiltrative nature that yields an abysmal prognosis. GBMs are categorically, like metastasis, difficult to manage as there are an assortment of physical barriers (i.e. blood-brain barrier, regions of hypoxia, high interstitial pressure and efflux pumps) that prevent an adequate accumulation of contrast or drug agents for either diagnostic or therapeutic purposes, respectively[30,66,145–147]. However, also like metastasis, the endothelium and near-perivascular regions adjacent to GBMs are a direct reflection on the health of the underlying tissue. Due to GBM outgrowth, the vasculature is displays distress signals in the form of upregulated biomarkers that are easily accessible to systemically administered targeted-nanoparticles[38,64,69,119,147].

The similarities in targeting between GBM and metastatic tumor microenvironments have enabled us to consider applying some of the techniques used in this dissertation. A commonality with the low prognosis of GBMs are the inadequacies of tumor progression and stratification as a function of a therapeutic timeline. Thus, as an initial approach, we aim to develop targeting strategies that will aid in improving the diagnosis of GBMs. The recruitment or local production of nonendogenous matrix proteins are highly correlated with GBM progression, invasion and distal dispersions. Fibronectin/fibrinogen mesh networks are developed through the deposition of these proteins in regions adjacent to an injured endothelium and further establish and motivate the onset of disease (**Fig 5.3)**[38]. Receptor protein tyrosine phosphatase mu (PTP-μ), is a catalytically cleaved cell-cell adhesion molecule that when processed acts as an extracellular matrix protein found in both aggressive forms of adult and pediatric GBMs

(**Fig 5.2)**[148]. In two separate studies, we observed the functionality of using these upregulated biomarkers as targeted ligands for enhanced nanoparticle deposition. For these studies, we developed an iron-oxide based nanoparticle that was comprised of 3-5 linearly linked iron oxide spheres termed nanochain (**Fig 5.1)**. Due to the iron oxide content, its intrinsic properties – high T2 relaxivity – enabled us to use such the nanochain as a T2-weighted contrast agent for MR imaging. In separate studies, using a fibrin targeted-nanoparticle and a PTP-μ targeted-nanoparticle, we were able to significantly enhance the T2-weighted MR contrast of GBMs (**Fig 5.2-3)**[38,148]. Furthermore, these targeting schemes enabled us to localize our nanoparticle not only to the solid tumor but also within invasive and distal dispersion tumor margins. This tumor targeting platform depicts a story of successful targetability which can then be further implemented into therapeutic approaches for GBMs such as what was observed in metastatic cancers.

Future research will focus on developing treatment protocols – chemotherapeutic and immunotherapeutic delivery – using nanoparticle targeting schemes for GBMs. In the case of metastasis, while tumor remission was observed in some studies, it is important to further establish proper treatment regimens and dosage escalations to prevent any suggestion of future recurrence.

5.4 Figures

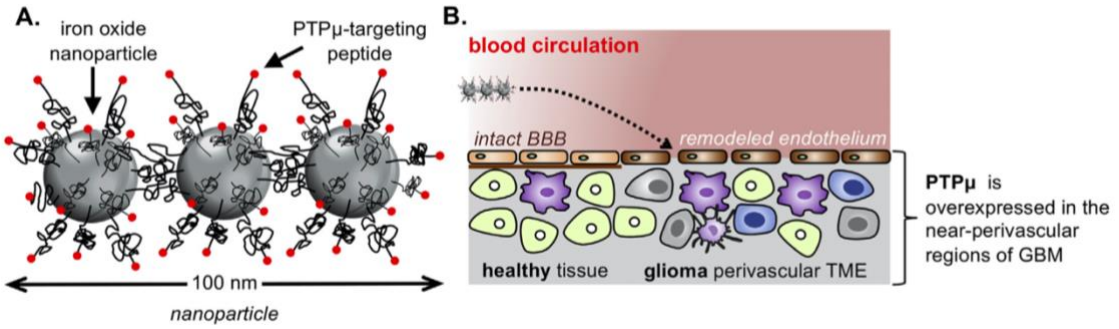

Figure 5.1 Illustration of the nanochain particle and its therapeutic effect on brain tumors.

(A) Schematic of a linear nanochain particle composed of three iron oxide (IO) nanospheres decorated with the PTPμ-targeted agent. (B) Illustration of the successful delivery of drugs to perivascular tumor microenvironment (TME) via vascular targeting of the PTPμ-targeted nanochain.

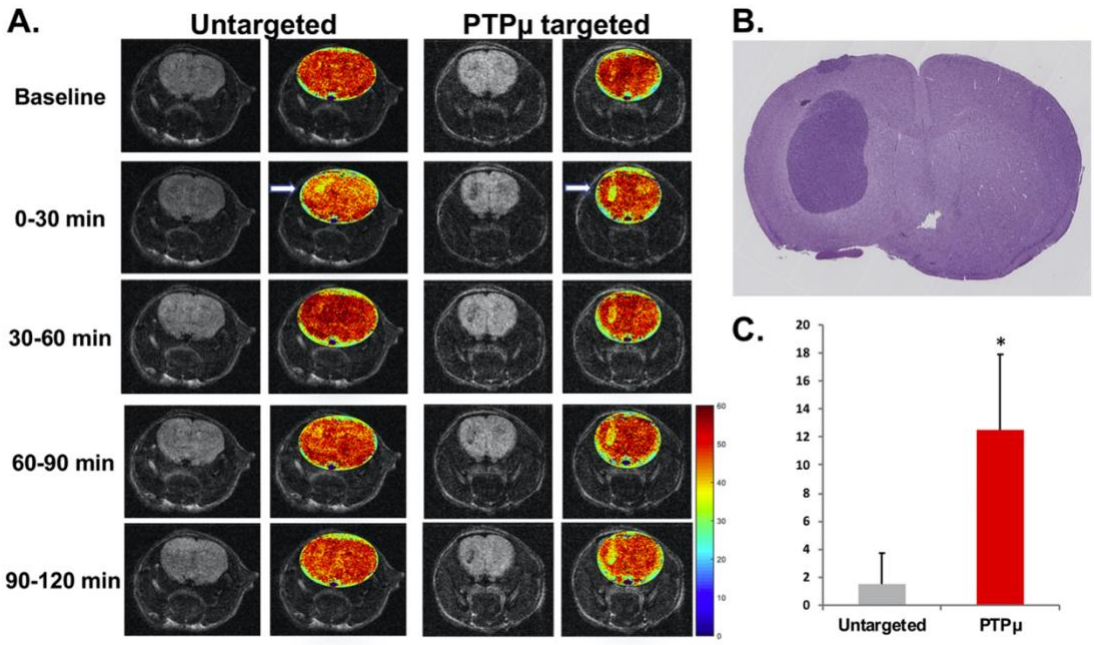

Figure 5.2 The PTPμ-targeted nanochain shows in vivo binding to U-87 MG intracranial tumors and T2-weighted contrast enhancement.

(A) Representative T2 weighted 2D images of U-87 MG orthotopic tumors before (Baseline) and during 30 min increments up to 120 min after intravenous injection of untargeted nanochain or PTPμ-targeted nanochain (n = 4/condition) with pseudo-colored T2 relaxation time map overlays to show contrast uptake. White arrow indicates tumor. Color coded scale bar indicates T2 relaxation time in milliseconds. (B) H & E stained histological section from a representative U-87 MG tumor is shown. (C) Quantification of change in T2 relaxation time (R2 = 1/T2) of U-87 MG intracranial tumor following intravenous administration of the PTPμ-targeted or untargeted iron nanochain (n = 4/condition]. Data shown represent normalized mean percent change in R2 +/− SEM (R2 = 1/T2). Asterisk represents statistical significance, P value = 0.035. Note the increased

percent change in R2 for tumors following administration of the PTPμ-targeted contrast agent.

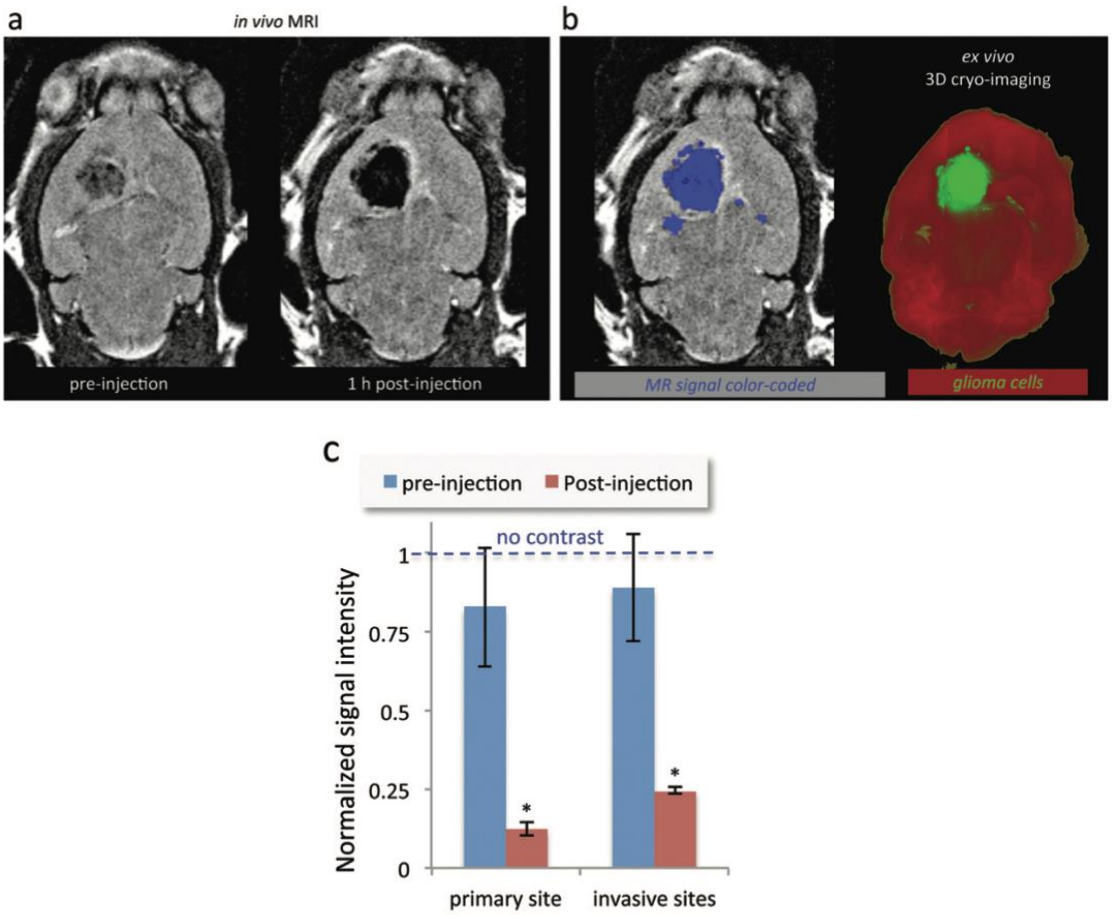

Figure 5.3 Representative in vivo MR images of the brain of mice bearing orthotopic glioma CNS-1 tumors using a 7 T MRI.

(a) Coronal T2-weighted images of the brain of a mouse before and 1 h after injection of CREKA-targeted nanochains. (b) In the 1 h post-injection MR image, the signal enhancement was thresholded and color-coded in blue (left). In the end of MR imaging, the brains of the animals were perfused, excised, and imaged ex vivo using 3D cryo-imaging. 3D cryo-imaging provided an ultra-high-resolution fluorescence volume of the brain showing the topology of CNS-1-GFP cells. The in vivo MR image (left) and the ex vivo fluorescence image (right) show the colocalization of MR signal and glioma cells. (c) The absolute MR signal intensity in gliomas and the healthy brain was measured in

manually drawn ROIs. The signal intensity in glioma sites was normalized to the signal of the corresponding healthy brain region (scale: 0–1). Since lower values indicate greater contrast in T2 images, normalized intensity values of 0 and 1 correspond to maximum and minimum contrast, respectively (data presented as mean ± standard deviation; n = 5; *P < 0.05).

Bibliography

(1) Meng, S.; Tripathy, D.; Frenkel, E. P.; Shete, S.; Naftalis, E. Z.; Huth, J. F.; Beitsch, P. D.; Leitch, M.; Hoover, S.; Euhus, D.; Haley, B.; Morrison, L.; Fleming, T. P.; Herlyn, D.; Terstappen, L. W. M. M.; Fehm, T.; Tucker, T. F.; Lane, N.; Wang, J.; Uhr, J. W. Circulating Tumor Cells in Patients with Breast Cancer Dormancy. *Clin. Cancer Res. Off. J. Am. Assoc. Cancer Res.* **2004**, *10* (24), 8152–8162. https://doi.org/10.1158/1078-0432.CCR-04-1110.

(2) Liedtke, C.; Mazouni, C.; Hess, K. R.; André, F.; Tordai, A.; Mejia, J. A.; Symmans, W. F.; Gonzalez-Angulo, A. M.; Hennessy, B.; Green, M.; Cristofanilli, M.; Hortobagyi, G. N.; Pusztai, L. Response to Neoadjuvant Therapy and Long-Term Survival in Patients with Triple-Negative Breast Cancer. *J. Clin. Oncol. Off. J. Am. Soc. Clin. Oncol.* **2008**, *26* (8), 1275–1281. https://doi.org/10.1200/JCO.2007.14.4147.

(3) André, F.; Zielinski, C. C. Optimal Strategies for the Treatment of Metastatic Triple-Negative Breast Cancer with Currently Approved Agents. *Ann. Oncol. Off. J. Eur. Soc. Med. Oncol.* **2012**, *23 Suppl 6*, vi46-51. https://doi.org/10.1093/annonc/mds195.

(4) Gupta, G. P.; Massagué, J. Cancer Metastasis: Building a Framework. *Cell* **2006**, *127* (4), 679–695. https://doi.org/10.1016/j.cell.2006.11.001.

(5) Li, F.; Tiede, B.; Massagué, J.; Kang, Y. Beyond Tumorigenesis: Cancer Stem Cells in Metastasis. *Cell Res.* **2007**, *17* (1), 3–14. https://doi.org/10.1038/sj.cr.7310118.

(6) Dalerba, P.; Cho, R. W.; Clarke, M. F. Cancer Stem Cells: Models and Concepts. *Annu. Rev. Med.* **2007**, *58*, 267–284. https://doi.org/10.1146/annurev.med.58.062105.204854.

(7) Samanta, D.; Gilkes, D. M.; Chaturvedi, P.; Xiang, L.; Semenza, G. L. Hypoxia-Inducible Factors Are Required for Chemotherapy Resistance of Breast Cancer Stem Cells. *Proc. Natl. Acad. Sci. U. S. A.* **2014**, *111* (50), E5429-5438. https://doi.org/10.1073/pnas.1421438111.

(8) Mani, S. A.; Guo, W.; Liao, M.-J.; Eaton, E. N.; Ayyanan, A.; Zhou, A. Y.; Brooks, M.; Reinhard, F.; Zhang, C. C.; Shipitsin, M.; Campbell, L. L.; Polyak, K.; Brisken, C.; Yang, J.; Weinberg, R. A. The Epithelial-Mesenchymal Transition Generates Cells with Properties of Stem Cells. *Cell* **2008**, *133* (4), 704–715. https://doi.org/10.1016/j.cell.2008.03.027.

(9) Ribas, A.; Wolchok, J. D. Cancer Immunotherapy Using Checkpoint Blockade. *Science* **2018**, *359* (6382), 1350–1355. https://doi.org/10.1126/science.aar4060.

(10) Xu, W.; Dong, J.; Zheng, Y.; Zhou, J.; Yuan, Y.; Ta, M.; Miller, H.; Olson, M.; Rajasekaran, K.; Ernstoff, M.; Wang, D.; Malarkannan, S.; Wang, L. Immune-Checkpoint Protein VISTA Regulates Antitumor Immunity by Controlling Myeloid Cell–Mediated Inflammation and Immunosuppression. *Cancer Immunol. Res.* **2019**, *7*, canimm.0489.2018. https://doi.org/10.1158/2326-6066.CIR-18-0489.

(11) Banys, M.; Hartkopf, A. D.; Krawczyk, N.; Kaiser, T.; Meier-Stiegen, F.; Fehm, T.; Neubauer, H. Dormancy in Breast Cancer. *Breast Cancer Dove Med. Press* **2012**, *4*, 183–191. https://doi.org/10.2147/BCTT.S26431.

(12) Ghajar, C. M. Metastasis Prevention by Targeting the Dormant Niche. *Nat. Rev. Cancer* **2015**, *15* (4), 238–247. https://doi.org/10.1038/nrc3910.

(13) Atukorale, P. U.; Raghunathan, S. P.; Raguveer, V.; Moon, T. J.; Zheng, C.; Bielecki, P. A.; Wiese, M. L.; Goldberg, A. L.; Covarrubias, G.; Hoimes, C. J.; Karathanasis,

E. Nanoparticle Encapsulation of Synergistic Immune Agonists Enables Systemic Codelivery to Tumor Sites and IFNβ-Driven Antitumor Immunity. *Cancer Res.* **2019**, *79* (20), 5394–5406. https://doi.org/10.1158/0008-5472.CAN-19-0381.

(14) Peiris, P. M.; Toy, R.; Doolittle, E.; Pansky, J.; Abramowski, A.; Tam, M.; Vicente, P.; Tran, E.; Hayden, E.; Camann, A.; Mayer, A.; Erokwu, B. O.; Berman, Z.; Wilson, D.; Baskaran, H.; Flask, C. A.; Keri, R. A.; Karathanasis, E. Imaging Metastasis Using an Integrin-Targeting Chain-Shaped Nanoparticle. *ACS Nano* **2012**, *6* (10), 8783–8795. https://doi.org/10.1021/nn303833p.

(15) Doolittle, E.; Peiris, P. M.; Doron, G.; Goldberg, A.; Tucci, S.; Rao, S.; Shah, S.; Sylvestre, M.; Govender, P.; Turan, O.; Lee, Z.; Schiemann, W. P.; Karathanasis, E. Spatiotemporal Targeting of a Dual-Ligand Nanoparticle to Cancer Metastasis. *ACS Nano* **2015**, *9* (8), 8012–8021. https://doi.org/10.1021/acsnano.5b01552.

(16) Peiris, P. M.; Deb, P.; Doolittle, E.; Doron, G.; Goldberg, A.; Govender, P.; Shah, S.; Rao, S.; Carbone, S.; Cotey, T.; Sylvestre, M.; Singh, S.; Schiemann, W. P.; Lee, Z.; Karathanasis, E. Vascular Targeting of a Gold Nanoparticle to Breast Cancer Metastasis. *J. Pharm. Sci.* **2015**, *104* (8), 2600–2610. https://doi.org/10.1002/jps.24518.

(17) Toy, R.; Hayden, E.; Camann, A.; Berman, Z.; Vicente, P.; Tran, E.; Meyers, J.; Pansky, J.; Peiris, P. M.; Wu, H.; Exner, A.; Wilson, D.; Ghaghada, K. B.; Karathanasis, E. Multimodal in Vivo Imaging Exposes the Voyage of Nanoparticles in Tumor Microcirculation. *ACS Nano* **2013**, *7* (4), 3118–3129. https://doi.org/10.1021/nn3053439.

(18) Covarrubias, G.; Cha, A.; Rahmy, A.; Lorkowski, M.; Perera, V.; Erokwu, B. O.; Flask, C.; Peiris, P. M.; Schiemann, W. P.; Karathanasis, E. Imaging Breast Cancer Using a Dual-Ligand Nanochain Particle. *PloS One* **2018**, *13* (10), e0204296. https://doi.org/10.1371/journal.pone.0204296.

(19) Peiris, P. M.; He, F.; Covarrubias, G.; Raghunathan, S.; Turan, O.; Lorkowski, M.; Gnanasambandam, B.; Wu, C.; Schiemann, W. P.; Karathanasis, E. Precise Targeting of Cancer Metastasis Using Multi-Ligand Nanoparticles Incorporating Four Different Ligands. *Nanoscale* **2018**, *10* (15), 6861–6871. https://doi.org/10.1039/c8nr02513d.

(20) Covarrubias, G.; He, F.; Raghunathan, S.; Turan, O.; Peiris, P. M.; Schiemann, W. P.; Karathanasis, E. Effective Treatment of Cancer Metastasis Using a Dual-Ligand Nanoparticle. *PloS One* **2019**, *14* (7), e0220474. https://doi.org/10.1371/journal.pone.0220474.

(21) Borsi, L.; Balza, E.; Bestagno, M.; Castellani, P.; Carnemolla, B.; Biro, A.; Leprini, A.; Sepulveda, J.; Burrone, O.; Neri, D.; Zardi, L. Selective Targeting of Tumoral Vasculature: Comparison of Different Formats of an Antibody (L19) to the ED-B Domain of Fibronectin. *Int. J. Cancer* **2002**, *102* (1), 75–85. https://doi.org/10.1002/ijc.10662.

(22) Coghlin, C.; Murray, G. I. Current and Emerging Concepts in Tumour Metastasis. *J. Pathol.* **2010**, *222* (1), 1–15. https://doi.org/10.1002/path.2727.

(23) Gay, L. J.; Felding-Habermann, B. Contribution of Platelets to Tumour Metastasis. *Nat. Rev. Cancer* **2011**, *11* (2), 123–134. https://doi.org/10.1038/nrc3004.

(24) Modery, C. L.; Ravikumar, M.; Wong, T. L.; Dzuricky, M. J.; Durongkaveroj, N.; Sen Gupta, A. Heteromultivalent Liposomal Nanoconstructs for Enhanced Targeting

and Shear-Stable Binding to Active Platelets for Site-Selective Vascular Drug Delivery. *Biomaterials* **2011**, *32* (35), 9504–9514. https://doi.org/10.1016/j.biomaterials.2011.08.067.

(25) Zhang, Q.; Yang, M.; Shen, J.; Gerhold, L. M.; Hoffman, R. M.; Xing, H. R. The Role of the Intravascular Microenvironment in Spontaneous Metastasis Development. *Int. J. Cancer* **2010**, *126* (11), 2534–2541. https://doi.org/10.1002/ijc.24979.

(26) Karathanasis, E.; Chan, L.; Karumbaiah, L.; McNeeley, K.; D'Orsi, C. J.; Annapragada, A. V.; Sechopoulos, I.; Bellamkonda, R. V. Tumor Vascular Permeability to a Nanoprobe Correlates to Tumor-Specific Expression Levels of Angiogenic Markers. *PloS One* **2009**, *4* (6), e5843. https://doi.org/10.1371/journal.pone.0005843.

(27) Neri, D.; Bicknell, R. Tumour Vascular Targeting. *Nat. Rev. Cancer* **2005**, *5* (6), 436–446. https://doi.org/10.1038/nrc1627.

(28) Atukorale, P. U.; Covarrubias, G.; Bauer, L.; Karathanasis, E. Vascular Targeting of Nanoparticles for Molecular Imaging of Diseased Endothelium. *Adv. Drug Deliv. Rev.* **2017**, *113*, 141–156. https://doi.org/10.1016/j.addr.2016.09.006.

(29) Zhou, Z.; Qutaish, M.; Han, Z.; Schur, R. M.; Liu, Y.; Wilson, D. L.; Lu, Z.-R. MRI Detection of Breast Cancer Micrometastases with a Fibronectin-Targeting Contrast Agent. *Nat. Commun.* **2015**, *6*, 7984. https://doi.org/10.1038/ncomms8984.

(30) Serres, E.; Debarbieux, F.; Stanchi, F.; Maggiorella, L.; Grall, D.; Turchi, L.; Burel-Vandenbos, F.; Figarella-Branger, D.; Virolle, T.; Rougon, G.; Van Obberghen-Schilling, E. Fibronectin Expression in Glioblastomas Promotes Cell Cohesion,

Collective Invasion of Basement Membrane in Vitro and Orthotopic Tumor Growth in Mice. *Oncogene* **2014**, *33* (26), 3451–3462. https://doi.org/10.1038/onc.2013.305.

(31) Ohnishi, T.; Hiraga, S.; Izumoto, S.; Matsumura, H.; Kanemura, Y.; Arita, N.; Hayakawa, T. Role of Fibronectin-Stimulated Tumor Cell Migration in Glioma Invasion in Vivo: Clinical Significance of Fibronectin and Fibronectin Receptor Expressed in Human Glioma Tissues. *Clin. Exp. Metastasis* **1998**, *16* (8), 729–741. https://doi.org/10.1023/a:1006532812408.

(32) Haubner, R.; Maschauer, S.; Prante, O. PET Radiopharmaceuticals for Imaging Integrin Expression: Tracers in Clinical Studies and Recent Developments. *BioMed Res. Int.* **2014**, *2014*, 871609. https://doi.org/10.1155/2014/871609.

(33) Molenaar, T. J. M.; Appeldoorn, C. C. M.; de Haas, S. A. M.; Michon, I. N.; Bonnefoy, A.; Hoylaerts, M. F.; Pannekoek, H.; van Berkel, T. J. C.; Kuiper, J.; Biessen, E. A. L. Specific Inhibition of P-Selectin-Mediated Cell Adhesion by Phage Display-Derived Peptide Antagonists. *Blood* **2002**, *100* (10), 3570–3577. https://doi.org/10.1182/blood-2002-02-0641.

(34) Cheng, Y.; Meyers, J. D.; Agnes, R. S.; Doane, T. L.; Kenney, M. E.; Broome, A.-M.; Burda, C.; Basilion, J. P. Addressing Brain Tumors with Targeted Gold Nanoparticles: A New Gold Standard for Hydrophobic Drug Delivery? *Small Weinh. Bergstr. Ger.* **2011**, *7* (16), 2301–2306. https://doi.org/10.1002/smll.201100628.

(35) Gentile, F.; Chiappini, C.; Fine, D.; Bhavane, R. C.; Peluccio, M. S.; Cheng, M. M.-C.; Liu, X.; Ferrari, M.; Decuzzi, P. The Effect of Shape on the Margination Dynamics of Non-Neutrally Buoyant Particles in Two-Dimensional Shear Flows. *J. Biomech.* **2008**, *41* (10), 2312–2318. https://doi.org/10.1016/j.jbiomech.2008.03.021.

(36) Lee, S.-Y.; Ferrari, M.; Decuzzi, P. Shaping Nano-/Micro-Particles for Enhanced Vascular Interaction in Laminar Flows. *Nanotechnology* **2009**, *20* (49), 495101. https://doi.org/10.1088/0957-4484/20/49/495101.

(37) Toy, R.; Hayden, E.; Shoup, C.; Baskaran, H.; Karathanasis, E. The Effects of Particle Size, Density and Shape on Margination of Nanoparticles in Microcirculation. *Nanotechnology* **2011**, *22* (11), 115101. https://doi.org/10.1088/0957-4484/22/11/115101.

(38) Perera, V. S.; Covarrubias, G.; Lorkowski, M.; Atukorale, P.; Rao, A.; Raghunathan, S.; Gopalakrishnan, R.; Erokwu, B. O.; Liu, Y.; Dixit, D.; Brady-Kalnay, S. M.; Wilson, D.; Flask, C.; Rich, J.; Peiris, P. M.; Karathanasis, E. One-Pot Synthesis of Nanochain Particles for Targeting Brain Tumors. *Nanoscale* **2017**, *9* (27), 9659–9667. https://doi.org/10.1039/c7nr02370g.

(39) Toy, R.; Peiris, P. M.; Ghaghada, K. B.; Karathanasis, E. Shaping Cancer Nanomedicine: The Effect of Particle Shape on the in Vivo Journey of Nanoparticles. *Nanomed.* **2014**, *9* (1), 121–134. https://doi.org/10.2217/nnm.13.191.

(40) Saul, J. M.; Annapragada, A.; Natarajan, J. V.; Bellamkonda, R. V. Controlled Targeting of Liposomal Doxorubicin via the Folate Receptor in Vitro. *J. Control. Release Off. J. Control. Release Soc.* **2003**, *92* (1–2), 49–67. https://doi.org/10.1016/s0168-3659(03)00295-5.

(41) Fukumura, D.; Duda, D. G.; Munn, L. L.; Jain, R. K. Tumor Microvasculature and Microenvironment: Novel Insights Through Intravital Imaging in Pre-Clinical Models. *Microcirc. N. Y. N 1994* **2010**, *17* (3), 206–225. https://doi.org/10.1111/j.1549-8719.2010.00029.x.

(42) Karathanasis, E.; Suryanarayanan, S.; Balusu, S. R.; McNeeley, K.; Sechopoulos, I.; Karellas, A.; Annapragada, A. V.; Bellamkonda, R. V. Imaging Nanoprobe for Prediction of Outcome of Nanoparticle Chemotherapy by Using Mammography. *Radiology* **2009**, *250* (2), 398–406. https://doi.org/10.1148/radiol.2502080801.

(43) Bipat, S.; van Leeuwen, M. S.; Comans, E. F. I.; Pijl, M. E. J.; Bossuyt, P. M. M.; Zwinderman, A. H.; Stoker, J. Colorectal Liver Metastases: CT, MR Imaging, and PET for Diagnosis--Meta-Analysis. *Radiology* **2005**, *237* (1), 123–131. https://doi.org/10.1148/radiol.2371042060.

(44) Joyce, J. A.; Fearon, D. T. T Cell Exclusion, Immune Privilege, and the Tumor Microenvironment. *Science* **2015**, *348* (6230), 74–80. https://doi.org/10.1126/science.aaa6204.

(45) Klein, C. A. Framework Models of Tumor Dormancy from Patient-Derived Observations. *Curr. Opin. Genet. Dev.* **2011**, *21* (1), 42–49. https://doi.org/10.1016/j.gde.2010.10.011.

(46) Eccles, S. A.; Aboagye, E. O.; Ali, S.; Anderson, A. S.; Armes, J.; Berditchevski, F.; Blaydes, J. P.; Brennan, K.; Brown, N. J.; Bryant, H. E.; Bundred, N. J.; Burchell, J. M.; Campbell, A. M.; Carroll, J. S.; Clarke, R. B.; Coles, C. E.; Cook, G. J. R.; Cox, A.; Curtin, N. J.; Dekker, L. V.; Silva, I. dos S.; Duffy, S. W.; Easton, D. F.; Eccles, D. M.; Edwards, D. R.; Edwards, J.; Evans, D.; Fenlon, D. F.; Flanagan, J. M.; Foster, C.; Gallagher, W. M.; Garcia-Closas, M.; Gee, J. M. W.; Gescher, A. J.; Goh, V.; Groves, A. M.; Harvey, A. J.; Harvie, M.; Hennessy, B. T.; Hiscox, S.; Holen, I.; Howell, S. J.; Howell, A.; Hubbard, G.; Hulbert-Williams, N.; Hunter, M. S.; Jasani, B.; Jones, L. J.; Key, T. J.; Kirwan, C. C.; Kong, A.; Kunkler, I. H.; Langdon, S. P.;

Leach, M. O.; Mann, D. J.; Marshall, J. F.; Martin, L.; Martin, S. G.; Macdougall, J. E.; Miles, D. W.; Miller, W. R.; Morris, J. R.; Moss, S. M.; Mullan, P.; Natrajan, R.; O'Connor, J. P. B.; O'Connor, R.; Palmieri, C.; Pharoah, P. D. P.; Rakha, E. A.; Reed, E.; Robinson, S. P.; Sahai, E.; Saxton, J. M.; Schmid, P.; Smalley, M. J.; Speirs, V.; Stein, R.; Stingl, J.; Streuli, C. H.; Tutt, A. N. J.; Velikova, G.; Walker, R. A.; Watson, C. J.; Williams, K. J.; Young, L. S.; Thompson, A. M. Critical Research Gaps and Translational Priorities for the Successful Prevention and Treatment of Breast Cancer. *Breast Cancer Res. BCR* **2013**, *15* (5), R92. https://doi.org/10.1186/bcr3493.

(47) Lemos, H.; Mohamed, E.; Huang, L.; Ou, R.; Pacholczyk, G.; Arbab, A. S.; Munn, D.; Mellor, A. L. STING Promotes the Growth of Tumors Characterized by Low Antigenicity via IDO Activation. *Cancer Res.* **2016**, *76* (8), 2076–2081. https://doi.org/10.1158/0008-5472.CAN-15-1456.

(48) Woo, S.-R.; Fuertes, M. B.; Corrales, L.; Spranger, S.; Furdyna, M. J.; Leung, M. Y. K.; Duggan, R.; Wang, Y.; Barber, G. N.; Fitzgerald, K. A.; Alegre, M.-L.; Gajewski, T. F. STING-Dependent Cytosolic DNA Sensing Mediates Innate Immune Recognition of Immunogenic Tumors. *Immunity* **2014**, *41* (5), 830–842. https://doi.org/10.1016/j.immuni.2014.10.017.

(49) Corrales, L.; McWhirter, S. M.; Dubensky, T. W.; Gajewski, T. F. The Host STING Pathway at the Interface of Cancer and Immunity. *J. Clin. Invest.* **2016**, *126* (7), 2404–2411. https://doi.org/10.1172/JCI86892.

(50) Shae, D.; Becker, K. W.; Christov, P.; Yun, D. S.; Lytton-Jean, A. K. R.; Sevimli, S.; Ascano, M.; Kelley, M.; Johnson, D. B.; Balko, J. M.; Wilson, J. T. Endosomolytic Polymersomes Increase the Activity of Cyclic Dinucleotide STING Agonists to

Enhance Cancer Immunotherapy. *Nat. Nanotechnol.* **2019**, *14* (3), 269–278. https://doi.org/10.1038/s41565-018-0342-5.

(51) Yang, H.; Lee, W. S.; Kong, S. J.; Kim, C. G.; Kim, J. H.; Chang, S. K.; Kim, S.; Kim, G.; Chon, H. J.; Kim, C. STING Activation Reprograms Tumor Vasculatures and Synergizes with VEGFR2 Blockade. *J. Clin. Invest.* *129* (10), 4350–4364. https://doi.org/10.1172/JCI125413.

(52) Demaria, O.; De Gassart, A.; Coso, S.; Gestermann, N.; Di Domizio, J.; Flatz, L.; Gaide, O.; Michielin, O.; Hwu, P.; Petrova, T. V.; Martinon, F.; Modlin, R. L.; Speiser, D. E.; Gilliet, M. STING Activation of Tumor Endothelial Cells Initiates Spontaneous and Therapeutic Antitumor Immunity. *Proc. Natl. Acad. Sci. U. S. A.* **2015**, *112* (50), 15408–15413. https://doi.org/10.1073/pnas.1512832112.

(53) Peiris, P. M.; Toy, R.; Abramowski, A.; Vicente, P.; Tucci, S.; Bauer, L.; Mayer, A.; Tam, M.; Doolittle, E.; Pansky, J.; Tran, E.; Lin, D.; Schiemann, W. P.; Ghaghada, K. B.; Griswold, M. A.; Karathanasis, E. Treatment of Cancer Micrometastasis Using a Multicomponent Chain-like Nanoparticle. *J. Control. Release Off. J. Control. Release Soc.* **2014**, *173*, 51–58. https://doi.org/10.1016/j.jconrel.2013.10.031.

(54) Hobbs, S. K.; Monsky, W. L.; Yuan, F.; Roberts, W. G.; Griffith, L.; Torchilin, V. P.; Jain, R. K. Regulation of Transport Pathways in Tumor Vessels: Role of Tumor Type and Microenvironment. *Proc. Natl. Acad. Sci. U. S. A.* **1998**, *95* (8), 4607–4612. https://doi.org/10.1073/pnas.95.8.4607.

(55) Huebschman, M. L.; Lane, N. L.; Liu, H.; Sarode, V. R.; Devlin, J. L.; Frenkel, E. P. Molecular Heterogeneity in Adjacent Cells in Triple-Negative Breast Cancer. *Breast Cancer Dove Med. Press* **2015**, *7*, 231–237. https://doi.org/10.2147/BCTT.S87041.

(56) Norton, K.-A.; Popel, A. S.; Pandey, N. B. Heterogeneity of Chemokine Cell-Surface Receptor Expression in Triple-Negative Breast Cancer. *Am. J. Cancer Res.* **2015**, *5* (4), 1295–1307.

(57) Martínez-Revollar, G.; Garay, E.; Martin-Tapia, D.; Nava, P.; Huerta, M.; Lopez-Bayghen, E.; Meraz-Cruz, N.; Segovia, J.; González-Mariscal, L. Heterogeneity between Triple Negative Breast Cancer Cells Due to Differential Activation of Wnt and PI3K/AKT Pathways. *Exp. Cell Res.* **2015**, *339* (1), 67–80. https://doi.org/10.1016/j.yexcr.2015.10.006.

(58) van Zijl, F.; Krupitza, G.; Mikulits, W. Initial Steps of Metastasis: Cell Invasion and Endothelial Transmigration. *Mutat. Res.* **2011**, *728* (1–2), 23–34. https://doi.org/10.1016/j.mrrev.2011.05.002.

(59) Schroeder, A.; Heller, D. A.; Winslow, M. M.; Dahlman, J. E.; Pratt, G. W.; Langer, R.; Jacks, T.; Anderson, D. G. Treating Metastatic Cancer with Nanotechnology. *Nat. Rev. Cancer* **2011**, *12* (1), 39–50. https://doi.org/10.1038/nrc3180.

(60) Kassam, F.; Enright, K.; Dent, R.; Dranitsaris, G.; Myers, J.; Flynn, C.; Fralick, M.; Kumar, R.; Clemons, M. Survival Outcomes for Patients with Metastatic Triple-Negative Breast Cancer: Implications for Clinical Practice and Trial Design. *Clin. Breast Cancer* **2009**, *9* (1), 29–33. https://doi.org/10.3816/CBC.2009.n.005.

(61) Kinkel, K.; Lu, Y.; Both, M.; Warren, R. S.; Thoeni, R. F. Detection of Hepatic Metastases from Cancers of the Gastrointestinal Tract by Using Noninvasive Imaging Methods (US, CT, MR Imaging, PET): A Meta-Analysis. *Radiology* **2002**, *224* (3), 748–756. https://doi.org/10.1148/radiol.2243011362.

(62) Niekel, M. C.; Bipat, S.; Stoker, J. Diagnostic Imaging of Colorectal Liver Metastases with CT, MR Imaging, FDG PET, and/or FDG PET/CT: A Meta-Analysis of Prospective Studies Including Patients Who Have Not Previously Undergone Treatment. *Radiology* **2010**, *257* (3), 674–684. https://doi.org/10.1148/radiol.10100729.

(63) Pantel, K.; Alix-Panabières, C.; Riethdorf, S. Cancer Micrometastases. *Nat. Rev. Clin. Oncol.* **2009**, *6* (6), 339–351. https://doi.org/10.1038/nrclinonc.2009.44.

(64) Peiris, P. M.; Abramowski, A.; Mcginnity, J.; Doolittle, E.; Toy, R.; Gopalakrishnan, R.; Shah, S.; Bauer, L.; Ghaghada, K. B.; Hoimes, C.; Brady-Kalnay, S. M.; Basilion, J. P.; Griswold, M. A.; Karathanasis, E. Treatment of Invasive Brain Tumors Using a Chain-like Nanoparticle. *Cancer Res.* **2015**, *75* (7), 1356–1365. https://doi.org/10.1158/0008-5472.CAN-14-1540.

(65) Karathanasis, E.; Geigerman, C. M.; Parkos, C. A.; Chan, L.; Bellamkonda, R. V.; Jaye, D. L. Selective Targeting of Nanocarriers to Neutrophils and Monocytes. *Ann. Biomed. Eng.* **2009**, *37* (10), 1984–1992. https://doi.org/10.1007/s10439-009-9702-5.

(66) Karathanasis, E.; Park, J.; Agarwal, A.; Patel, V.; Zhao, F.; Annapragada, A. V.; Hu, X.; Bellamkonda, R. V. MRI Mediated, Non-Invasive Tracking of Intratumoral Distribution of Nanocarriers in Rat Glioma. *Nanotechnology* **2008**, *19* (31), 315101. https://doi.org/10.1088/0957-4484/19/31/315101.

(67) Liu, J.; Bu, J.; Bu, W.; Zhang, S.; Pan, L.; Fan, W.; Chen, F.; Zhou, L.; Peng, W.; Zhao, K.; Du, J.; Shi, J. Real-Time in Vivo Quantitative Monitoring of Drug Release by Dual-Mode Magnetic Resonance and Upconverted Luminescence Imaging.

Angew. Chem. Int. Ed Engl. **2014**, *53* (18), 4551–4555. https://doi.org/10.1002/anie.201400900.

(68) Croissant, J. G.; Fatieiev, Y.; Almalik, A.; Khashab, N. M. Mesoporous Silica and Organosilica Nanoparticles: Physical Chemistry, Biosafety, Delivery Strategies, and Biomedical Applications. *Adv. Healthc. Mater.* **2018**, *7* (4). https://doi.org/10.1002/adhm.201700831.

(69) McNeeley, K. M.; Karathanasis, E.; Annapragada, A. V.; Bellamkonda, R. V. Masking and Triggered Unmasking of Targeting Ligands on Nanocarriers to Improve Drug Delivery to Brain Tumors. *Biomaterials* **2009**, *30* (23–24), 3986–3995. https://doi.org/10.1016/j.biomaterials.2009.04.012.

(70) Calcagno, A. M.; Salcido, C. D.; Gillet, J.-P.; Wu, C.-P.; Fostel, J. M.; Mumau, M. D.; Gottesman, M. M.; Varticovski, L.; Ambudkar, S. V. Prolonged Drug Selection of Breast Cancer Cells and Enrichment of Cancer Stem Cell Characteristics. *J. Natl. Cancer Inst.* **2010**, *102* (21), 1637–1652. https://doi.org/10.1093/jnci/djq361.

(71) McCarty, O. J.; Mousa, S. A.; Bray, P. F.; Konstantopoulos, K. Immobilized Platelets Support Human Colon Carcinoma Cell Tethering, Rolling, and Firm Adhesion under Dynamic Flow Conditions. *Blood* **2000**, *96* (5), 1789–1797.

(72) Arnaout, M. A.; Mahalingam, B.; Xiong, J.-P. Integrin Structure, Allostery, and Bidirectional Signaling. *Annu. Rev. Cell Dev. Biol.* **2005**, *21*, 381–410. https://doi.org/10.1146/annurev.cellbio.21.090704.151217.

(73) Felding-Habermann, B.; O'Toole, T. E.; Smith, J. W.; Fransvea, E.; Ruggeri, Z. M.; Ginsberg, M. H.; Hughes, P. E.; Pampori, N.; Shattil, S. J.; Saven, A.; Mueller, B. M.

Integrin Activation Controls Metastasis in Human Breast Cancer. *Proc. Natl. Acad. Sci. U. S. A.* **2001**, *98* (4), 1853–1858. https://doi.org/10.1073/pnas.98.4.1853.

(74) Lorger, M.; Krueger, J. S.; O'Neal, M.; Staflin, K.; Felding-Habermann, B. Activation of Tumor Cell Integrin Alphavbeta3 Controls Angiogenesis and Metastatic Growth in the Brain. *Proc. Natl. Acad. Sci. U. S. A.* **2009**, *106* (26), 10666–10671. https://doi.org/10.1073/pnas.0903035106.

(75) Läubli, H.; Borsig, L. Selectins Promote Tumor Metastasis. *Semin. Cancer Biol.* **2010**, *20* (3), 169–177. https://doi.org/10.1016/j.semcancer.2010.04.005.

(76) Kim, Y. J.; Borsig, L.; Han, H. L.; Varki, N. M.; Varki, A. Distinct Selectin Ligands on Colon Carcinoma Mucins Can Mediate Pathological Interactions among Platelets, Leukocytes, and Endothelium. *Am. J. Pathol.* **1999**, *155* (2), 461–472. https://doi.org/10.1016/S0002-9440(10)65142-5.

(77) Ludwig, R. J.; Boehme, B.; Podda, M.; Henschler, R.; Jager, E.; Tandi, C.; Boehncke, W.-H.; Zollner, T. M.; Kaufmann, R.; Gille, J. Endothelial P-Selectin as a Target of Heparin Action in Experimental Melanoma Lung Metastasis. *Cancer Res.* **2004**, *64* (8), 2743–2750. https://doi.org/10.1158/0008-5472.can-03-1054.

(78) Nierodzik, M. L.; Karpatkin, S. Thrombin Induces Tumor Growth, Metastasis, and Angiogenesis: Evidence for a Thrombin-Regulated Dormant Tumor Phenotype. *Cancer Cell* **2006**, *10* (5), 355–362. https://doi.org/10.1016/j.ccr.2006.10.002.

(79) Borsig, L.; Wong, R.; Feramisco, J.; Nadeau, D. R.; Varki, N. M.; Varki, A. Heparin and Cancer Revisited: Mechanistic Connections Involving Platelets, P-Selectin, Carcinoma Mucins, and Tumor Metastasis. *Proc. Natl. Acad. Sci. U. S. A.* **2001**, *98* (6), 3352–3357. https://doi.org/10.1073/pnas.061615598.

(80) Mousa, S. A.; Petersen, L. J. Anti-Cancer Properties of Low-Molecular-Weight Heparin: Preclinical Evidence. *Thromb. Haemost.* **2009**, *102* (2), 258–267. https://doi.org/10.1160/TH08-12-0832.

(81) Pawlowski, V.; Révillion, F.; Hebbar, M.; Hornez, L.; Peyrat, J. P. Prognostic Value of the Type I Growth Factor Receptors in a Large Series of Human Primary Breast Cancers Quantified with a Real-Time Reverse Transcription-Polymerase Chain Reaction Assay. *Clin. Cancer Res. Off. J. Am. Assoc. Cancer Res.* **2000**, *6* (11), 4217–4225.

(82) Newby, J. C.; A'Hern, R. P.; Leek, R. D.; Smith, I. E.; Harris, A. L.; Dowsett, M. Immunohistochemical Assay for Epidermal Growth Factor Receptor on Paraffin-Embedded Sections: Validation against Ligand-Binding Assay and Clinical Relevance in Breast Cancer. *Br. J. Cancer* **1995**, *71* (6), 1237–1242. https://doi.org/10.1038/bjc.1995.239.

(83) Martinazzi, M.; Crivelli, F.; Zampatti, C.; Martinazzi, S. Epidermal Growth Factor Receptor Immunohistochemistry in Different Histological Types of Infiltrating Breast Carcinoma. *J. Clin. Pathol.* **1993**, *46* (11), 1009–1010. https://doi.org/10.1136/jcp.46.11.1009.

(84) Home - ClinicalTrials.gov https://clinicaltrials.gov/ (accessed Jul 20, 2020).

(85) Lichtner, R. B.; Kaufmann, A. M.; Kittmann, A.; Rohde-Schulz, B.; Walter, J.; Williams, L.; Ullrich, A.; Schirrmacher, V.; Khazaie, K. Ligand Mediated Activation of Ectopic EGF Receptor Promotes Matrix Protein Adhesion and Lung Colonization of Rat Mammary Adenocarcinoma Cells. *Oncogene* **1995**, *10* (9), 1823–1832.

(86) Mendelsohn, J.; Baselga, J. The EGF Receptor Family as Targets for Cancer Therapy. *Oncogene* **2000**, *19* (56), 6550–6565. https://doi.org/10.1038/sj.onc.1204082.

(87) Kondapaka, S. B.; Fridman, R.; Reddy, K. B. Epidermal Growth Factor and Amphiregulin Up-Regulate Matrix Metalloproteinase-9 (MMP-9) in Human Breast Cancer Cells. *Int. J. Cancer* **1997**, *70* (6), 722–726. https://doi.org/10.1002/(sici)1097-0215(19970317)70:6<722::aid-ijc15>3.0.co;2-b.

(88) Turner, T.; Chen, P.; Goodly, L. J.; Wells, A. EGF Receptor Signaling Enhances in Vivo Invasiveness of DU-145 Human Prostate Carcinoma Cells. *Clin. Exp. Metastasis* **1996**, *14* (4), 409–418. https://doi.org/10.1007/BF00123400.

(89) Steeg, P. S. Metastasis Suppressors Alter the Signal Transduction of Cancer Cells. *Nat. Rev. Cancer* **2003**, *3* (1), 55–63. https://doi.org/10.1038/nrc967.

(90) Karathanasis, E.; Chan, L.; Balusu, S. R.; D'Orsi, C. J.; Annapragada, A. V.; Sechopoulos, I.; Bellamkonda, R. V. Multifunctional Nanocarriers for Mammographic Quantification of Tumor Dosing and Prognosis of Breast Cancer Therapy. *Biomaterials* **2008**, *29* (36), 4815–4822. https://doi.org/10.1016/j.biomaterials.2008.08.036.

(91) Peiris, P. M.; Bauer, L.; Toy, R.; Tran, E.; Pansky, J.; Doolittle, E.; Schmidt, E.; Hayden, E.; Mayer, A.; Keri, R. A.; Griswold, M. A.; Karathanasis, E. Enhanced Delivery of Chemotherapy to Tumors Using a Multicomponent Nanochain with Radio-Frequency-Tunable Drug Release. *ACS Nano* **2012**, *6* (5), 4157–4168. https://doi.org/10.1021/nn300652p.

(92) Massoud, T. F.; Gambhir, S. S. Molecular Imaging in Living Subjects: Seeing Fundamental Biological Processes in a New Light. *Genes Dev.* **2003**, *17* (5), 545–580. https://doi.org/10.1101/gad.1047403.

(93) Kenanova, V.; Wu, A. M. Tailoring Antibodies for Radionuclide Delivery. *Expert Opin. Drug Deliv.* **2006**, *3* (1), 53–70. https://doi.org/10.1517/17425247.3.1.53.

(94) Wendt, M. K.; Taylor, M. A.; Schiemann, B. J.; Sossey-Alaoui, K.; Schiemann, W. P. Fibroblast Growth Factor Receptor Splice Variants Are Stable Markers of Oncogenic Transforming Growth Factor B1 Signaling in Metastatic Breast Cancers. *Breast Cancer Res. BCR* **2014**, *16* (2), R24. https://doi.org/10.1186/bcr3623.

(95) Wendt, M. K.; Taylor, M. A.; Schiemann, B. J.; Schiemann, W. P. Down-Regulation of Epithelial Cadherin Is Required to Initiate Metastatic Outgrowth of Breast Cancer. *Mol. Biol. Cell* **2011**, *22* (14), 2423–2435. https://doi.org/10.1091/mbc.E11-04-0306.

(96) Susnik, B.; Frkovic-Grazio, S.; Bracko, M. Occult Micrometastases in Axillary Lymph Nodes Predict Subsequent Distant Metastases in Stage I Breast Cancer: A Case-Control Study with 15-Year Follow-Up. *Ann. Surg. Oncol.* **2004**, *11* (6), 568–572. https://doi.org/10.1245/ASO.2004.10.021.

(97) Cote, R. J.; Peterson, H. F.; Chaiwun, B.; Gelber, R. D.; Goldhirsch, A.; Castiglione-Gertsch, M.; Gusterson, B.; Neville, A. M. Role of Immunohistochemical Detection of Lymph-Node Metastases in Management of Breast Cancer. International Breast Cancer Study Group. *Lancet Lond. Engl.* **1999**, *354* (9182), 896–900. https://doi.org/10.1016/s0140-6736(98)11104-2.

(98) Braun, S.; Kentenich, C.; Janni, W.; Hepp, F.; de Waal, J.; Willgeroth, F.; Sommer, H.; Pantel, K. Lack of Effect of Adjuvant Chemotherapy on the Elimination of Single

Dormant Tumor Cells in Bone Marrow of High-Risk Breast Cancer Patients. *J. Clin. Oncol. Off. J. Am. Soc. Clin. Oncol.* **2000**, *18* (1), 80–86. https://doi.org/10.1200/JCO.2000.18.1.80.

(99) Mansi, J. L.; Gogas, H.; Bliss, J. M.; Gazet, J. C.; Berger, U.; Coombes, R. C. Outcome of Primary-Breast-Cancer Patients with Micrometastases: A Long-Term Follow-up Study. *Lancet Lond. Engl.* **1999**, *354* (9174), 197–202. https://doi.org/10.1016/s0140-6736(98)10175-7.

(100) Gerber, B.; Krause, A.; Müller, H.; Richter, D.; Reimer, T.; Makovitzky, J.; Herrnring, C.; Jeschke, U.; Kundt, G.; Friese, K. Simultaneous Immunohistochemical Detection of Tumor Cells in Lymph Nodes and Bone Marrow Aspirates in Breast Cancer and Its Correlation with Other Prognostic Factors. *J. Clin. Oncol. Off. J. Am. Soc. Clin. Oncol.* **2001**, *19* (4), 960–971. https://doi.org/10.1200/JCO.2001.19.4.960.

(101) Perreard, L.; Fan, C.; Quackenbush, J. F.; Mullins, M.; Gauthier, N. P.; Nelson, E.; Mone, M.; Hansen, H.; Buys, S. S.; Rasmussen, K.; Orrico, A. R.; Dreher, D.; Walters, R.; Parker, J.; Hu, Z.; He, X.; Palazzo, J. P.; Olopade, O. I.; Szabo, A.; Perou, C. M.; Bernard, P. S. Classification and Risk Stratification of Invasive Breast Carcinomas Using a Real-Time Quantitative RT-PCR Assay. *Breast Cancer Res. BCR* **2006**, *8* (2), R23. https://doi.org/10.1186/bcr1399.

(102) Bertucci, F.; Finetti, P.; Cervera, N.; Charafe-Jauffret, E.; Buttarelli, M.; Jacquemier, J.; Chaffanet, M.; Maraninchi, D.; Viens, P.; Birnbaum, D. How Different Are Luminal A and Basal Breast Cancers? *Int. J. Cancer* **2009**, *124* (6), 1338–1348. https://doi.org/10.1002/ijc.24055.

(103) Anders, C. K.; Carey, L. A. Biology, Metastatic Patterns, and Treatment of Patients with Triple-Negative Breast Cancer. *Clin. Breast Cancer* **2009**, *9 Suppl 2*, S73-81. https://doi.org/10.3816/CBC.2009.s.008.

(104) O'Reilly, E. A.; Gubbins, L.; Sharma, S.; Tully, R.; Guang, M. H. Z.; Weiner-Gorzel, K.; McCaffrey, J.; Harrison, M.; Furlong, F.; Kell, M.; McCann, A. The Fate of Chemoresistance in Triple Negative Breast Cancer (TNBC). *BBA Clin.* **2015**, *3*, 257–275. https://doi.org/10.1016/j.bbacli.2015.03.003.

(105) Toy, R.; Bauer, L.; Hoimes, C.; Ghaghada, K. B.; Karathanasis, E. Targeted Nanotechnology for Cancer Imaging. *Adv. Drug Deliv. Rev.* **2014**, *76*, 79–97. https://doi.org/10.1016/j.addr.2014.08.002.

(106) Aslakson, C. J.; Miller, F. R. Selective Events in the Metastatic Process Defined by Analysis of the Sequential Dissemination of Subpopulations of a Mouse Mammary Tumor. *Cancer Res.* **1992**, *52* (6), 1399–1405.

(107) Morris, V. L.; Tuck, A. B.; Wilson, S. M.; Percy, D.; Chambers, A. F. Tumor Progression and Metastasis in Murine D2 Hyperplastic Alveolar Nodule Mammary Tumor Cell Lines. *Clin. Exp. Metastasis* **1993**, *11* (1), 103–112. https://doi.org/10.1007/BF00880071.

(108) Wendt, M. K.; Smith, J. A.; Schiemann, W. P. Transforming Growth Factor-β-Induced Epithelial-Mesenchymal Transition Facilitates Epidermal Growth Factor-Dependent Breast Cancer Progression. *Oncogene* **2010**, *29* (49), 6485–6498. https://doi.org/10.1038/onc.2010.377.

(109) Gooding, A. J.; Zhang, B.; Jahanbani, F. K.; Gilmore, H. L.; Chang, J. C.; Valadkhan, S.; Schiemann, W. P. The LncRNA BORG Drives Breast Cancer

Metastasis and Disease Recurrence. *Sci. Rep.* **2017**, *7* (1), 12698. https://doi.org/10.1038/s41598-017-12716-6.

(110) Ueno, N. T.; Zhang, D. Targeting EGFR in Triple Negative Breast Cancer. *J. Cancer* **2011**, *2*, 324–328. https://doi.org/10.7150/jca.2.324.

(111) Schreiber, R. D.; Old, L. J.; Smyth, M. J. Cancer Immunoediting: Integrating Immunity's Roles in Cancer Suppression and Promotion. *Science* **2011**, *331* (6024), 1565–1570. https://doi.org/10.1126/science.1203486.

(112) Borriello, L.; Seeger, R. C.; Asgharzadeh, S.; DeClerck, Y. A. More than the Genes, the Tumor Microenvironment in Neuroblastoma. *Cancer Lett.* **2016**, *380* (1), 304–314. https://doi.org/10.1016/j.canlet.2015.11.017.

(113) Müller, L.; Aigner, P.; Stoiber, D. Type I Interferons and Natural Killer Cell Regulation in Cancer. *Front. Immunol.* **2017**, *8*, 304. https://doi.org/10.3389/fimmu.2017.00304.

(114) Swartz, M. A.; Hirosue, S.; Hubbell, J. A. Engineering Approaches to Immunotherapy. *Sci. Transl. Med.* **2012**, *4* (148), 148rv9. https://doi.org/10.1126/scitranslmed.3003763.

(115) Cheng, N.; Watkins-Schulz, R.; Junkins, R. D.; David, C. N.; Johnson, B. M.; Montgomery, S. A.; Peine, K. J.; Darr, D. B.; Yuan, H.; McKinnon, K. P.; Liu, Q.; Miao, L.; Huang, L.; Bachelder, E. M.; Ainslie, K. M.; Ting, J. P.-Y. A Nanoparticle-Incorporated STING Activator Enhances Antitumor Immunity in PD-L1-Insensitive Models of Triple-Negative Breast Cancer. *JCI Insight* **2018**, *3* (22). https://doi.org/10.1172/jci.insight.120638.

(116) Corrales, L.; Glickman, L. H.; McWhirter, S. M.; Kanne, D. B.; Sivick, K. E.; Katibah, G. E.; Woo, S.-R.; Lemmens, E.; Banda, T.; Leong, J. J.; Metchette, K.; Dubensky, T. W.; Gajewski, T. F. Direct Activation of STING in the Tumor Microenvironment Leads to Potent and Systemic Tumor Regression and Immunity. *Cell Rep.* **2015**, *11* (7), 1018–1030. https://doi.org/10.1016/j.celrep.2015.04.031.

(117) Corrales, L.; Gajewski, T. F. Endogenous and Pharmacologic Targeting of the STING Pathway in Cancer Immunotherapy. *Cytokine* **2016**, *77*, 245–247. https://doi.org/10.1016/j.cyto.2015.08.258.

(118) Corrales, L.; Gajewski, T. F. Molecular Pathways: Targeting the Stimulator of Interferon Genes (STING) in the Immunotherapy of Cancer. *Clin. Cancer Res. Off. J. Am. Assoc. Cancer Res.* **2015**, *21* (21), 4774–4779. https://doi.org/10.1158/1078-0432.CCR-15-1362.

(119) Turan, O.; Bielecki, P.; Tong, K.; Covarrubias, G.; Moon, T.; Rahmy, A.; Cooley, S.; Park, Y.; Peiris, P. M.; Ghaghada, K. B.; Karathanasis, E. Effect of Dose and Selection of Two Different Ligands on the Deposition and Antitumor Efficacy of Targeted Nanoparticles in Brain Tumors. *Mol. Pharm.* **2019**, *16* (10), 4352–4360. https://doi.org/10.1021/acs.molpharmaceut.9b00693.

(120) Dupuy, A. G.; Caron, E. Integrin-Dependent Phagocytosis: Spreading from Microadhesion to New Concepts. *J. Cell Sci.* **2008**, *121* (11), 1773–1783. https://doi.org/10.1242/jcs.018036.

(121) Hanayama, R.; Tanaka, M.; Miwa, K.; Shinohara, A.; Iwamatsu, A.; Nagata, S. Identification of a Factor That Links Apoptotic Cells to Phagocytes. *Nature* **2002**, *417* (6885), 182–187. https://doi.org/10.1038/417182a.

(122) Savill, J.; Dransfield, I.; Hogg, N.; Haslett, C. Vitronectin Receptor-Mediated Phagocytosis of Cells Undergoing Apoptosis. *Nature* **1990**, *343* (6254), 170–173. https://doi.org/10.1038/343170a0.

(123) Tao, K.; Fang, M.; Alroy, J.; Sahagian, G. G. Imagable 4T1 Model for the Study of Late Stage Breast Cancer. *BMC Cancer* **2008**, *8*, 228. https://doi.org/10.1186/1471-2407-8-228.

(124) Morrison, C. D.; Parvani, J. G.; Schiemann, W. P. The Relevance of the TGF-β Paradox to EMT-MET Programs. *Cancer Lett.* **2013**, *341* (1), 30–40. https://doi.org/10.1016/j.canlet.2013.02.048.

(125) Gooding, A. J.; Zhang, B.; Gunawardane, L.; Beard, A.; Valadkhan, S.; Schiemann, W. P. The LncRNA BORG Facilitates the Survival and Chemoresistance of Triple-Negative Breast Cancers. *Oncogene* **2019**, *38* (12), 2020–2041. https://doi.org/10.1038/s41388-018-0586-4.

(126) Wendt, M. K.; Tian, M.; Schiemann, W. P. Deconstructing the Mechanisms and Consequences of TGF-β-Induced EMT during Cancer Progression. *Cell Tissue Res.* **2012**, *347* (1), 85–101. https://doi.org/10.1007/s00441-011-1199-1.

(127) Gooding, A. J.; Schiemann, W. P. Harnessing Protein Kinase A Activation to Induce Mesenchymal-Epithelial Programs to Eliminate Chemoresistant, Tumor-Initiating Breast Cancer Cells. *Transl. Cancer Res.* **2016**, *5* (Suppl 2), S226–S232. https://doi.org/10.21037/tcr.2016.08.09.

(128) Robinson, N. J.; Schiemann, W. P. Means to the Ends: The Role of Telomeres and Telomere Processing Machinery in Metastasis. *Biochim. Biophys. Acta* **2016**, *1866* (2), 320–329. https://doi.org/10.1016/j.bbcan.2016.10.005.

(129) La Belle, A. A.; Schiemann, W. P. Oncostatin M Activation of Stat3:Smad3 Complexes Drives Senescence. *Cell Cycle Georget. Tex* **2017**, *16* (6), 497–498. https://doi.org/10.1080/15384101.2017.1287862.

(130) Taylor, M. A.; Lee, Y.-H.; Schiemann, W. P. Role of TGF-β and the Tumor Microenvironment during Mammary Tumorigenesis. *Gene Expr.* **2011**, *15* (3), 117–132. https://doi.org/10.3727/105221611x13176664479322.

(131) Taylor, M. A.; Sossey-Alaoui, K.; Thompson, C. L.; Danielpour, D.; Schiemann, W. P. TGF-β Upregulates MiR-181a Expression to Promote Breast Cancer Metastasis. *J. Clin. Invest.* **2013**, *123* (1), 150–163. https://doi.org/10.1172/JCI64946.

(132) Wendt, M. K.; Schiemann, W. P. Therapeutic Targeting of the Focal Adhesion Complex Prevents Oncogenic TGF-Beta Signaling and Metastasis. *Breast Cancer Res. BCR* **2009**, *11* (5), R68. https://doi.org/10.1186/bcr2360.

(133) Roland, C. L.; Harken, A. H.; Sarr, M. G.; Barnett, C. C. ICAM-1 Expression Determines Malignant Potential of Cancer. *Surgery* **2007**, *141* (6), 705–707. https://doi.org/10.1016/j.surg.2007.01.016.

(134) Yang, J.; Zhang, L.; Yu, C.; Yang, X.-F.; Wang, H. Monocyte and Macrophage Differentiation: Circulation Inflammatory Monocyte as Biomarker for Inflammatory Diseases. *Biomark. Res.* **2014**, *2* (1), 1. https://doi.org/10.1186/2050-7771-2-1.

(135) Klimp, A. H.; de Vries, E. G. E.; Scherphof, G. L.; Daemen, T. A Potential Role of Macrophage Activation in the Treatment of Cancer. *Crit. Rev. Oncol. Hematol.* **2002**, *44* (2), 143–161. https://doi.org/10.1016/s1040-8428(01)00203-7.

(136) Martinez-Pomares, L. The Mannose Receptor. *J. Leukoc. Biol.* **2012**, *92* (6), 1177–1186. https://doi.org/10.1189/jlb.0512231.

(137) Andersen, M. N.; Andersen, N. F.; Rødgaard-Hansen, S.; Hokland, M.; Abildgaard, N.; Møller, H. J. The Novel Biomarker of Alternative Macrophage Activation, Soluble Mannose Receptor (SMR/SCD206): Implications in Multiple Myeloma. *Leuk. Res.* **2015**, *39* (9), 971–975. https://doi.org/10.1016/j.leukres.2015.06.003.

(138) Puri, A.; Loomis, K.; Smith, B.; Lee, J.-H.; Yavlovich, A.; Heldman, E.; Blumenthal, R. Lipid-Based Nanoparticles as Pharmaceutical Drug Carriers: From Concepts to Clinic. *Crit. Rev. Ther. Drug Carr. Syst.* **2009**, *26* (6). https://doi.org/10.1615/CritRevTherDrugCarrierSyst.v26.i6.10.

(139) Bobo, D.; Robinson, K. J.; Islam, J.; Thurecht, K. J.; Corrie, S. R. Nanoparticle-Based Medicines: A Review of FDA-Approved Materials and Clinical Trials to Date. *Pharm. Res.* **2016**, *33* (10), 2373–2387. https://doi.org/10.1007/s11095-016-1958-5.

(140) Beltrán-Gracia, E.; López-Camacho, A.; Higuera-Ciapara, I.; Velázquez-Fernández, J. B.; Vallejo-Cardona, A. A. Nanomedicine Review: Clinical Developments in Liposomal Applications. *Cancer Nanotechnol.* **2019**, *10* (1), 11. https://doi.org/10.1186/s12645-019-0055-y.

(141) Anselmo, A. C.; Mitragotri, S. Nanoparticles in the Clinic: An Update. *Bioeng. Transl. Med.* **2019**, *4* (3). https://doi.org/10.1002/btm2.10143.

(142) Study of Intratumorally Administered Stimulator of Interferon Genes (STING) Agonist E7766 in Participants With Advanced Solid Tumors or Lymphomas - INSTAL-101 - Full Text View - ClinicalTrials.gov https://clinicaltrials.gov/ct2/show/NCT04144140 (accessed Jul 21, 2020).

(143) Study of MK-1454 Alone or in Combination With Pembrolizumab (MK-3475) in Participants With Advanced / Metastatic Solid Tumors or Lymphomas (MK-1454-

001) https://www.cancer.gov/about-cancer/treatment/clinical-trials/search/v?id=NCI-2017-00280 (accessed Jul 21, 2020).

(144) Efficacy and Safety Trial of ADU-S100 and Pembrolizumab in Head and Neck Cancer https://www.cancer.gov/about-cancer/treatment/clinical-trials/search/v?id=NCI-2019-04759 (accessed Jul 21, 2020).

(145) Coomberl, B. L.; Stewart, P. A.; Hayakawa, K.; Farrell, C. L.; Del Maestros, R. F. Quantitative Morphology of Human Glioblastoma Multiforme Microvessels: Structural Basis of Blood-Brain Barrier Defect. *J. Neurooncol.* **1987**, *5* (4), 299–307. https://doi.org/10.1007/BF00148386.

(146) Jena, L.; McErlean, E.; McCarthy, H. Delivery across the Blood-Brain Barrier: Nanomedicine for Glioblastoma Multiforme. *Drug Deliv. Transl. Res.* **2020**, *10* (2), 304–318. https://doi.org/10.1007/s13346-019-00679-2.

(147) Rascher, G.; Fischmann, A.; Kröger, S.; Duffner, F.; Grote, E.-H.; Wolburg, H. Extracellular Matrix and the Blood-Brain Barrier in Glioblastoma Multiforme: Spatial Segregation of Tenascin and Agrin. *Acta Neuropathol. (Berl.)* **2002**, *104* (1), 85–91. https://doi.org/10.1007/s00401-002-0524-x.

(148) Covarrubias, G.; Johansen, M. L.; Vincent, J.; Erokwu, B. O.; Craig, S. E. L.; Rahmy, A.; Cha, A.; Lorkowski, M.; MacAskill, C.; Scott, B.; Gargesha, M.; Roy, D.; Flask, C. A.; Karathanasis, E.; Brady-Kalnay, S. M. PTPmu-Targeted Nanoparticles Label Invasive Pediatric and Adult Glioblastoma. *Nanomedicine Nanotechnol. Biol. Med.* **2020**, *28*, 102216. https://doi.org/10.1016/j.nano.2020.102216.